Optimization of Fuel Cell Hybrid Vehicles

Von der Fakultät für Ingenieurwissenschaften, Abteilung Maschinenbau und Verfahrenstechnik
der
Universität Duisburg-Essen
zur Erlangung des akademischen Grades

eines

Doktors der Ingenieurwissenschaften

Dr.-Ing.

genehmigte Dissertation

von

Farouk Odeim
aus
Zahr Almagher / Syrien

Gutachter: Univ.-Prof. Dr. rer. nat. Angelika Heinzel
Univ.-Prof. Dr.-Ing. Dirk Abel
Tag der mündlichen Prüfung: 07.05.2018

Abstract

The limited fossil fuel resources and the environmental concerns associated with burning those fossil fuels lie behind the increasing interest in hydrogen as a clean and sustainable alternative to fossil fuels, and in fuel cells as a clean converter of hydrogen into electrical energy especially in the transportation sector. Fuel cell hybrid vehicles (FCHVs) are characterized by the use of a fuel cell system (FCS) as the main power source and a battery, a supercapacitor or both as an energy storage system (ESS). Hybridizing the FCS with an ESS significantly improves the hydrogen economy, helps downsize the FCS, and resolves the issues related the long start-up time and slow dynamics of the FCS. The existence of multiple power sources in the powertrain gives rise to two important questions: How to coordinate the power contribution of the sources (i.e., power management strategy (PMS)), and how to size these sources in order to exploit the advantages of hybridization.

The goal of this thesis is to develop a comprehensive framework for the optimization of PMS and size of FCHV powertrains. Depending on the type of ESS, three topologies are considered: fuel cell/ battery, fuel cell/ supercapacitor, and fuel cell/ battery/ supercapacitor. The PMS optimization is investigated on two levels; i.e., the vehicle level by simulation and the developed optimization algorithms are then validated on a small-scale test bench.

When the driving cycle is known a priori, the off-line optimal PMS that globally minimizes the hydrogen consumption is calculated by two algorithms, namely, Dynamic Programming (DP) and Pontryagin's Minimum Principle (PMP), and the two algorithms are compared. It has been found that PMP can be a superior approach for off-line optimization since it requires negligible computation resources without sacrificing the global optimality. The off-line optimal strategy is not real-time capable; hence, real-time strategies are designed and optimized while using the off-line optimal PMS as a benchmark. Special emphasize is put on the inclusion of multiple driving cycles, of different nature, in the optimization of the real-time PMS to increase its robustness.

The sizing of the power sources of fuel cell/ battery and fuel cell/ supercapacitor hybrids considers hydrogen consumption and powertrain cost as two objectives and takes into account the drivability constraints such as top speed, gradeablity and acceleration time. The interesting designs (i.e., FCS size and ESS size), which represent the most efficient trade-off between the objectives, are then extracted and analyzed. The effect of battery aging on the optimal powertrain size is investigated by an Ampere-hour throughput model. It has been found that the battery aging leads to less efficient powertrain designs and the supercapacitor can become a more efficient option in comparison to batteries of poor lifetime.

Zusammenfassung

Die begrenzten fossilen Ressourcen und die Umweltsorgen, die mit der Verbrennung dieser fossilen Brennstoffe verbunden sind, stecken hinter dem steigenden Interesse am Wasserstoff als sauberer und nachhaltiger Alternative, und an Brennstoffzellen als sauberen Wandlern des Wasserstoffs in elektrische Energie, vor allem im Verkehrssektor. Ein Brennstoffzellen-Hybridfahrzeug (FCHV) verwendet ein Brennstoffzellensystem (FCS) als eine Hauptenergiequelle und eine Batterie, einen Superkondensator oder beide als Energiespeichersystem (ESS). Hybridisierung des FCS mit einem ESS verringert erheblich den Wasserstoffverbrauch, hilft das FCS zu verkleinern, und behebt das Problem der langen Anlaufzeit und der langsamen Dynamik des FCS. Die Existenz von mehreren Stromquellen im Antriebsstrang wirft zwei wichtige Fragen auf: Wie ist die Leistungsanforderung des Fahrzeugs zwischen den Quellen zu verteilen (d.h. Power-Management-Strategie (PMS)) und wie sind diese Quellen zu dimensionieren, um die Hybridisierung auszunutzen.

Das Ziel dieser Arbeit ist es, einen umfassenden Rahmen für die Optimierung der PMS und Dimensionierung der Brennstoffzellen-basierten hybriden Antriebsstränge zu entwickeln. Abhängig von der Art des ESS werden drei Topologien berücksichtigt: Brennstoffzelle/ Batterie, Brennstoffzelle/ Superkondensator und Brennstoffzelle/ Batterie/ Superkondensator. Die PMS-Optimierung wird auf zwei Ebenen untersucht, und zwar die Fahrzeugebene durch Simulation und die Prüfstandsebene, worauf die entwickelten Optimierungsalgorithmen experimentell validiert werden.

Wenn der Lastzyklus im Voraus bekannt ist, kann die offline optimale PMS, die den Wasserstoffverbrauch global minimiert, berechnet werden. Dazu werden die zwei Algorithmen, Dynamische Programmierung (DP) und Pontryagins Minimumprinzip (PMP), verglichen. Es wurde herausgefunden, dass das PMP ein überlegener Ansatz für die offline-Optimierung sein kann, da es viel weniger Rechenressourcen braucht, ohne die globale Optimalität zu opfern. Die offline optimale Strategie ist nicht echtzeitfähig, und deshalb werden Echtzeit-Strategien entworfen und optimiert, indem die offline optimale PMS als Maßstab verwendet wird. Beim Designen der echtzeitfähigen Strategien werden mehrere Fahrzyklen unterschiedlicher Natur beachtet, um die Robustheit der Strategien zu erhöhen.

Die Dimensionierung der Stromquellen der Brennstoffzelle/ Batterie und Brennstoffzelle/ Superkondensator Hybriden betrachtet den Wasserstoffverbrauch und die Kosten des Antriebsstrangs als zwei Ziele. Es wird dabei die Fahrbarkeit, d.h. Höchstgeschwindigkeit, Steigfähigkeit und Beschleunigungszeit, berücksichtigt. Die interessanten Konfigurationen (FCS-Größe und ESS-Größe), die den effizientesten Kompromiss zwischen den Zielen darstellen, werden dann herausgefunden und analysiert. Die Wirkung der Batteriealterung auf die optimale Antriebsstrang-Größe wird durch ein Ampere-Stunden-Durchsatzmodell untersucht. Es wurde herausgefunden, dass die Batterie-Alterung weniger effiziente Antriebsstrang-Konfigurationen ergibt, und dass der Superkondensator eine effizientere Alternative zur Batterie sein kann, wenn er mit Batterien von schlechter Lebensdauer verglichen wird.

Acknowledgments

In the first place, I would like to thank Prof. Dr. Angelika Heinzel for giving me the opportunity to write this work under her supervision at the Chair of Energy Technology. Her guidance and support over the years have pushed me to work harder and contribute more to the research field than I would otherwise have been capable of doing.

I would also like to express may gratitude to Prof. Dr. Dirk Abel for taking over the role of co-referee of this thesis, and to all the members of the examination committee for making the oral exam so comfortable.

My special thanks are extended to Dr. Jürgen Roes who has been always there with his continuous support in the research-related as well as the personal problems. His insightful reviews of my research progress have helped me get back on track after tough times.

Additionally, I am thankful to all the workers and PhD students of the Chair of Energy Technology. Working with them has been a very enriching experience.

Last but not least, I am infinitely grateful to my family. Their continuous support and love have sustained me throughout my life.

Contents

Nomenclature

Abbreviations

A_f	Vehicle frontal area
C	Capacitance
C_d	Aerodynamic drag coefficient
C_r	Rolling friction coefficient
E	Energy
F	Force
G	Gear ratio
g	Acceleration of gravity
I	Current
J	Cost function
m	Vehicle mass
P	Power
Q	Capacity
R	Resistance
r	Wheel radius
T	Torque
t	Time
T_s	Sample time
V	Voltage
v	Speed
x	State
f	Function

Subscripts

acc	Acceleration
aux	Auxiliaries
a	Aerodynamic drag
b	Battery
chg	Charge
dem	Demand
dis	Dischage
$fcdc$	Fuel cell DC/DC converter
fc	Fuel cell system
g	Gravity
m	Motor

opt	Optimal
r	Rolling friction
scdc	Supercapacitor DC/DC converter
sc	Supercapacitor
trans	Transmission
w	Wheel

Greek Letters

η	Efficiency
λ	Co-state
ω	Rotational speed
ρ	Air density
θ	Road angle

Acronyms

BLCS	Battery longevity-conscious strategy
BLNCS	Battery longevity-nonconscious strategy
DOE	US Department of Energy
DP	Dynamic Programming
EOL	End-of-life
ESS	Energy storage system
EV	Electric vehicle
FCHV	Fuel cell hybrid vehicle
FCS	Fuel cell system
GA	Genetic algorithm
HC	Hydrogen consumption
HEV	Hybrid electric vehicle
HWFET	Highway Fuel Economy Test
ICE	Internal combustion engine
J. 10-15	Japanese 10-15 Mode driving cycle
NEDC	New European Driving Cycle
NSGA	Non-dominated sorting genetic algorithm
OCV	Open circuit voltage
PEMFC	Polymer electrolyte membrane fuel cell
PMP	Pontryagin's Minimum Principle
PMS	Power management strategy
PSO	Particle swarm optimization
SOC	State-of-charge
SOE	State-of-energy
UDDS	Urban Dynamometer Driving Schedule

Chapter 1

Introduction

1.1 Why Hybrid Vehicles?

Vehicles powered by conventional internal combustion engines (ICEs) have been in existence for over a century. The demand for vehicles for personal transportation has increased dramatically in the past decade[1] [1] and it will continue to increase bolstered by the increase of world population and the fast economic growth of the large emerging markets, such as China and India. This trend has contributed to the significant increase in oil consumption since the transportation sector accounts for the major oil consumption as illustrated in Figure 1.1(a). In addition to oil dependency, there are environmental concerns (i.e., pollution, global warming ...) associated with the increasing use of passenger vehicles. As illustrated in Figure 1.1(b), transportation sector accounted for about a third of the total carbon dioxide emissions worldwide in 2010.

To face the above two serious issues, government agencies and organizations have developed more stringent standards for the fuel consumption and emissions. For example, the European Union has set a CO_2 average emissions target for new passenger cars of 130 g/km by 2015 and 95 g/km by 2021 [2], corresponding to a decrease of 11% and 35%, respectively, in comparison to 2009 emissions level of 145.7 g/km [3].

Electric vehicles (EVs) powered by batteries were one of the solutions proposed to tackle the energy crisis and global warming. However, the high initial cost, short driving range, and long charging time are major obstacles facing the wide market penetration of EVs.

Commercially introduced in the late 90s, the hybrid electric vehicles (HEVs) were developed to overcome the disadvantages of both ICE vehicles and EVs. The HEV uses an ICE and an energy storage system (ESS), mainly battery, as an energy buffer to power the vehicle. The addition of battery helps reduce the fuel consumption and emissions by:

- Downsizing the engine and still fulfilling the maximum power requirements of the vehicle;

[1] According to [1], 41.2 and 67.5 million passenger cars were produced in 2000 and 2014, respectively.

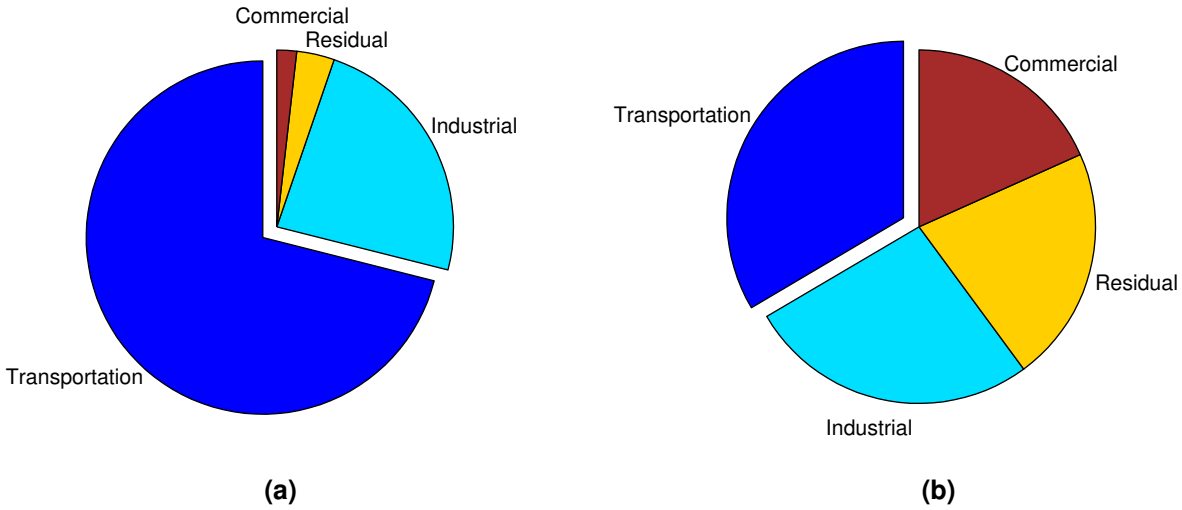

Figure 1.1: (a) Petroleum consumption and (b) carbon dioxide emissions by sector in 2010. Data from [4].

- Recovering some energy during deceleration instead of dissipating it in friction braking;
- Optimizing the energy distribution between the ICE and the battery;
- Eliminating engine idling by turning off the engine when no power is required (i.e., stop/start system).

As shown in Figure 1.2, four possible power paths can exist between the ICE, the energy buffer and the load (i.e., vehicle wheels). The power path (1) is from the ICE to the load, the path (2) is from the ICE to the energy buffer, the path (3) is from the energy buffer to the load, and the path (4) is from the load to the energy buffer (i.e., regenerative braking). Depending on the actual power flow in the powertrain, seven distinctive modes of operation can be recognized:

- The ICE drives the load alone (power flows in path (1));
- The ICE charges the energy buffer (power flows in path (2));
- The ICE and the energy buffer drive the load together (power flows in paths (1) and (3));
- The ICE drives the load and charges the energy buffer (power flows in paths (1) and (2));
- The energy buffer drives the load alone (power flows in path (3));
- The load charges the battery by regenerative braking (power flows in path (4));
- Both the load (by regenerative braking) and the ICE charge the energy buffer (power flows in paths (2) and (4)).

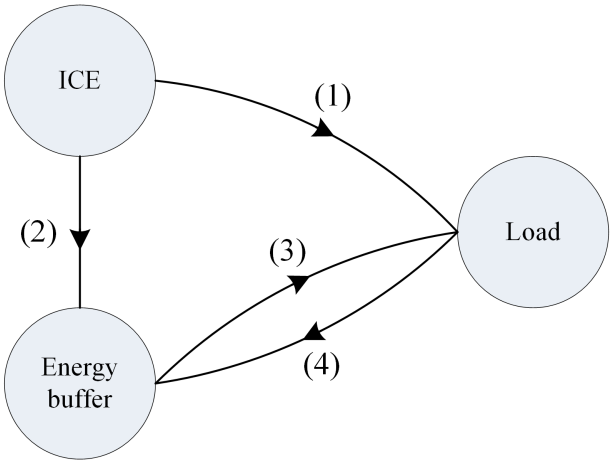

Figure 1.2: Possible power flow directions in hybrid powertrains.

According to the battery size, HEVs can be classified into mild, micro and full hybrids. The main characteristics of these three types are listed in Table 1.1. In micro hybrids, the battery is small and its main function is to start/stop the ICE to avoid idling; hence, the fuel saving is limited to few percent in city driving where there are frequent starts and stops. The battery size and power are larger in mild hybrids and it can assist the ICE in driving the vehicle giving rise to higher fuel saving up to about 20% in city driving. The battery size is further increased in full hybrids, so that the pure electric driving becomes possible and the fuel saving becomes more significant. Between full hybrids and EVs, there is also plug-in hybrids that feature larger batteries than full hybrids so that the battery drives the vehicle alone for an extended time (in the charge depleting mode), and the battery can be charged from the grid like those of EVs.

Table 1.1: Selected characteristics of HEV categories: mild, micro and full hybrids. Data from various sources [5, 6, 7] and net.

	Micro hybrid	Mild hybrid	Full hybrid
Functionality			
Stop/start	✓	✓	✓
Regenerative braking	✓	✓	✓
Engine assist		✓	✓
Pure electric driving			✓
Specifications			
Battery voltage	12-48 V	48-150 V	200-650 V
Battery power	<10 kW	10-20 kW	>20 kW
Max. fuel saving	<10%	10-20%	>20%
Example vehicles	BMW 1 and 3 series; Ford Focus and Transit; Mercedes-Benz A-class	Honda Civic and Insight Hybrid; Mercedes-Benz S400 BlueHybrid	Toyota Prius Hybrid; Ford Fusion Hybrid; Kia Optima Hybrid

1.2 Fuel Cell Hybrid Vehicles

Fuel cell hybrid vehicles (FCHVs) are hybrid vehicles that use fuel cells instead of ICE. Fuel cells are electrochemical energy converters that convert the chemical energy of hydrogen into electricity while producing water as a by-product; hence, they do not produce pollutants (i.e., zero emission). Additionally, fuel cells exhibit higher efficiency than ICE since they do not involve thermal energy as an intermediate step in the electrochemical energy conversion; hence, unlike ICE, fuel cells are not limited by Carnot efficiency. There are many types of fuel cells [8]; among them the so-called polymer electrolyte membrane fuel cells (PEMFCs) are most suited for automotive applications for their high specific power and power density and their relatively fast start-up time since they operate at relatively low temperature (around 80 °C).

Nearly all automakers have produced concept fuel cell-based vehicles. They are, as examples, Mercedes-Benz F-Cell B-class by Daimler, Audi A7 h-tron quattro by Audi, Honda FCV Concept by Honda, Toyota FCV by Toyota, VW Golf SportWagen Hymotion by Volkswagen, Hyundai ix35 FCEV by Hyundai.

Even though fuel cell vehicles have not yet entered the large commercialization phase, they have a great potential to be the final step in the transition of the transportation sector to the environmentally friendly vehicles [9]. However, coming to this stage requires the fuel cell technology to overcome many technical challenges, such as reducing the system cost[2], improving the durability[3] and reducing the system weight and volume[4], in addition to the challenges associated with hydrogen production, delivery and storage [10].

In addition to the aforementioned advantages of hybridization, the ESS in FCHVs helps smooth the fuel cells power demand prolonging its lifetime. High load dynamics is considered as the main aging accelerator of PEMFCs [11]. Fast load changing leads to many degradation effects like flooding of the porous media of the electrodes, dehydration of the membrane, and the loss in the catalyst layer due to gas starvation [12].

A PEMFC consists of a membrane sandwiched between two porous electrodes as depicted in Figure 1.3. The membrane has a special property that allows positive ions (protons) to pass through while blocking electrons. Hydrogen gas passes over one electrode (the anode), and with the help of a catalyst, splits into electrons and protons. The protons flow to the other electrode (the cathode) through the electrolyte while the electrons flow through an external circuit, thus creating electricity. The protons and electrons combine with oxygen flow through the cathode and produce water. The voltage produced from one cell is between 0 to 1 volt depending on the fuel cell operating conditions and the load size. To get higher voltages, multiple cells are connected in series to form a fuel cell stack.

[2]The US Department of Energy (DOE) reported a cost for automotive fuel cell systems of US$49/kW in 2011 and set a target of US$30/kW for 2020. The cost figures are projected to high-volume production of 500000 units per year [10].

[3]According to [10], the 2011 status for fuel cell system durability was 2500 hours over automotive driving cycle, and the target is to reach 5000 hours by 2020 to be comparable with the current automotive engines. The durability refers here to the time by which the system voltage degrades by 10%.

[4]According to [10], the 2011 status for automotive fuel cell systems is 400 W/kg for the specific power and 400 W/L for the power density, whereas the 2020 targets are 650 W/kg and 850 W/L, respectively.

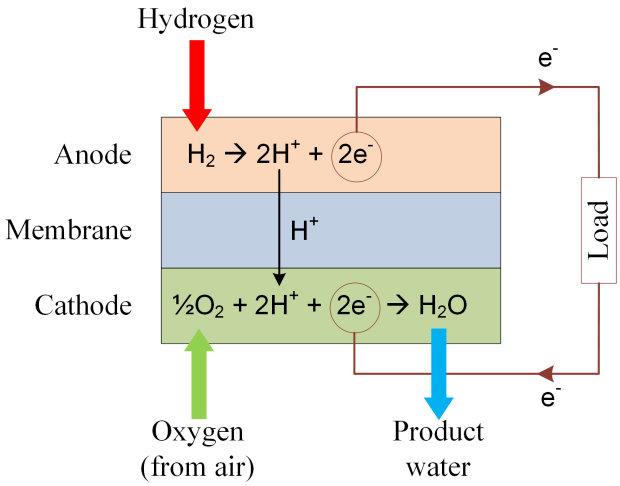

Figure 1.3: PEM fuel cell operating principle.

In order to generate power, the fuel cell stack needs to be integrated with other components to form a fuel cell system (FCS). In addition to the stack, the FCS includes typically three main subsystems: air supply subsystem, water management subsystem and thermal management subsystem. The hydrogen is typically stored in pressurized tanks; otherwise, if alternative hydrogen-rich fuels, such as natural gas or methanol, are used, then a reformer is needed to convert the fuel into hydrogen before feeding it into the fuel cell stack. The air supply subsystem, basically a compressor, sucks air from the ambient and feeds it with a controlled flow rate into the cathode compartment of the stack. The water management subsystem humidifies the air entering the stack by means of a humidifier. Water management is crucial for proper operation of the system; i.e., sufficient humidification is required to keep the water content in the membrane high for high conductivity, but too high humidity may cause flooding and blocking of the porous media in the electrodes. The thermal management subsystem has the role of maintaining the stack temperature in the proper range by removing excessive heat generated by the electrochemical reaction. This task is typically performed by means of de-ionized water circulating in channels through the stack.

1.3 Energy Storage Systems

Most of HEVs and FCHVs produced by automakers use a battery as an ESS to assist the main power source in fulfilling the power demand. Lithium-ion (Li-ion) and Nickel Metal Hydride (NiMH) are the dominant battery technologies. Li-ion batteries excel NiMH batteries in terms of specific power and specific energy as shown in Figure 1.4 and, additionally, in terms of efficiency. However, Li-ion batteries are still more expensive due to the relatively lower production volume, so that increasing the production volume is expected to make Li-ion batteries more economical in the future [13].

A Li-ion cell is composed of two electrodes (anode and cathode) and an electrolyte that allows Li ions to move through between the electrodes. Whereas graphite is the dominant anode material for Li-ion batteries, there are many possible cathode materials such

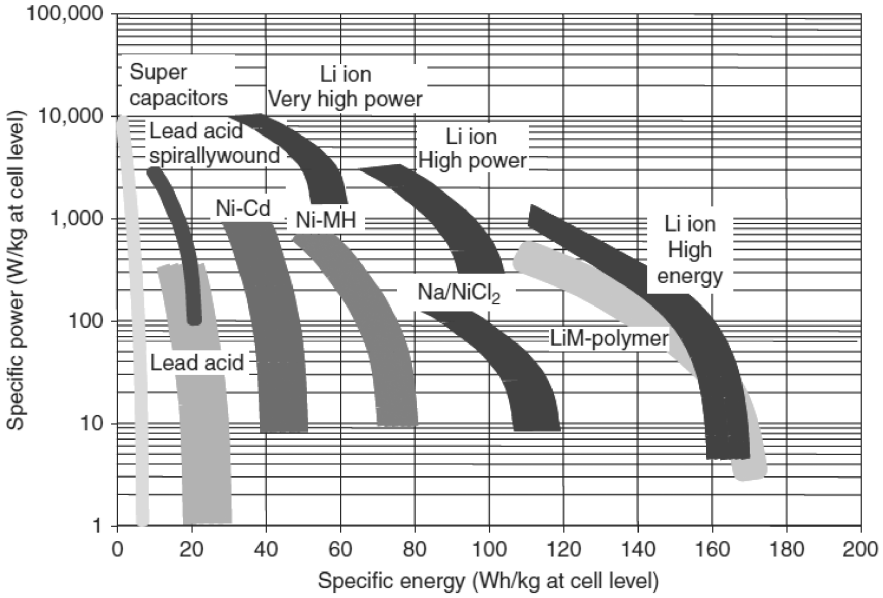

Figure 1.4: Comparison between different battery systems in terms of specific power and specific energy [13].

as Lithium Cobalt Oxide LiCoO2 (LCO), Lithium Manganese Oxide LiMn2O4 (LMO), Lithium Nickel Manganese Cobalt Oxide LiNiMnCoO2 (NMC), Lithium Nickel Cobalt Aluminum Oxide LiNiCoAlO2 (NCA) and Lithium Iron Phosphate LiFePO4 (LFP). Hitachi and Samsung SDI (with their NMC batteries), Johnson Controls (with its NCA batteries), and A123 System (with its LFP batteries) are among the top batteries suppliers for HEVs.

The reactions occurring at the electrodes of a Li-ion cell are given below for graphite (C_6) anode and LCO cathode, as an example. Both electrodes allow Li ions to move in (i.e., intercalation process) and out (i.e., deintercalaction process) of their interiors. During discharge, Li positive ions move from the anode leaving behind electrons that flow through an external circuit (i.e., load). Li ions flow through the ionic-conductive electrolyte and enter the cathode material. The reverse occurs when charging the cell.

$$\begin{aligned} \text{Anode:} \quad & \mathrm{LiC_6} \longleftrightarrow \mathrm{Li^+ + e^- + C_6} \\ \text{Cathode:} \quad & \mathrm{Li^+ + e^- + CoO_2} \longleftrightarrow \mathrm{LiCoO_2} \end{aligned}$$

As stated earlier, batteries of HEVs are intended to assist the main power source in meeting the power demand especially during strong acceleration phases. In contrast to EVs, where the battery needs to be of sufficiently large energy in order to achieve the design driving range, the battery power capability is the main interest for HEV, not its energy. Being subject to high power pulses, another important aspect for HEV battery comes into play, which is its lifetime. The battery lifetime depends on the operating conditions (i.e., charge-discharge rate, depth-of-discharge and temperature [14, 15]) with few thousand cycles as a typical order of magnitude. These issues have lead to the fact that the HEV battery is usually oversized in terms of energy in order to fulfill the power and lifetime requirements.

In comparison to batteries, supercapacitors have a much higher specific power (up to 10 kW/kg) as shown in Figure 1.4, however, with significantly lower specific energy (few

Wh/kg) in comparison to 1-2 kW/kg and 50-100 Wh/kg, respectively, for the currently used HEV battery cells [16]. Additionally, supercapacitors have a higher efficiency and a much longer cycle life in the order of 1 million cycles. These characteristics make supercapacitors attractive as a candidate ESS in HEVs. The low energy density and the high cost of supercapacitors are the challenges to be overcome in future for a wider acceptance in HEV applications. Honda FCX [17] is an example of a FCHV using supercapacitors as an ESS. Maxwell Technologies and Nesscap are examples of the leading manufacturers of supercapacitors for automotive applications.

The operating principle of a supercapacitor (or ultracapacitor or also electric double-layer capacitor (EDLC)[5]) is depicted in Figure 1.5. A supercapacitor cell consists of two electrodes (typically of high surface-area activated carbon) ionically connected by an electrolyte composed of positive and negative ions solvated in a solvent such as water. When a voltage is applied to the cell, a double-layer is generated at each electrode-electrolyte interface, where one layer is in the electrode surface and the other layer is formed by the solvated electrolyte ions of the opposite polarity. The two layers are separated by the solvent molecules adsorbed to the electrode surface. Due to the large electrode surface area and the extremely thin double-layer distance, large capacitance (thousands of Farads per cell) can be obtained, enabling supercapacitors to store thousands of times more energy density than conventional electrolytic capacitors.

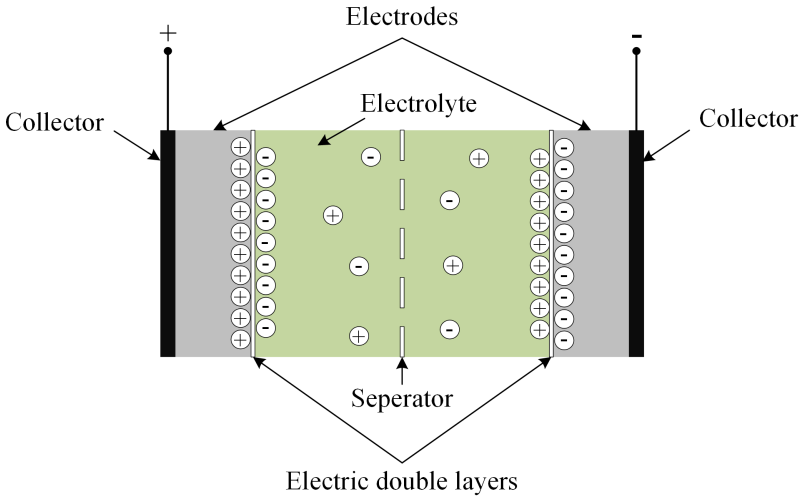

Figure 1.5: Construction of a typical supercapacitor.

1.4 Literature Review

The existence of multiple power sources in HEVs requires a power management strategy (PMS) that coordinates the power flow from the power sources. The PMS takes as inputs the driver request and system status (like speed and charge level of the energy buffer) and, based on that, distributes the request among the power sources. Since the market introduction of HEVs, there has been an extensive research on the PMS design

[5]EDLC is actually the most common type of supercapacitors. There are other types like pseudocapacitors and hybrid capacitors.

and optimization. The objective of any PMS design has been typically to exploit the advantages of hybridization by minimizing the fuel consumption and emissions (in case of ICE-based HEVs). Most literature has dealt with PMS design for conventional HEVs; however, the design and optimization approaches can be mostly adapted to FCHVs. Reviews of PMSs can be found in review articles such as [18, 19, 20, 21]. The proposed PMS design approaches in literature can be classified into three main categories: global optimization, real-time optimization, and rule-based strategies.

Global optimization techniques are the ones that seek the globally optimal PMS for a given cost function (e.g., fuel consumption) and a given load profile (i.e., driving cycle). To achieve the global optimal solution, these techniques require the whole driving cycle to be known; hence, the resulting optimal strategy is called off-line optimal. Dynamic Programming (DP) is a numerical optimization technique that makes use of the Bellman's Principle of optimality [22]. It is still the most common off-line optimization algorithm for HEVs [23, 24], for it guarantees the global optimum without any assumptions regarding the convexity or linearity of the system models. Pontryagin's Minimum Principle (PMP), based on the optimal control theory [25], has been applied to the power management optimization of HEVs [26, 27]. In comparison to DP, PMP gives only the necessary conditions that must be satisfied by the global optimum and not the sufficient conditions and, therefore, the PMP solution may be a local optimum. However, if the solution of PMP is unique, then it must be a global optimum. Convex optimization has been recently applied to HEVs optimization [28, 29]. It prerequires that the system can be described by a set of convex models and the accuracy of the optimal solution (in comparison to DP) depends on the accuracy of the approximations done to relax the non-convex behavior of the system, if any. In the same spirit, linear optimization (or linear programming) was used in [30] after approximating the cost functions and system model by linear relationships; here also the global optimality of the resulting strategy depends of the accuracy of the approximations.

The drawback of the off-line optimal PMS is that it is highly dependent on the driving cycle and, therefore, the optimal strategy over one driving cycle may result in a poor performance over other ones in real-time. Nevertheless, the off-line optimum has three main advantages: (1) it provides a benchmark for the real-time capable strategies, where the objective of any strategy designs is to be as close as possible to the off-line optimum. (2) The off-line optimum can give insight into the optimal system behavior, helping design and tune the real-time PMS. (3) It provides a tool for a fair and objective comparison between different powertrain topologies and powertrain sizes.

Stochastic dynamic programming (SDP) [31, 32] has been proposed to alleviate the cycle sensitivity of the deterministic DP. SDP considers a family of representative driving cycles, characterized by a sequence of speed and power demand, and a stochastic model (Markov chain model) of the speed and demand is generated. The SDP is then formulated as an infinite-horizon optimization problem, which results in a real-time capable PMS represented by time-invariant look-up tables. For a combination of system states (here power demand, vehicle speed and ESS charge level), the resulting control would be optimal in the statistical sense; in other terms, it is optimal for the most likely load sequence.

Real-time optimization modifies the global optimization problem into a sequence of instantaneous optimization problems at each time instance of the driving cycle. The

real-time optimization uses present system status and may use past information or even future information extracted from a navigation system. A very well-known example is the Equivalent Consumption Minimization Strategy (EMCS). EMCS was first proposed in [33] and further developed in [34, 35, 36]. It was shown in [37] that ECMS can be regarded as a real-time realization of PMP, so that EMCS and PMP are currently considered equivalent. Strategies based on model predictive control have been also devised [38, 39].

Rule-based strategies do not use optimization, rather a predefined set of rules, either deterministic [40, 41] or fuzzy [42, 43, 44], that distributes the demand among the power sources based on the present system status. The rules are derived heuristically from expert knowledge and may require significant tuning and testing effort. Such strategies require minimal requirements in terms of computation resources (i.e., time and memory); however, they do not offer any proof of optimality. The performance of the rule-based strategies can be improved by tuning their parameters to mimic the performance of the off-line optimal PMS [23]; alternatively, the parameters are optimized by means of evolutionary optimization algorithms, such as DIRECT (DIviding RECTangle) algorithm [45], genetic algorithm (GA) [46] or particle swarm optimization (PSO) [47].

All the aforementioned papers deal with one ESS system, mainly battery; nevertheless, the PMS design and optimization can be quite a complex task. Using two ESS systems (i.e., battery and supercapacitor) implicates an additional degree-of-freedom, further complicating the PMS design. As examples of literature dealing with fuel cell/ battery/ supercapacitor hybrid vehicular systems, DP [48] and convex optimization [29] have been used to get the off-line optimal PMS. Many real-time PMSs have been devised, they are, as examples, proportional-integral control [49, 50], fuzzy logic control [51, 52], deterministic rule-based control [53], and model predictive control [54].

The design of a HEV is a multi-level problem that includes the control design (i.e., PMS) and the plant design (e.g., size of the multiple power sources). For one power source, this source is sized according to the maximum required power by the vehicle to meet certain requirements such as acceleration time. With two or more sources, the sizing problem becomes less trivial. The main complexity comes from the fact that the two design levels (control and plant) are actually coupled. For example, the battery size can affect the PMS performance, and the PMS design may affect the optimal battery size for a given cost function. A comprehensive overview of coordination methods between plant design and control design can be found in [55].

The simplest plant design approach is to use a fixed PMS that is evaluated for each plant design, and look for the design that minimizes certain objective function(s) (e.g., fuel consumption, cost or both). The PMS typically takes the form of deterministic rules that stay the same during plant optimization; hence, the coupling between plant design and control design is neglected. The plant optimization algorithm can be a simple exhaustive search (all design candidates are evaluated and compared) [56] or an evolutionary optimization algorithm [57, 58, 59].

Considering the coupling between the plant design and control design have been approached by two coordination schemes: simultaneous and nested. In the simultaneous scheme, the plant parameters and control parameters are optimized simultaneously within one optimization loop. Convex optimization has been used to globally optimize the control and plant size simultaneously [28, 29]. Another possibility is to use evolutionary

optimization algorithms [45, 60], where the control parameters and plant parameters represent the optimization variables.

The nested coordination scheme uses two loops: an outer loop for the plant design and an inner loop for the controller design, so that the PMS is redesigned for each plant design evaluation. For the outer loop, exhaustive search has been used with DP [61], SDP [62] and PMP [63] for control optimization in the inner loop. An evolutionary algorithm was used in [64] in the outer loop together with DP as control algorithm.

1.5 Scientific Contribution

In the framework of this project, a number of scientific contributions to the literature were published. These are listed below. The publications i, iii and iv are peer-reviewed journal articles, whereas ii is a book chapter. In i, an experimental fuel cell/battery hybrid system is investigated in terms of the off-line optimal PMS and the optimization of the real-time PMS. A new formulation of the optimization problem for the real-time strategy is proposed taking into account multiple driving cycles in an attempt to improve the real-time PMS robustness. Additionally, two real-time PMS designs, i.e., PMP-based PI controller and Fuzzy controller, are compared. Publication ii reports an experimental study on the effect of the real-time PMS parameters on the performance of the hybrid system in terms of hydrogen consumption, battery charge sustenance and fuel cell system power dynamics. Publications iii (simulation) and iv (experiment) deal with the power management optimization of a triple hybrid system fuel cell/battery/supercapacitor for transit bus applications. In iii, a comparison between DP and PMP as two off-line optimization techniques is conducted, and a systematic approach, based on multi-objective optimization, is introduced for the optimization of the real-time strategy. In iv, an experimental study is conducted to validate the optimization techniques used in iii, and to compare a new real-time strategy with conventional strategies of literature.

i. **Odeim, Farouk**; Roes, Jürgen; Wülbeck, Lars; and Heinzel, Angelika. "Power management optimization of fuel cell/battery hybrid vehicles with experimental validation." *Journal of Power Sources* 252 (2014): 333-343.

ii. **Odeim, Farouk**; Roes, Jürgen; Wülbeck, Lars; and Heinzel, Angelika. "An experimental study on the power management optimization of fuel cell/battery hybrid drivetrains," in *Energy Science and Technology Vol. 10: Fuel cells and Batteries.* Studium Press LLC, 2015.

iii. **Odeim, Farouk**; Roes, Jürgen; Heinzel, Angelika. "Power management optimization of a fuel cell/battery/supercapacitor hybrid system for transit bus applications." *IEEE Transactions on Vehicular Technology* 65 (2016): 5783-5788.

iv. **Odeim, Farouk**; Roes, Jürgen; Heinzel, Angelika. "Power Management Optimization of an Experimental Fuel Cell/Battery/Supercapacitor Hybrid System." *Energies* 8, no. 7 (2015): 6302-6327.

The contributions of the thesis, including the aforementioned published papers, are summarized below.

- DP and PMP, as two off-line optimization techniques are compared for the three fuel cell-based hybrid powertrain topologies fuel cell/battery, fuel cell/supercapacitor and fuel cell/battery/supercapacitor. A special emphasize is given to the incorporation of the ESS charge constraints into PMP formulation, which is still considered an open issue in literature, particularly for a hybrid ESS composed of battery and supercapacitor.
- A new formulation is proposed for the optimization of the real-time strategy over multiple driving cycles at once, taking into account hydrogen consumption and charge sustenance in a framework of multi-objective optimization.
- An analytical study is conducted on the effect of battery efficiency on FCS optimal power dynamics.
- A new formulation is proposed for the real-time PMS optimization for fuel cell/ battery/ supercapacitor hybrids, taking into account hydrogen consumption, battery power and vehicle acceleration performance in a framework of multi-objective optimization.
- A new real-time strategy structure is proposed for the fuel cell/ battery/ supercapacitor hybrid and compared with similar strategies in literature.
- Several methods are discussed to incorporate the limitation of FCS dynamics in the off-line optimization.
- The sizing of the power sources is studied for fuel cell/battery and fuel cell/ supercapacitor hybrids, taking into account hydrogen consumption, cost, and drivability constraints (i.e., top speed, gradeability and acceleration time). The effect of battery aging on the sizing optimization is discussed.
- The proposed strategies and optimization methods are experimentally validated on a small-scale test bench.

1.6 Thesis Structure

The thesis deals with the power management optimization, both off-line and real-time strategies, and the sizing of fuel cell-based vehicles. The study on PMS design and optimization is carried out on two levels: the vehicle level and the test-bench level for validation. For fuel cell/battery and fuel cell/supercapacitor powertrains, a mid-size passenger vehicle is considered as an application, whereas a transit bus is considered for the fuel cell/battery/supercapacitor powertrain. The structure of the thesis is as follows.

Chapter 2 deals with fuel cell/battery vehicles in terms of PMS optimization and sizing. Firstly, the vehicle model is introduced. Then, the two off-line optimization techniques, i.e., DP and PMP, are comprehensively compared, and the off-line optimal strategy is analyzed. The sizing of the two power sources, i.e., FCS and battery, is then investigated. The optimization of the real-time strategy is subsequently presented. The chapter ends with an experimental validation.

Chapter 3 repeats the methods of the previous chapter, however, for a fuel cell/ supercapacitor powertrain. In the experimental study, incorporating of FCS dynamics limitation in the off-line optimization is addressed. In the end, alternative topologies are experimentally evaluated.

Chapter 4 deals with a fuel cell/battery/supercapacitor hybrid system for transit bus applications in terms of PMS design and optimization. The experimental study validates the proposed real-time strategy and its optimization and illustrates its advantages.

Chapter 5 summarizes the conclusions and findings of the study, and makes recommendations for future work.

Appendix A presents the bases and the theoretical background of the used off-line optimization techniques: Dynamic Programming and Pontryagin's Minimum Principle. Appendix B provides an introduction to the multi-objective optimization using a genetic algorithm, which is used extensively throughout the thesis. Appendix C introduces the Hardware-in-the-Loop test bench used for validation.

Chapter 2

Fuel Cell/Battery Hybrid

In this chapter, a fuel cell/battery hybrid powertrain for a mid-size passenger vehicle is investigated in terms of power management optimization and sizing. Section 2.1 introduces the model of the vehicle that enables the calculation of the power demand of the hybrid power source for standard driving cycles. In Section 2.2, two off-line optimization techniques, namely, Dynamic Programming (DP) and Pontryagin's Minimum Principle (PMP), are applied and compared in terms of the global optimality and in terms of the required computation resources. Further analysis of the off-line optimal strategy is conducted in Section 2.3. The sizing of power sources (i.e., fuel cells and battery) is addressed in Section 2.4, taking into account hydrogen consumption and cost. The design and optimization of a real-time capable power management strategy is introduced in Section 2.5. Experimental results obtained from a test bench are presented in Section 2.6.

2.1 Vehicle Model

The causality and main building blocks of the vehicle model are shown in Figure 2.1. The modeling approach used here is a combination of forward and backward calculations similar to the one used in ADVISOR [40]. The backward calculations, as the name suggests, starts by a required given speed profile, moves backward from the wheels to the DC bus and the various power sources. However, if the required power at the DC bus cannot be met by the power sources and/or the electric motor, the forward calculation path calculates the achievable speed. For most standard driving cycles and with a good power management strategy, the required power at the DC bus can be always fulfilled, so that the achievable speed matches exactly the required one. In some cases, however, those two speeds may differ, for examples, during harsh accelerations, and when the energy storage system is empty and the prime mover is unable to meet the power demand alone. The same models are used in the two calculation paths, however, with the inputs/outputs exchanged.

Following the backward calculation path, the model of vehicle dynamics accounts for the different forces acting on the vehicle mechanical curb for a give speed profile. The wheels model translates the net force and the required vehicle speed into required torque and

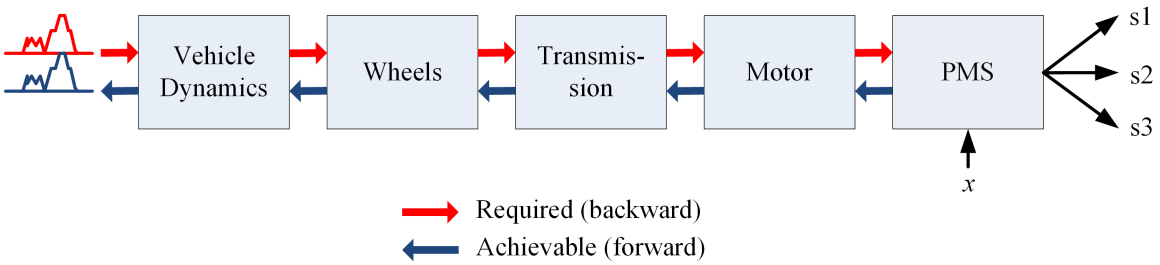

Figure 2.1: Causality and building blocks of the forward-backward vehicle model. x denotes the system states and s denotes a power source. Up to three power sources can exist in the powertrain.

required rotational speed at the wheels. With the help of the transmission line model, the required torque and rotational speed at the motor output is then obtained. The motor model calculates the required electric power at the DC bus, which is then distributed by the PMS among the power sources, while considering the system states (e.g., charge state of the energy storage system and vehicle speed).

The traction force, F_t, required at the wheels for a given speed is the sum of four forces [65]: the acceleration force, F_{acc}, the force required to overcome the aerodynamic drag, F_a, the force required to overcome the rolling friction with the road surface, F_r, and the gravity force, F_g, acting on the vehicle when driving on non-horizontal roads (up or downhill); i.e.,

$$\begin{aligned} F_t &= F_{acc} + F_a + F_r + F_g, \\ F_{acc} &= \left(m + \frac{\Theta_w}{r^2}\right)\frac{dv}{dt}, \\ F_a &= \frac{1}{2}\rho C_d A_f v^2, \\ F_r &= mgC_r\cos(\theta), \\ F_g &= mg\sin(\theta), \end{aligned} \tag{2.1}$$

where θ is the road angle that is set to zero for the evaluation driving cycles, and the other parameters are given in Table 2.1.

Given the traction force, the required torque at the wheels, T_w, and the wheels rotational speed, ω_w, are then obtained as follows:

$$\begin{aligned} T_w &= rF_t, \\ \omega_w &= v/r. \end{aligned} \tag{2.2}$$

The transmission line is modeled by its efficiency, η_{trans}, and gear ratio (reduction and differential), G. The required torque, T_m, and rotational speed, ω_m, of the motor are then given by:

$$\begin{aligned} T_m &= \begin{cases} \frac{T_w}{G\eta_{trans}}, & T_w \geq 0, \\ \frac{T_w\eta_{trans}}{G}, & T_w < 0, \end{cases} \\ \omega_m &= G\omega_w, \end{aligned} \tag{2.3}$$

where the positive torque corresponds to motoring phase and the negative torque corresponds to the regenerative braking phase. The motor and its inverter are modeled by

Table 2.1: Vehicle model parameters.

	Parameter	**Value**
Vehicle	Mass, m (kg)	1500
	Drag coefficient, C_d	0.3
	Frontal area, A_f (m^2)	2.2
	Auxiliary power, P_{aux} (W)	500
Wheels	Inertia, Θ_w($kg.m^2$)	3.3
	Radius, r (m)	0.31
	Friction coefficient, C_r	0.009
Transmission	Efficiency, η_{trans}	0.95
	Gear ratio, G	7.30
Motor	Max. torque (N·m)	271
	Max. speed (rpm)	10000
	Max. mechanical power (kW)	75
	Efficiency, η_m	Figure 2.2
Constants	Gravity constant, g (m/s^2)	9.81
	Air density, ρ (kg/m^3)	1.2

their combined efficiency, η_m, with which the required electric power of the motor, P_m, can be calculated as:

$$P_m = \begin{cases} \frac{T_m \omega_m}{\eta_m}, & T_m \geq 0, \\ \eta_m T_m \omega_m, & T_m < 0. \end{cases} \tag{2.4}$$

The total electric power at the DC bus, P_{dem}, is the sum of the motor power, P_m, and power required by the vehicle auxiliaries (e.g. air conditioning, power steering ...etc), P_{aux}; i.e.,

$$P_{dem} = P_m + P_{aux}. \tag{2.5}$$

This resulting power demand is distributed by the PMS among the different power sources.

Table 2.1 lists the vehicle parameters used in the simulation. The parameters are typical for a mid-size sedan. The induction motor MC-AC75 from ADVISOR database [40] is used. Its efficiency as a function of torque and rotational speed is shown in Figure 2.2. The gear ratio of 7.30 is selected in order for the maximum motor speed of 10000 rpm to correspond to 160 km/h top vehicle speed.

Standard driving cycles are commonly used to test the fuel economy and emissions (for ICE-based powertrains) of the vehicle. Four cycles, for passenger vehicles, are used here. Their speed profiles are shown in Figure 2.3 and their main characteristics are listed in Table 2.2.

New European Driving Cycle (NEDC) is the standard evaluation cycle in the European Union for passenger vehicles. It consists of four repetitions of the urban cycle ECE-15 (each lasts for 195 s) appended by the extra-urban cycle EUDC lasting for 400 s,

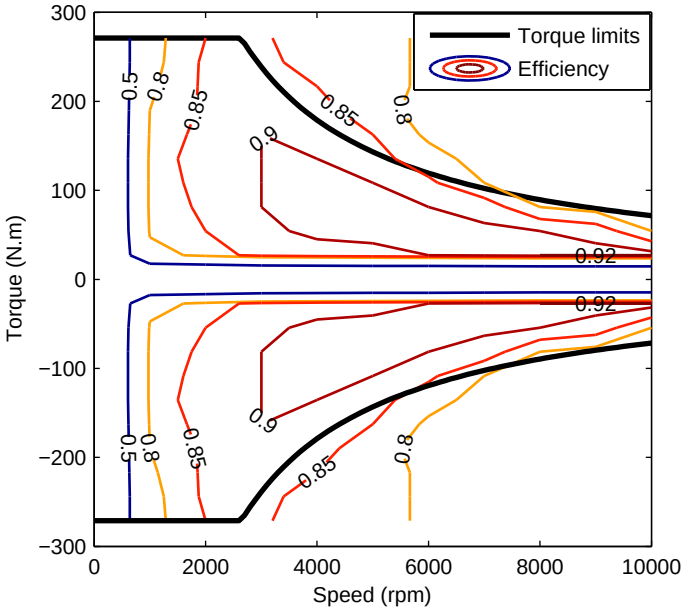

Figure 2.2: Efficiency map for MC-AC75 as a function of torque and rotational speed.

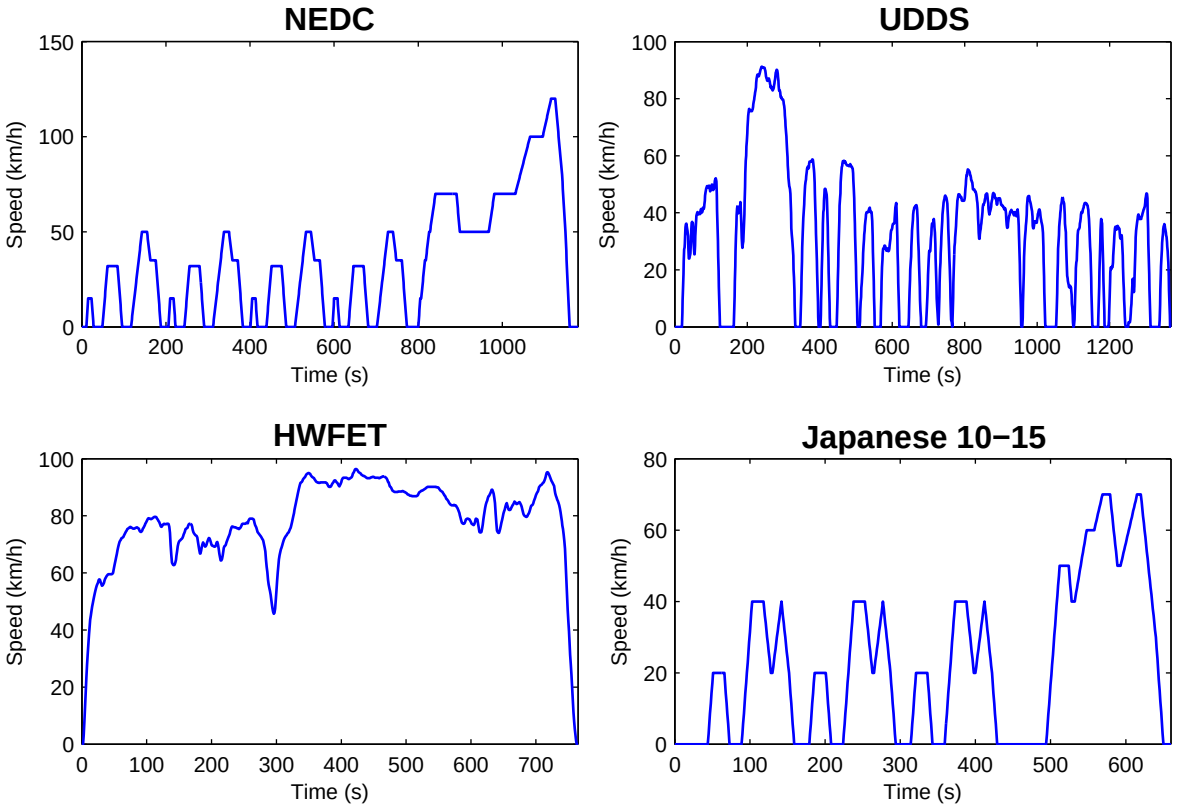

Figure 2.3: Speed profiles of the evaluation driving cycles.

Table 2.2: Selected characteristics of the evaluation driving cycles.

Characteristics	**Unit**	**NEDC**	**UDDS**	**HWFET**	**J. 10-15**
Distance	km	10.93	11.99	16.51	4.16
Duration	s	1180	1369	765	660
Speed (average/maximum)	km/h	33.32/120.00	31.51/91.25	77.58/ 96.40	22.68/ 69.97
Acceleration (average/maximum)	m/s^2	0.54/ 1.06	0.50/ 1.48	0.19/ 1.43	0.57/ 0.79
Deceleration (average/maximum)	m/s^2	-0.79/ -1.39	-0.58/ -1.48	-0.22 / -1.48	-0.65/ -0.83
Idle time	s	280	241	4	207
Stops	-	12	14	0	6

making in total a duration of 1180 s for the complete cycle. *Urban Dynamometer Driving Schedule* (UDDS) and *Highway Fuel Economy Test* (HWFET) are the standard test cycles in the United States. UDDS represents city driving, whereas HWFET simulates highway driving. *Japanese 10-15 Mode* (J. 10-15) has been the official test cycle in Japan. It consists of 3 repetitions of the so-called 10-mode segment followed by one 15-mode segment. This cycle has been recently replaced by the newer JC08 cycle.

As a result of the vehicle model, the required electric power at the DC bus for any driving cycle can be calculated, as shown in Figure 2.4 for NEDC. In the ideal case, where no aerodynamic drag, no rolling friction, no losses in the motor and transmission line and no auxiliary power, the total energy at the DC bus sums up to zero for a driving cycle that starts at standstill and ends up at standstill. This is because any energy spent to accelerate the vehicle would be compensated by the same energy recovered by the regenerative braking during deceleration. Due to the losses, the net energy is, however, positive, and this net energy should be supplied by the power sources. Figure 2.5 shows the contribution of different energy losses mechanisms in the vehicle over NEDC. At the end of NEDC, about 1.3 kWh is lost; about two thirds of which are needed to overcome the aerodynamic drag and friction, whereas about a quarter is lost in the motor and transmission. The rest is consumed by vehicle auxiliaries.

A schematic of the fuel cell/battery vehicle is shown in Figure 2.6. The battery is directly connected to the DC bus, whereas the FCS is coupled to the bus via a unidirectional

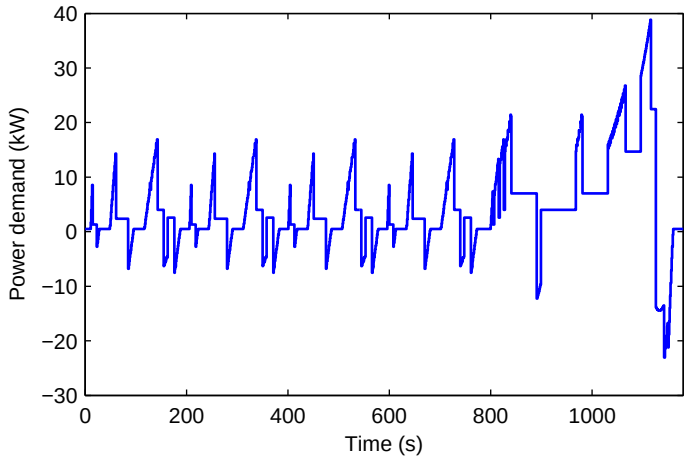

Figure 2.4: Power demand of NEDC as calculated by the vehicle model.

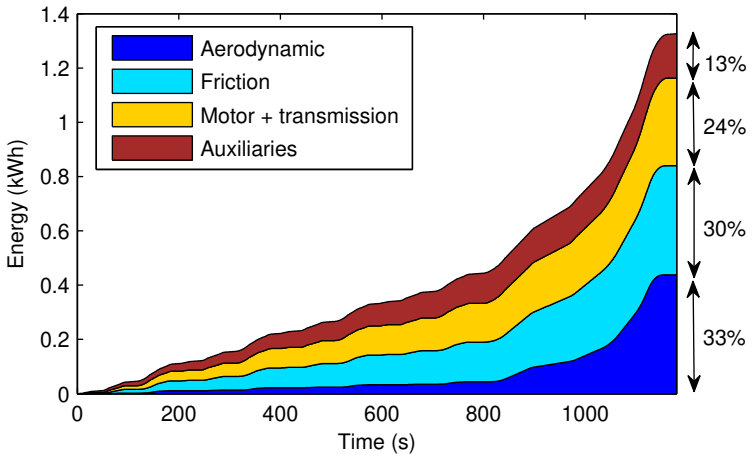

Figure 2.5: Energy losses over NEDC.

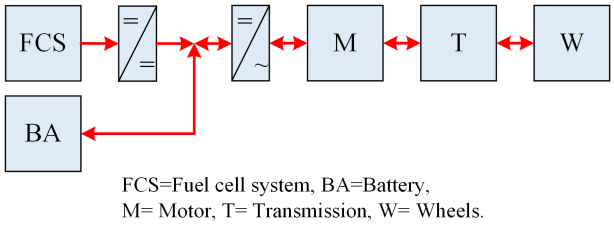

Figure 2.6: Schematic of fuel cell/battery hybrid powertrain.

DC/DC converter that enables the control of the FCS output power. The DC bus feeds the induction electric motor through an inverter. The motor shaft is coupled to the wheels through a single-speed transmission line that includes the reduction gearbox and the differential.

The FCS has a maximum power rating of 50 kW and it is modeled by its efficiency shown in Figure 2.7. The efficiency data, taken from [66], respects the DOE targets of a peak efficiency of 60% at 25% of the peak FCS power and 50% efficiency at full load, which are already achieved by the current automotive FCSs [67].

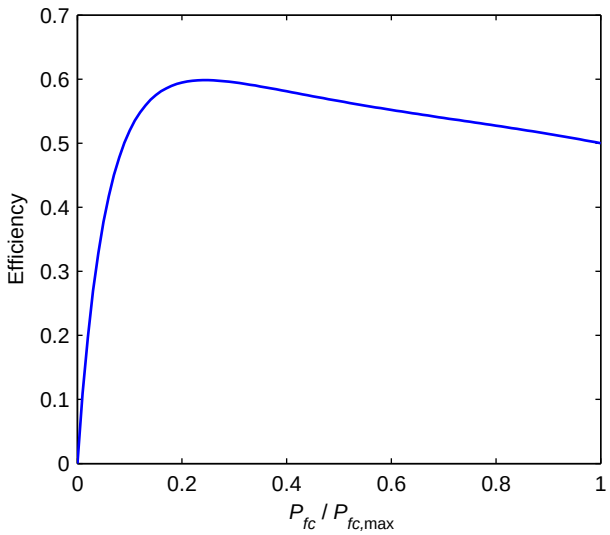

Figure 2.7: Efficiency of the fuel cell system.

The system efficiency is the ratio of system power, P_{fc}, to the hydrogen power, P_h, where P_h is the product of hydrogen mass flow rate, $\dot{m}_h$, and the hydrogen lower heating value, LHV (=120 kJ/g). The system has a peak efficiency of 60% at 25% of its power rating, and the efficiency decreases rapidly at lower power due to the idling power requirements of the system auxiliary components. The efficiency is also lower for high power levels due to the ohmic losses of the stack and the power loss by the auxiliaries, mainly, the air compressor which accounts for the major power loss. The FCS DC/DC converter is modeled by a constant efficiency of 95%. The start/stop operation of the FCS is not considered throughout the thesis. This means that when the FCS is delivering a zero power, the FCS auxiliaries stay in operation and the idle hydrogen consumption exists.

The building block of the battery bank is VL6P cell from Saft/Johnson Controls, which is used in hybrid vehicles of Mercedes-Benz [13]. Table 2.3 lists the main specifications of the battery cell. The battery is modeled by the internal-resistance model [68] whose equivalent circuit is shown in Figure 2.8(a), where OCV is the open circuit voltage of the battery, V_b, and R is its internal resistance, R_b. Two values of R_b are usually distinguished: one when charging the battery, $R_{b,chg}$, and the other when discharging it, $R_{b,dis}$. All the model parameters vary with the state-of-charge (SOC) as shown in Figure 2.8(b), where the data has been estimated from 10-second pulse power data in [13], as recommended in [69] for the determination of battery internal resistance. Sixty cells are connected in series to form the battery bank, so that the total energy content is 1.5 kWh and a no-load DC bus voltage of 220 V is obtained at 60% SOC.

Table 2.3: Selected characteristics of VL6P battery cell. Data from [13].

Characteristic	**Value**
Rated capacity	6.8 Ah
Mass	0.34 kg
Total energy	25 Wh
Current limits	250 A (discharge), 200 A (charge)
Voltage limits	2.5 – 4.1 V

2.2 Off-Line Optimization

As the name suggests, the off-line optimization aims at finding the optimal power sharing strategy between the two power sources over a known driving cycle, which achieves the minimum hydrogen consumption. The power demand P_{dem} should be fulfilled by the two power sources; i.e.,

$$P_{dem} = P_{fcdc} + P_b, \tag{2.6}$$

whereP_{fcdc} is the output power of the FCS DC/DC converter (P_{fc} is the FCS power), and P_b is the battery power. The objective of the optimization is to minimize the total hydrogen consumption over a given driving cycle, so the objective function to be minimized can be expressed as follows:

$$J = \int_0^{t_f} \dot{m}_h \left(P_{fcdc}\left(t\right)\right) dt, \tag{2.7}$$

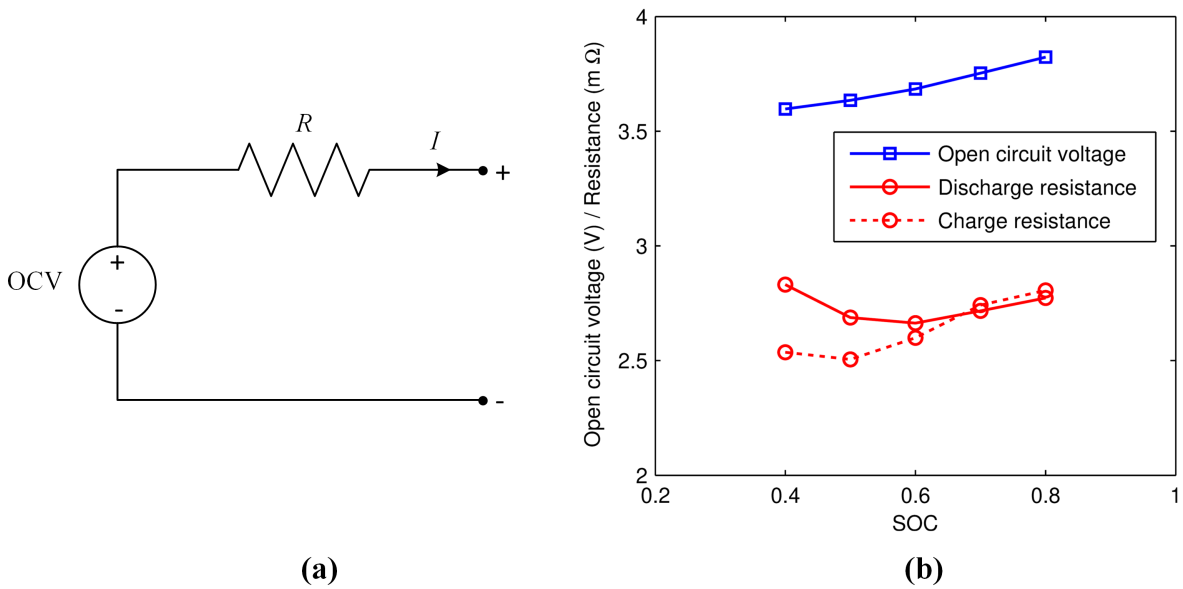

Figure 2.8: Internal-resistance battery model. (a) Model equivalent circuit; (b) Battery cell model parameters versus SOC.

where $\dot{m}_h$ is the hydrogen consumption rate and t_f is the duration of driving cycle. The battery state-of-charge evolves with time as follows:

$$\mathrm{SOC}(t) = \frac{Q(t)}{Q_b} = \mathrm{SOC}(0) - \frac{1}{Q_b}\int_0^t I_b(\tau)d\tau, \tag{2.8}$$

where $Q(t)$ is the remaining charge, Q_b is the battery charge capacity and I_b is the battery current, which is considered positive for discharging and negative for charging. From the internal resistance model, the SOC dynamics as a function of battery power is given by[1]:

$$\frac{d\,\mathrm{SOC}(t)}{dt} = \frac{-I_b(t)}{Q_b} = \begin{cases} \frac{-1}{2R_{b,dis}Q_b}\left(V_b - \sqrt{V_b^2 - 4R_{b,dis}P_b(t)}\right), & P_b(t) \geq 0, \\ \frac{-1}{2R_{b,chg}Q_b}\left(V_b - \sqrt{V_b^2 - 4R_{b,chg}P_b(t)}\right), & P_b(t) < 0. \end{cases} \tag{2.9}$$

The optimization problem is constrained by the power capabilities of the FCS and the battery. For example, the FCS power cannot be negative and it is limited to the FCS power rating, and the charging and discharging power of the battery are limited. Thus,

$$\begin{aligned} &P_{fcdc,\min} \leq P_{fcdc} \leq P_{fcdc,\max}, \\ &P_{b,\min} \leq P_b \leq P_{b,\max}. \end{aligned} \tag{2.10}$$

In addition to the power constraints, there are constraints on the battery SOC. First, the SOC is governed by the dynamic equation (2.9). Second, the SOC is not allowed to span

[1]Equation (2.9) can be derived as follows. Let V_b be the battery OCV, R_b its internal resistance, P_b its power and I_b its current, then we have: $P_b = I_b(V_b - R_bI_b)$. After rearrangement we get: $R_bI_b^2 - V_bI_b + P_b = 0$. This is a second-order equation with I_b as unknown; it has the solution: $I_b = \left(V_b - \sqrt{V_b^2 - 4R_bP_b}\right)/2R_b$.

the whole physical range of [0, 100] %, rather it is limited to a narrow range of 45% and 75%, so that the usable SOC range is 30% of the installed one. Those limits are imposed in order to prolong the battery lifetime. Additionally, the initial and final SOC over the driving cycle should be predefined. For HEVs, the charge-sustaining performance, where the initial and final states are identical, is used to evaluate the hydrogen consumption over the driving cycle.

A summary of the optimization problem objectives and constraints is given in Table 2.4. For a compact formulation of the problem, x is used to denote the battery SOC as a state of the system, and u is used to denote P_{fcdc} as a control variable (P_b can then be readily calculated by the power balance). The admissible control space $\mathbf{U}(t,x)$ represents the values that the control variable u can take at time t and state x; it is a function of power demand (and hence time) and battery SOC since the battery power limits depend on its SOC. The function f represents the equation (2.9). The dependency of f on the state comes from the fact that the battery model parameters are all functions of SOC. The constraints also include the definition of the initial state $x_0$and the final state x_f.

Table 2.4: Summary of the optimization problem objectives and constraints.

Objective:	$\min_u \int_0^{t_f} \dot{m}_h\left(u\left(t\right)\right) \mathrm{d}t.$
Constraints:	$u(t) \in \mathbf{U}(t,x),$
	$\dot{x}(t) = f(x(t), u(t), t),$
	$x_{\min} \leq x(t) \leq x_{\max},$
	$x(0) = x_0,$
	$x(t_f) = x_f.$

Dynamic Programming (DP) and Pontryagin's Minimum Principle (PMP) provide two tools to obtain the optimal power share over a given driving cycle. The two algorithms will be presented here.

2.2.1 Dynamic Programming (DP)

DP algorithm uses Bellmann's principle of optimality to efficiently solve the optimization problem (see Section A.1 for further information). The algorithm starts by discretizing the time span of the driving cycle into K+1 points with a sample time T_s. Two-dimensional state space is established, where one dimension corresponds to time and the second dimension corresponds to state (with M+1 levels and a state resolution of Δx), as shown in Figure 2.9.

At each time point k and each state grid point x^m, the cost-to-go function $J_k(x^m)$ is evaluated in a recursive manner moving backward in time as follows:

$$\begin{aligned} J_k(x^m, u_k) &= \dot{m}_h(u_k)T_s + J_k^*\left(x^m + T_s f(x^m, u_k, k)\right), \\ & \quad k = 0,\, 1,\, \ldots,\, K;\; m = 0,\, 1,\, \ldots,\, M. \end{aligned} \tag{2.11}$$

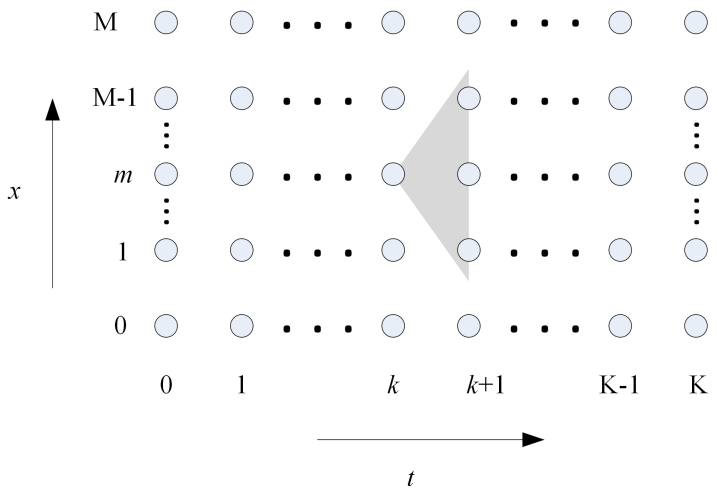

Figure 2.9: Working principle of Dynamic Programming.

The cost-to-go value associated to each control decision u_k is the sum of the cost of this decision (the hydrogen consumption over one sample time) and the optimal cost-to-go at time $k+1$ at the state reached by taking this control decision. By evaluating all the possible control decisions (with a resolution Δu), the minimum cost-to-go, $J_k^*(x^m)$, is obtained. As the name suggests, $J_k^*(x^m)$ represents the minimum hydrogen consumption that can be achieved starting from the state x^m at time point k and ending at the final state x_f at the final time point K. The term $(x^m + T_s f(x^m, u_k, k))$ represents the state achieved at time $k+1$ starting from state x^m at time k and taking the control decision u_k. It is possible that this achieved state does not belong to the state grid, whereas the optimal cost-to-go is available only at the state grid points. In this case, the optimal cost-to-go is calculated by linear interpolation between the nearest state grid points.

The final cost-to-go value, J_K^*, is set to zero for x_f and a large value otherwise in order to consider only the solutions that lead to x_f; i.e.,

$$J_K^*(x^m) = \begin{cases} 0, & x^m = x_f, \\ \infty, & x^m \neq x_f. \end{cases} \tag{2.12}$$

The result of the minimization is an optimal state-feedback control law that relates each state and each time point with the corresponding optimal control u^* that minimizes the cost-to-go; i.e.,

$$u_k^*(x^m) = \arg \min_{u_k \in \mathbf{U}(k,m)} J_k(x^m, u_k). \tag{2.13}$$

The optimal control map is then used to calculate the optimal DP solution moving forward in time starting from the predefined initial state. If necessary, the optimal control at states that do not belong to the state grid is evaluated also by linear interpolation.

In summary, DP follows, first, a backward calculation path, starting from the final time point. At each time point and each state point, all the possible control actions need to be evaluated in order to calculate the optimal cost-to-go function and the optimal control. Having calculated all the optimal control actions at all the points of the time-state space,

the forward calculation path starts with the given initial state to calculate the optimal control trajectory and the optimal state trajectory. This gives an impression on how extensive and time-consuming the calculations are.

DP guarantees the global optimum for an infinitely dense state gird and an infinitely fine control. The deviation from global optimum increases with decreasing the resolution in state grid and control. The effect of resolution on the solution optimality arises from the following factors. First, finite number of possible control actions is evaluated to calculate the cost-to-go function, and the optimal control is chosen among the tested actions. Second, as stated earlier, when evaluating the cost-to-go at time point k, linear interpolation between the optimal cost-to-go values at the next time point is required. Any non-linearity in the optimal cost-to-go at $k+1$ will cause an error in the evaluation of cost-to-go and therefore the resulting optimal control. Third, in the forward calculation of the optimal policy, also linear interpolation between the optimal actions at the state grid is used. Also here, the non-linearity in the optimal control will cause an error.

2.2.2 Pontryagin's Minimum Principle (PMP)

In contrast to DP, which can be regarded as a numerical algorithm, the PMP makes use of the calculus of variations to establish the necessary conditions of optimality (see Section A.2 for further information). It uses the concept of system Hamiltonian defined as follows:

$$H\left(x(t), u(t), \lambda(t), t\right) = \dot{m}_h\left(u(t)\right) - \lambda(t) f\left(x(t), u(t), t\right), \tag{2.14}$$

where the first term of the Hamiltonian is the instantaneous cost (i.e., hydrogen consumption rate) and the second term is the function f defined in equation (2.9)(i.e., dynamics of the state). The coefficient λ is the Lagrange multiplier, which is conventionally called co-state in the framework of PMP. In textbooks, a plus sign is used between the two terms; here a minus sign is used in order to get a positive co-state as will be seen.

The Minimum Principle states that the optimal control satisfies the following three necessary conditions:

$$\dot{x}^*(t) = -\frac{\partial H}{\partial \lambda}\left(x^*(t), u^*(t), \lambda^*(t), t\right) = f(x^*(t), u^*(t), t), \tag{2.15}$$

$$\dot{\lambda}^*(t) = \frac{\partial H}{\partial x}\left(x^*(t), u^*(t), \lambda^*(t), t\right), \tag{2.16}$$

$$H\left(x^*(t), u^*(t), \lambda^*(t), t\right) \leq H\left(x^*(t), u(t), \lambda^*(t), t\right). \tag{2.17}$$

The first necessary condition is nothing else than the system dynamics. The second condition determines the evolution of the optimal co-state with time. The third condition states that optimal control minimizes the Hamiltonian. Substituting the Hamiltonian of equation (2.14) into equation (2.16), we get:

$$\begin{aligned} \dot{\lambda}^*(t) &= \frac{\partial \dot{m}_h}{\partial x}\left(u^*(t)\right) - \lambda^*(t)\frac{\partial f}{\partial x}\left(x^*(t), u^*(t), \lambda^*(t), t\right), \\ &= -\lambda^*(t)\frac{\partial f}{\partial x}\left(x^*(t), u^*(t), \lambda^*(t), t\right), \end{aligned} \tag{2.18}$$

since the hydrogen consumption rate is not an explicit function of the state.

Since we have two dynamic equations to be solved, one for the state (i.e., equation (2.15)) and one for the co-state (i.e., equation (2.18)), the initial values of the state and co-state need to be given for the equations to be solved. The initial state is given by the statement of the problem as a constraint; however, the initial co-state is not given and need to be determined. By examining the formula of the Hamiltonian, the co-state plays a role of a weighting factor of the variations of the SOC (see Section 2.3.4 for more details). For high co-state values, the charging of the battery is favored and the final state-of-charge is higher than the initial one. For low values, the discharge is favored. Therefore, the optimal initial co-state depends on the constraint imposed on the final state-of-charge. So, to find the initial co-state an iterative procedure over the entire driving cycle is required. At the end of each iteration, the obtained final state is compared with the desired one, and the iterations stop once the final state constraint is satisfied. The fact that the final state increases with the initial co-state value, makes the search easy and within few iterations, the optimal value can be identified with a very good accuracy. A binary search algorithm is used to find the optimal initial co-state.

The numerical implementation of PMP proceeds as follows:

(1) Sampling the driving cycle with a sample time T_s (of 1 s). The samples are indexed by $k = 0 \dots K$;

(2) Define a first guess of the initial co-state $\lambda^*(0)$;

(3) For each power demand sample, $P_{dem}(k)$, the permissible control range is scanned and the corresponding Hamiltonian is evaluated with the aid of $\lambda^*(k)$. The control value that minimizes the Hamiltonian, $u^*(k)$, is applied;

(4) The state at the next sample time is calculated as follows:

$$x^*(k+1) = x^*(k) + T_s f(x^*(k), u^*(k), k);$$

(5) The co-state at the next sample time is calculated according to the forward Euler's integration method:

$$\lambda^*(k+1) = \lambda^*(k) - \lambda^*(k) T_s \frac{\partial f}{\partial x}(x^*(k), u^*(k), k);$$

(6) At the end of the driving cycle, $x^*(K)$ is compared to x_f. If $|x(K) - x_f| \leq \delta x$, then the solution is obtained. Otherwise, the algorithm is repeated with another guess of the initial co-state. δx is the tolerance on the deviation of the final state from the target one.

2.2.2.1 SOC Bounds Constraints

DP takes into account both control and state constraint, whereas PMP does not include, as stated, the state boundary constraint. There are several approaches used in literature to incorporate the state constraints into the formulation of PMP. Most approaches require

defining a new state and another co-state, which complicates the problem formulation, where the additional co-state requires careful tuning by trial and error [37], and such approaches may end up at many solutions that need to be compared in order to find the optimum [70].

If it is known that the optimal state trajectory hits the limits at known contact times, then the problem becomes straightforward. For example, let us assume that it is somehow known that the optimal state trajectory hits the upper state limit, $x_{\texttt{max}}$, at time t_c, whereas it lies within the limits otherwise. Then the problem can be divided into two problems: over the time span $[0, t_c]$ the unconstrained problem is solved for an initial state of x_0 and a final state of $x_{\texttt{max}}$. Over the time span $[t_c, t_f]$ the unconstrained problem is solved for an initial state of $x_{\texttt{max}}$ and a final state of x_f. The optimal solution of the complete problem results then from merging the two sub-solutions at the time t_c. So, solving the constrained problem can be reduced to solving a set of unconstrained problems once the contact times with the state limits are known a priori. However, the question that is still to be answered is how to determine those contact times, if any.

Dealing with the SOC boundary constraints uses a heuristic algorithm proposed in [26, 71], and validated by the author in [72]. The algorithm determines the contact times, where the optimal solution hits the limits, recursively. The algorithm proceeds as follows:

(1) Solve the unconstrained optimization problem over the entire driving cycle, and if the constraints are violated;

(2) Find the time instance t_1 where the state boundary is exceeded the most; i.e.,

$$t_1 = \arg \max_{t \in [t_0, t_f]} \left(x_{\texttt{min}} - x(t), x(t) - x_{\texttt{max}} \right);$$

(3) Split the time horizon into two parts $[0, t_1]$ and $[t_1, t_f]$. Calculate the unconstrained optimal solution at both parts, however, with different start and end state constraints as follows:

- In case the upper limit is exceeded, $x_{\texttt{max}}$ is used as an end state of the part $[0, t_1]$ and as a start state of the part $[t_1, t_f]$.
- In case the lower limit is exceeded, $x_{\texttt{min}}$ is used as an end state of the part $[0, t_1]$ and as a start state of the part $[t_1, t_f]$;

(4) If the unconstrained solution over any of the parts violates the limits, the subdivision of the time horizon is done within that part and the last two steps are repeated for that part;

(5) The algorithm stops when the solutions over all the state sub-trajectories satisfy the constraints. The optimal sub-trajectories are then joined together to form the complete solution.

As an example, Figure 2.10 illustrates the algorithm used to obtain the constrained PMP solution over UDDS with an initial state of 0.6 and a target final state of 0.6. Here the

lower SOC limit is taken 0.5 instead of 0.45, in order to make the difference between the constrained and the unconstrained solutions clearer. The PMP is applied first to the total driving cycles without constraints. The unconstrained solution exceeds the lower SOC limit at most at time step t_c=283 s. So, the optimization problem is solved twice; once over the time span [0,283] s with an initial state of 0.6 and a target final state of 0.5, and once over the time span [283,1369] s with an initial state of 0.5 and a target final state of 0.6. The solutions of the two sub-problems respect the constraints and, therefore, no further division is required. The resulting two sub-solutions are joined at the time instance t_c to form the complete solution of the constrained problem.

Figure 2.10 reveals an interesting behavior of the co-state, where it exhibits a discontinuity at the contact times. As discussed earlier, the co-state controls the difference between the final and initial states. Over the time span $[0, t_c]$, the unconstrained solution starts at 0.6 and ends up at 0.44, whereas the constrained solution ends up at 0.5, so the co-state of the constrained solutions is higher than that of the unconstrained solution. Over the time span $[t_c, t_f]$, both solutions end up at the same state of 0.6; however, the constrained solution starts at higher initial state and, therefore, the co-state of the constrained problem is lower than that of the unconstrained problem. This explains the step-down exhibited by the co-state at the contact time. Using the same reasoning, it can be expected that when the upper SOC limit is hit, a step-up is exhibited by the co-state at the contact time.

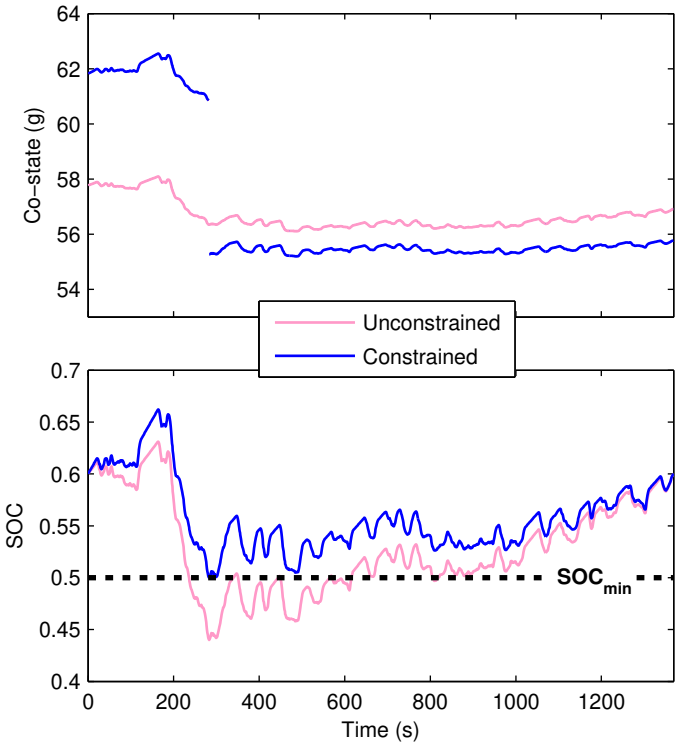

Figure 2.10: Steps to obtain the constrained PMP solution over UDDS.

2.2.3 Comparison Between DP and PMP

Both algorithms, DP and PMP, are compared in this section. For DP, a state resolution of 0.001 and a control resolution of 100 W are used. For PMP, a control resolution of 100 W is also used when scanning the admissible control actions while minimizing the Hamiltonian. A difference in the final SOC of 0.0001 is tolerated for PMP. Both algorithms are first compared in terms of achieved hydrogen consumption and resulting state trajectory. In [25], it is shown that there exists a relation between DP and PMP for an optimal solution, where the optimal co-state of PMP equals the partial derivative of the optimal cost-to-go function; i.e.,

$$\lambda^*(k) = \frac{\partial J_k^*}{\partial x}(x^*(k)). \tag{2.19}$$

This relation provides additional method to compare the two algorithms, where the optimal co-state trajectories calculated by the two algorithms can be also compared. For DP, the derivative of the optimal cost-to-go is approximated by the difference between state grid points in the vicinity of the optimal state at each time point.

Figure 2.11 shows a comparison between DP and PMP over NEDC for two different target final SOC: 0.6 and 0.55. The state trajectories of the two algorithms are almost identical. The same applies for the optimal co-state trajectories. The co-state of DP calculated from equation (2.19) is relatively dispersed at the end of driving cycle; this is attributed to truncation errors and the finite resolution used. For a final SOC of 0.6, the optimal state trajectory hits the upper SOC limit and, therefore, the co-state makes a step-up at the contact times (at time instances 802 and 807 s). For a final SOC of 0.55,

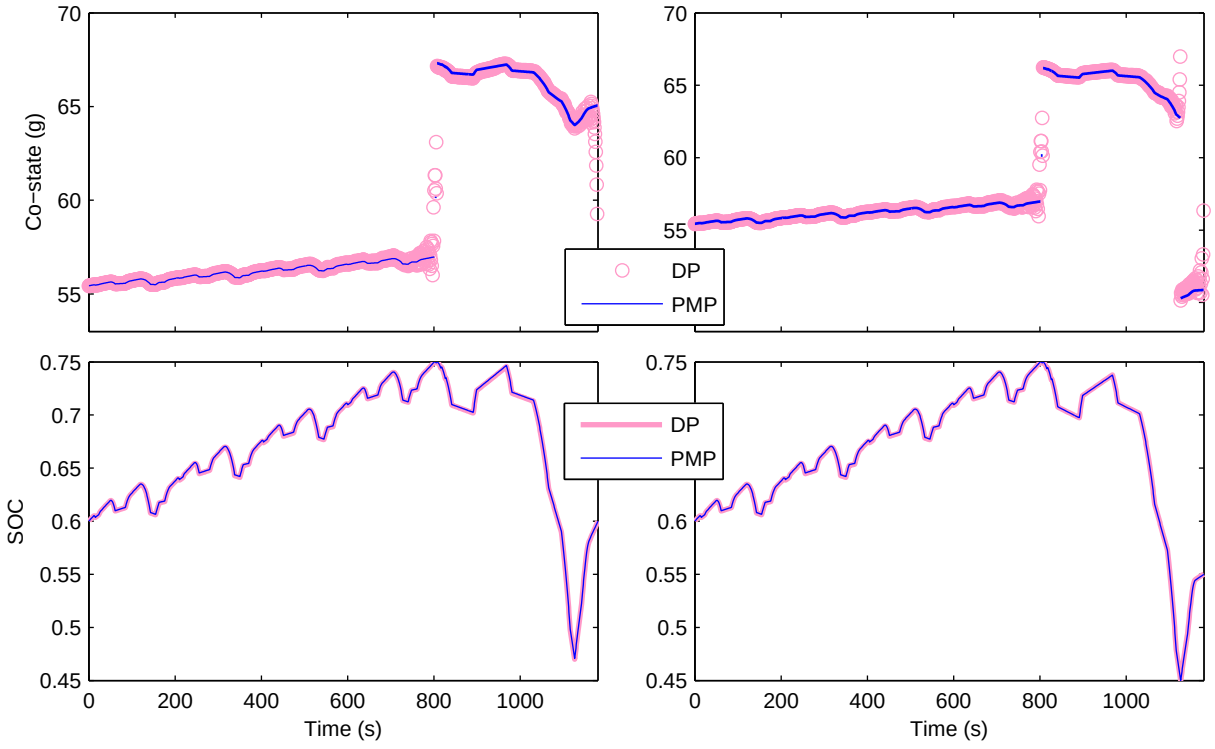

Figure 2.11: Comparison between DP and PMP in terms of state and co-state trajectories for (left) 0.6 and (right) 0.55 as a target final battery SOC over NEDC.

both upper and lower SOC limits are hit, and the co-state makes a step-down when the lower limit is hit.

Table 2.5 compares DP and PMP in terms of the achieved hydrogen consumption over the evaluation driving cycles. The figures of the two algorithms are practically identical.

Table 2.5: Comparison between DP and PMP in terms of hydrogen consumption.

Driving cycle	**DP (g)**	**PMP (g)**
NEDC	88.636	88.633
UDDS	94.542	94.540
HWFET	107.731	107.731
J. 10-15	38.507	38.507

For a complete comparison between DP and PMP, other important metrics need to be considered. The comparison is summarized in Table 2.6, where DP is used as a reference (denoted as •). Here are the details of the comparison.

- In terms of computation time and memory requirements, PMP requires negligible resources in comparison to DP. The exact time reduction depends on many factors like the state resolution and the code optimization. In our case, DP takes 66 s, whereas PMP takes 1.1 s over NEDC[2]. For a DP resolution of 0.01, the solution is obtained in 6.8 s, however, the hydrogen consumption becomes 89.347 g (0.8% increase). In terms of memory requirements, for DP, a map of $K\times(M+1)$ elements of the optimal control polices resulted from equation (2.13) are kept in memory for post processing (i.e., calculation of the optimal state trajectory starting from k=0), whereas only the initial optimal co-state is required for PMP post processing. For modern computers the memory requirement is not any more an issue. DP takes an acceptable time for a single energy storage (and hence one state and one control variable). The computation time and memory increase exponentially with the number of states and control variables. This phenomenon is usually referred to in literature as the "curse of dimensionality".

- State constraints simplify and reduce the computation time of DP since the cost-to-go function is required to be evaluated only on the allowed state range. In contrast, those constraints require additional non-trivial manipulations in PMP.

- PMP gives only the necessary conditions for optimality and not the sufficient conditions and, therefore, the PMP solution could be a local optimum. In contrast, the DP solution is guaranteed to be a global optimum for given state and control resolutions. The global optimality of PMP for hybrid vehicles was investigated by Kim *et al.* [73]. The PMP global optimality has been illustrated here by comparing the PMP solution with the DP solution.

- PMP solution has an interesting characteristic that makes it extendable to real-time. Ignoring the SOC limits, the optimal strategy over a driving cycle is reduced to one single number; that is, the initial co-state. In comparison, the calculation of

[2]Computer specifications: Intel(R) Core(TM) i5, 2.60 GHz CPU, 4.00 GB RAM.

the DP optimal strategy requires having the optimal control actions at all nodes of the state grid and all time points until the end of driving cycle. So, what is required for PMP at each sample time is a proper value of the co-state, then the minimization of the Hamiltonian can result in the corresponding control action. This feature of PMP will be used in the design of the real-time strategy in Section 2.5.

Table 2.6: Comparison between DP and PMP.

Metric	DP	PMP
Computation resources	•	+
SOC limitations	•	-
Global optimality	•	•
Real-time variant	•	+

2.3 Discussions

2.3.1 Constant Co-state

The dynamics of the optimal co-state is governed by equation (2.18). If the function f is independent of the state (i.e., the battery model parameters are constant independent of SOC), then the optimal co-state becomes constant. For HEVs in general, the battery is operated in a narrow SOC range, where the open circuit voltage and internal resistance do not vary significantly. As a result, it can be anticipated that a constant co-state can be a good approximation of the optimal co-state trajectory. For constant co-state, the same PMP algorithm is used as before but the step where the co-state is updated is skipped, and the initial guess of co-state is used over the entire driving cycle or part of it if the optimal trajectory hits the limits.

Figure 2.12 shows the optimal state and co-state trajectories for both variable and constant co-state over NEDC. In both cases, the co-state is discontinuous when the state trajectory hits the limit. A small difference in the state trajectory is observed. However, since the objective function is to minimize the hydrogen consumption in both cases, the best way to quantify the difference is to calculate the difference in hydrogen consumption. The constant co-state results in a very good approximation of the optimal hydrogen consumption with an error below 0.02% for all driving cycles. The constant co-state will be employed as an optimum in many places of the thesis.

2.3.2 Advantage of Hybridization

One of the main advantages of hybridization is the reduction of hydrogen consumption. The off-line optimal strategy provides the best hydrogen consumption and, therefore, it can be used to assess the potential hydrogen saving when moving from non-hybrid to hybrid powertrains. The potential hydrogen saving comes from two factors:

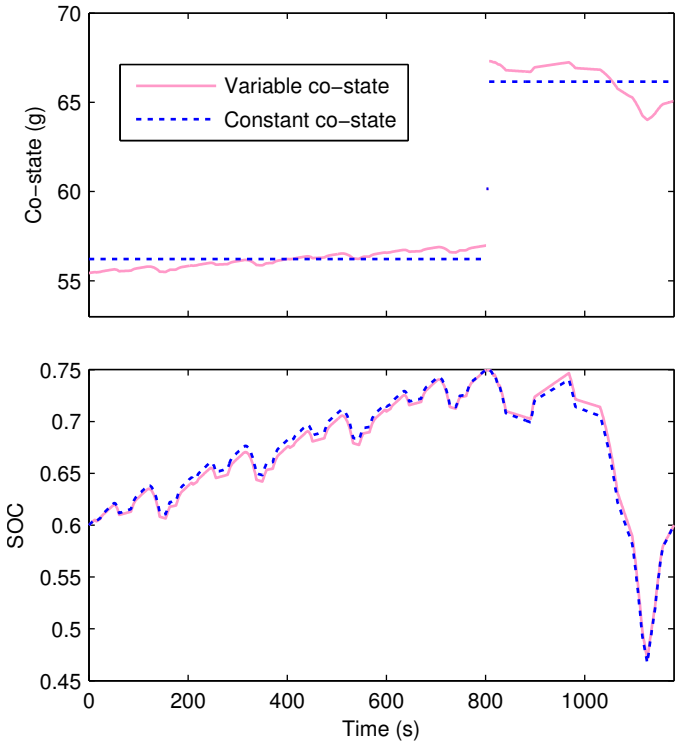

Figure 2.12: Comparison between variable co-state and constant co-state in terms of state and co-state trajectories over NEDC.

(1) Optimization of the operating points of the FCS and battery;

(2) Adding the possibility of regenerative braking, which is not possible for FCS as the only power source.

Figure 2.13 shows the hydrogen consumption of three scenarios: only FCS, hybrid without regenerative braking and hybrid with regenerative braking, and the percentage of hydrogen saving referenced to the non-hybrid. Here the vehicle parameters and power sources ratings are kept unchanged. The hydrogen saving of the second scenario in comparison to the first one is a result of optimizing the operating points of the FCS and battery (factor (1) above). The hydrogen saving of the third scenario in comparison to first one results from the two factors above. As it is clear, the major improvement of hydrogen consumption results from the regenerative braking. The hydrogen saving varies between driving cycles; it is highest for city cycles (like UDDS) where the amount of regenerative braking is highest, and it is lowest for highway cycles (like HWFET) which exhibit fewer braking phases.

In addition to hydrogen saving, the hybridization has other two advantages. First, without the battery, the FCS should be rated to provide the maximum driving power, whereas in the hybrid system, the FCS is sized to provide the cruising power demand and, therefore, the FCS can be downsized. Second, the dynamics of the FCS in the hybrid system is far much smoother, where the high dynamics is assigned to the battery, which results in an extension of the FCS lifetime.

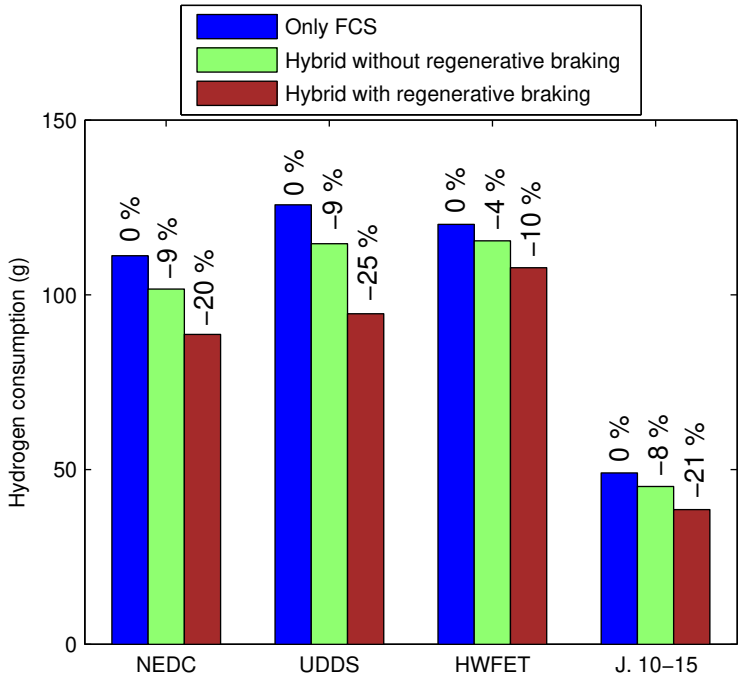

Figure 2.13: Effect of hybridization and regenerative braking on hydrogen consumption.

2.3.3 Optimization Window

The off-line optimization techniques can be used to find out, not only the best strategy, but also the worst strategy that achieves the maximum hydrogen consumption. The difference between the two strategies defines the limits of any other strategy, so that any strategy cannot be better than the best and cannot be worse than the worst. The worst strategy is calculated here with DP.

Figure 2.14(a) shows the best and worst hydrogen consumption over NEDC for variable final SOC between 0.55 and 0.65. The optimization window is quite large so that the worst consumption is about 55% higher than the best. It is interesting to note that the worst strategy is far much worse than the non-hybrid option (only FCS is used and no contribution from the battery). This can be interpreted as follows: adding the battery as an additional degree-of-freedom has the potential to significantly improve the hydrogen consumption; however, this degree-of-freedom can increase the consumption if it is used unwisely.

Figure 2.14(b and c) show the statistical distribution of FCS power for the best and worst strategies over NEDC for a final SOC of 0.6. The best strategy chooses favorable operating points of the FCS and battery in terms of efficiency, where the round-trip efficiency[3] of the battery is 93.6%. The worst strategy maximizes the hydrogen consumption by minimizing the amount of regenerative braking and by choosing the less favorable operating points, i.e., very low or very high power for FCS and the battery round-trip efficiency is 86.9%.

[3]The round-trip efficiency is defined as the ratio of the discharged energy to the charging energy over the driving cycle.

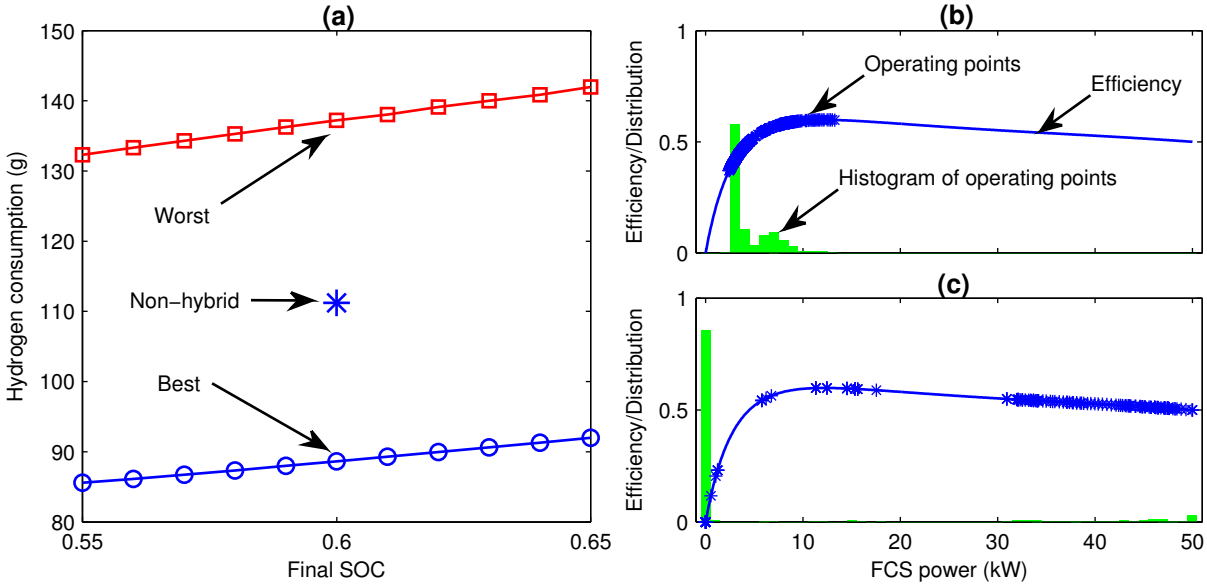

Figure 2.14: (a) Optimization window as a function of final SOC over NEDC; (b, c) Efficiency and FCS power distribution for the best (b) and worst (c) off-line strategies for a final SOC of 0.6.

2.3.4 Comments on the Co-state

From equation (2.14), the Hamiltonian is composed of two terms: the instantaneous hydrogen consumption rate and f representing the instantaneous state change rate, as follows:

$$H = \dot{m}_h + \lambda(-f) \quad : f = \dot{x}\,.$$

When minimizing the Hamiltonian to calculate the optimal control action, the co-state can be regarded as a weighting factor, which makes a compromise between the instantaneous hydrogen consumption and the instantaneous decrease in state.

This idea is illustrated graphically in Figure 2.15, which shows the ingredients of the Hamiltonian as a function of battery power for a power demand of 20 kW and a battery SOC of 0.6, for three different values of the co-state. With increasing the co-state, the term $(-\lambda f\ )$ rotates counterclockwise, and so does the Hamiltonian, making the optimal battery power (that minimizes the Hamiltonian) smaller. As example, increasing the co-state from 70.7 to 91.4 to 105.4 g decreases the optimal battery power between 10 kW (i.e., FCS and battery equally share the power demand) to 0 kW (FCS provides the demand alone) to -10 kW (FCS provides the demand and charges the battery). As a result, if over an extended time (e.g., driving cycle) a higher co-state is used, then the battery power will be always smaller and, therefore, the battery will exhibit less discharge (more charge) and the reached SOC will be higher. In contrast, if a smaller co-state is used over an extended time, the final SOC will be lower. In conclusion, the co-state controls the final SOC.

Actually, the variation of optimal co-state over a driving cycle is quite small if the SOC bounds constraints are ignored. Therefore, the initial co-state determines the final SOC. This is illustrated in Figure 2.16(a) for ECE-15 driving cycle. Three optimal state trajectories are depicted in Figure 2.16(b), with three initial co-state values of 45.0, 51.2 and

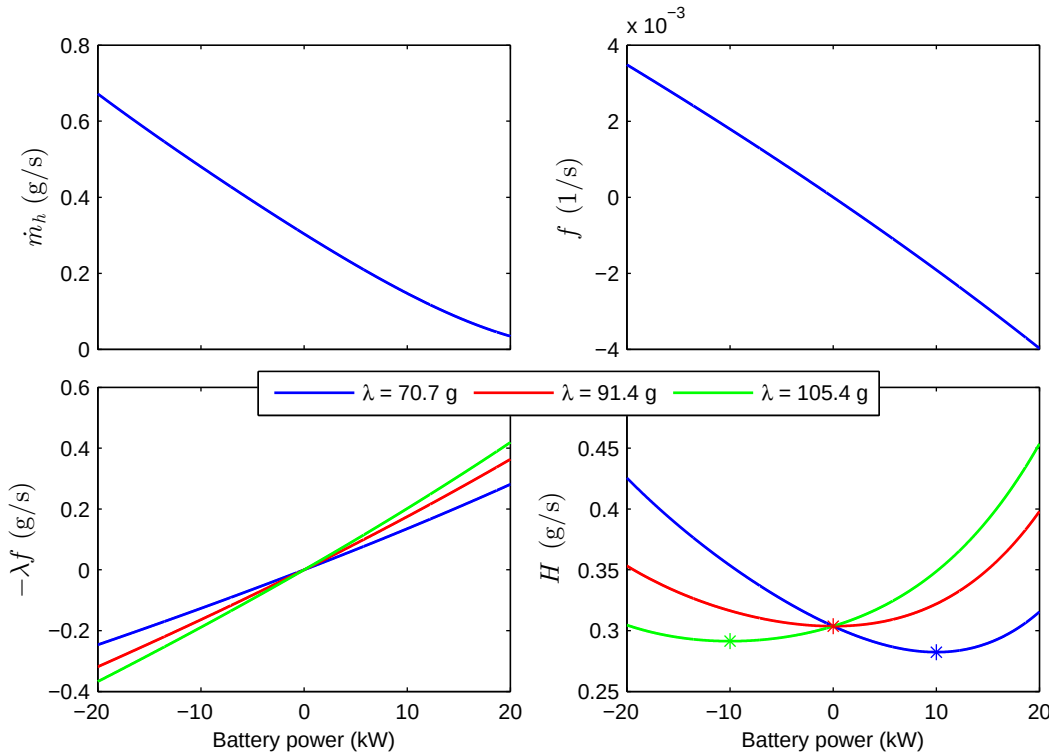

Figure 2.15: Example of the effect of co-state on the Hamiltonian and optimal battery power for a power demand of 20 kW and a battery SOC of 0.6.

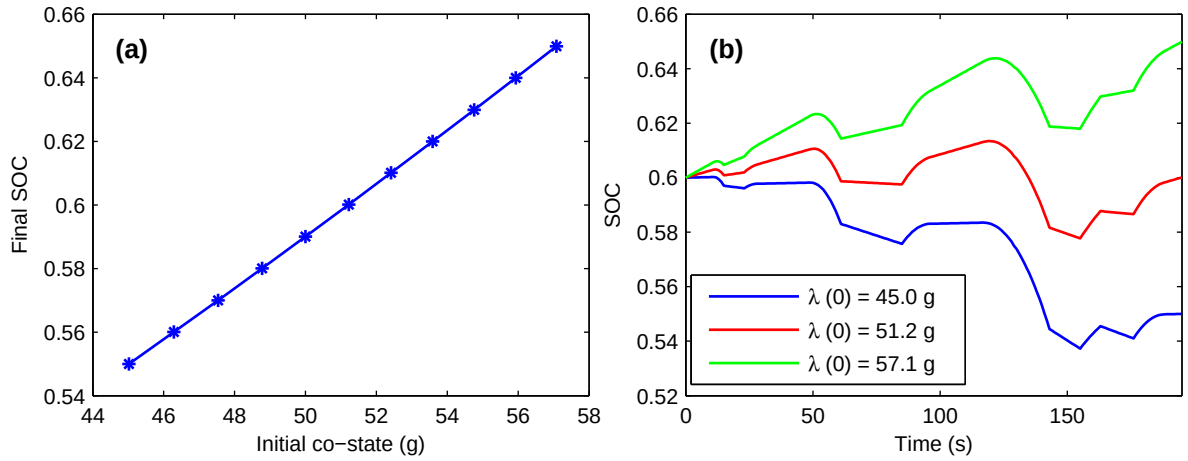

Figure 2.16: Effect of initial co-state on the final SOC over ECE-15. (a) Final SOC versus initial co-state; (b) Optimal SOC trajectories for three different initial co-state values.

57.1 g that lead to final SOC values of 0.55, 0.6 and 0.65, respectively. The final SOC becomes more sensitive to the initial co-state with increasing the duration of the driving cycle. For example, for 4 repetitions of ECE-15, the initial co-state varies between 49.7, 51.2 and 52.7 g for final SOC of 0.55, 0.60 and 0.65, respectively.

2.3.5 Effect of Battery Efficiency on FCS Optimal Dynamics

In this section, it will be shown that the dynamics of the optimal FCS power depends on the efficiency of the battery, so that decreasing the battery efficiency increases the

optimal FCS dynamics. Before proceeding with the analysis, It is necessary first to show that the hydrogen consumption rate is a strictly convex function of P_{fcdc}.

Neglecting the hydrogen losses due to purging and leakage, the hydrogen mass consumption rate $\dot{m}_h$ is related to stack current I_{st} by:

$$\dot{m}_h = \frac{N_{st} M_{H_2}}{2F} I_{st},$$

where N_{st} is the number of cells in the stack, M_{H_2} is the molar mass of hydrogen, and F is the Faraday constant. Considering the fact that the stack current is the stack power, P_{st}, divided by the stack voltage, V_{st}, and that P_{st} is the sum of FCS net power P_{fc} and the power consumed by the system auxiliaries, P_{aux}, and, moreover, P_{fc} is the sum of P_{fcdc} and the losses in the DC/DC converter, $P_{dc,loss}$, then the hydrogen mass flow rate can be expressed as follows:

$$\dot{m}_h = \frac{N_{st} M_{H_2}}{2F V_{st}} \left(P_{fcdc} + P_{dc,loss} + P_{aux} \right).$$

This relation shows that if V_{st}, $P_{dc,loss}$ and P_{aux} are all constants, then $\dot{m}_h$ increases linearly with P_{fcdc}. However, as it is known from experiment, V_{st} decreases with increasing FCS power according to the stack polarization curve and, additionally, $P_{dc,loss}$ and P_{aux} increase with P_{fcdc}. These effects add a convexity to the relation, making $\dot{m}_h$ a strictly convex function of P_{fcdc}.

Assuming the battery as an ideal voltage source with constant open circuit voltage and zero internal resistance, the Hamiltonian at a certain power demand and certain time instance is then given by:

$$H\left(P_{fcdc}, \lambda\right) = \dot{m}_h\left(P_{fcdc}\right) + \lambda \frac{P_b}{Q_b V_b} = \dot{m}_h\left(P_{fcdc}\right) + \frac{\lambda}{Q_b V_b}\left(P_{dem} - P_{fcdc}\right).$$

Since the Hamiltonian is independent of the battery SOC, the optimal co-state, λ^*, is constant over time. At the optimal P_{fcdc} and optimal λ, the Hamiltonian reaches its minimum. Ignoring the power constraints, then:

$$\begin{aligned} \frac{\partial H}{\partial P_{fcdc}}\left(P^*_{fcdc}, \lambda^*\right) &= \frac{\mathrm{d}\dot{m}_h}{\mathrm{d}P_{fcdc}}\left(P^*_{fcdc}\right) - \frac{\lambda^*}{Q_b V_b} = 0, \\ \Rightarrow \frac{\mathrm{d}\dot{m}_h}{\mathrm{d}P_{fcdc}}\left(P^*_{fcdc}\right) &= \frac{\lambda^*}{Q_b V_b}. \end{aligned}$$

Since $\dot{m}_h$ is a strictly convex function of P_{fcdc}, then the above equation has a single solution for a given λ^*. Since λ^* is constant, P^*_{fcdc} is constant independent of the power demand. Since the battery is lossless and the final SOC of the battery is the same as the initial one, then P^*_{fcdc} is nothing else than the average power demand, $P_{dem,av}$. The last formula gives also an analytical expression for the optimal co-state for a charge sustaining performance:

$$\lambda^* = Q_b V_b \frac{\mathrm{d}\dot{m}_h}{\mathrm{d}P_{fcdc}}\left(P_{dem,av}\right).$$

It should be noted that the last analysis holds also when the battery voltage varies with its SOC. This means that the optimal P_{fcdc} is constant also with a variable open circuit

voltage (however, with a zero internal resistance). The proof of the last case becomes simpler if the state-of-energy, rather than the state-of-charge, is used as a system state. Then $Q_b V_b$ is replaced by E_b (the battery energy capacity).

The conclusion of the aforementioned analysis is that the optimal P_{fcdc} is constant for a lossless battery. Actually, this conclusion can be reached without using the optimal control theory, rather using only the characteristic that $\dot{m}_h$ is a convex function of P_{fcdc}. Let $\{P_{fcdc}(k)\}$ be a sequence of controls with an average of $P_{fcdc,av}$. Since the battery is lossless, then using a constant control of $P_{fcdc,av}$ leads to the same final SOC as $\{P_{fcdc}(k)\}$. The hydrogen consumption of the sequence $\{P_{fcdc}(k)\}$ is given by:

$$J_1 = \sum_{k=1}^{K} T_s \dot{m}_h \left(P_{fcdc}(k)\right),$$

whereas using a constant control of $P_{fcdc,av}$ leads to hydrogen consumption of:

$$J_2 = K T_s \dot{m}_h \left(P_{fcdc,av}\right).$$

As it is known from the definition of the strictly convex function:

$$\begin{aligned} \dot{m}_h \left(P_{fcdc,av}\right) &< \frac{1}{K} \sum_{k=1}^{K} \dot{m}_h \left(P_{fcdc}(k)\right), \\ \Rightarrow J_2 &< J_1. \end{aligned}$$

This means that setting a constant control action results in the minimum hydrogen consumption. The cost increase (i.e., J_1 in comparison to J_2) increases with increasing the curvature of $\dot{m}_h$.

As a result, the dynamics of the optimal FCS power comes actually from the inefficiency of the battery. Figure 2.17(a and b) shows the optimal power distribution between the FCS and the battery over ECE-15 driving cycle for variable battery internal resistance between 0 and 4 times R_{base}, where R_{base} is the actual resistance of the used battery. For a zero resistance, the FCS power is constant equals to the demand average, whereas the battery takes the whole demand dynamics. With increasing battery resistance, the dynamics of FCS power increases. This can be explained if we look at the battery efficiency of Figure 2.17(c). With increasing battery resistance, the FCS takes more dynamics in order to decrease the losses in the battery by decreasing the battery power.

2.4 Sizing

In this section the effect of FCS and battery sizes on the vehicle performance will be discussed. The performance parameters considered are the drivability (i.e., top speed, gradeability and acceleration time), the hydrogen consumption and the hybrid power source cost. The parameters of the vehicle used so far will be used as reference and called "base plant design".

The method used for sizing the power sources is illustrated in Figure 2.18. Both hydrogen consumption and plant cost are evaluated for variable FCS size and battery size. The

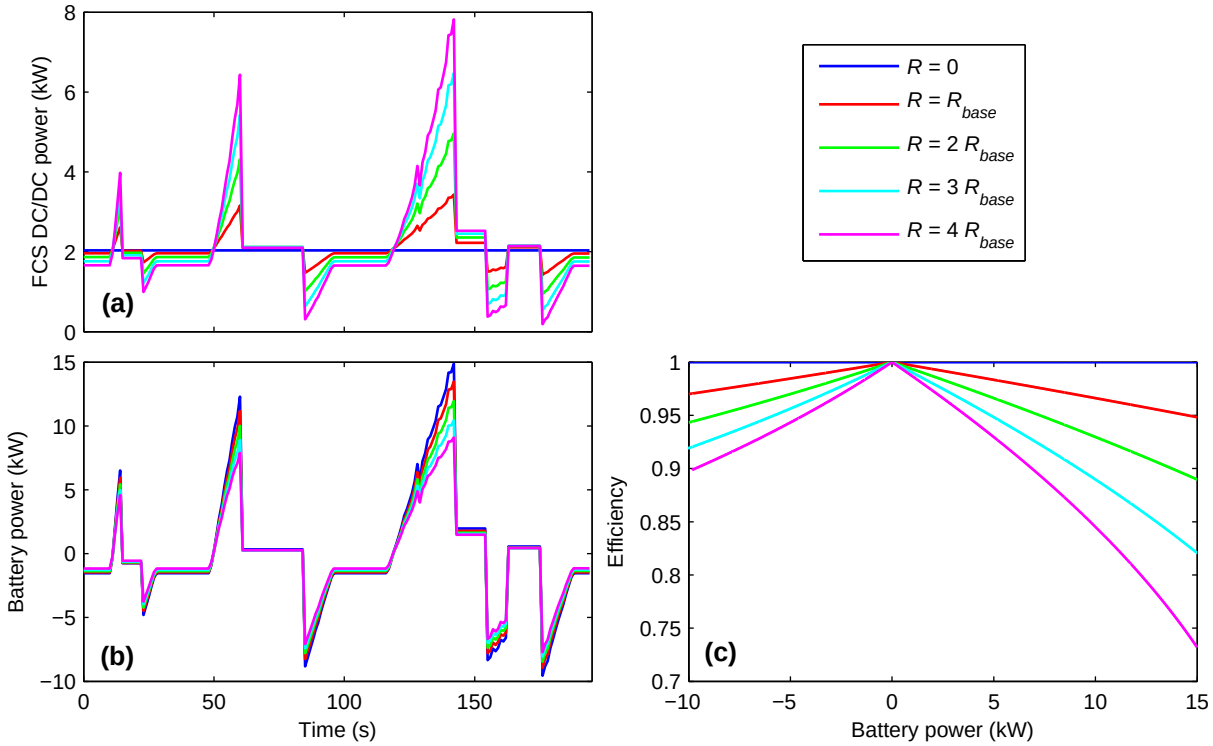

Figure 2.17: Effect of battery internal resistance on the FCS optimal power dynamics over ECE-15. (a) FCS converter power; (b) Battery power; (c) Battery efficiency.

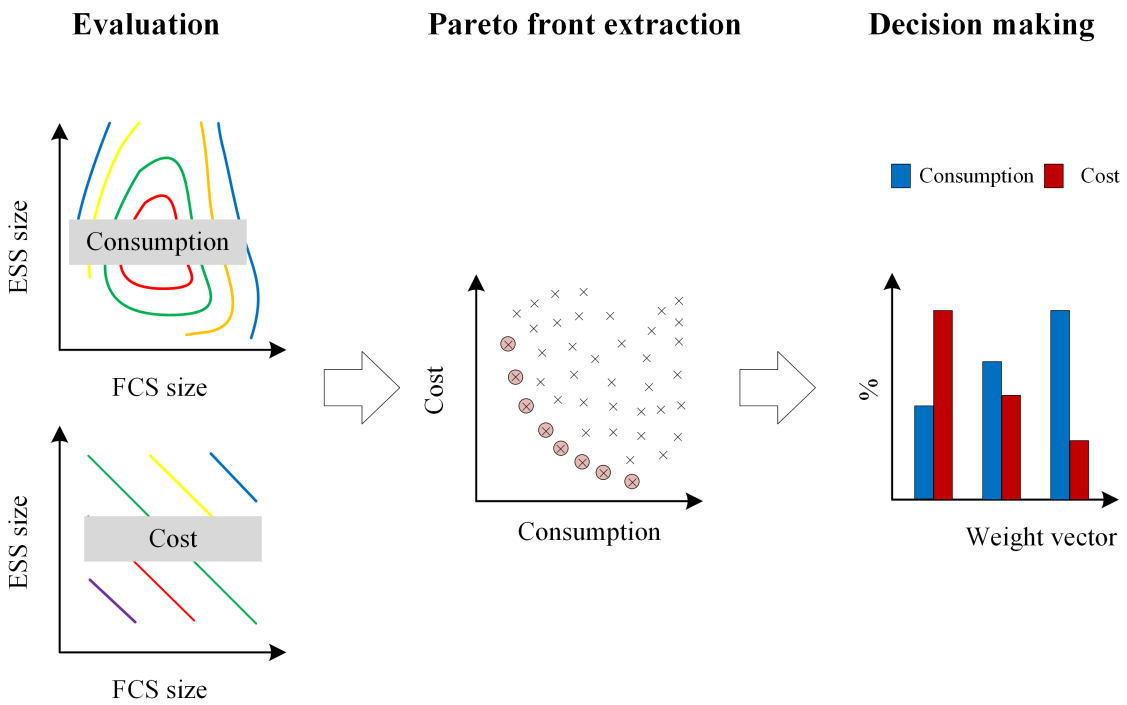

Figure 2.18: Procedure for sizing the hybrid power source of fuel cell/battery vehicle.

designs that represent the most efficient trade-off between the consumption and cost, i.e., the Pareto front, are then identified. By weighting the relative importance of consumption and cost, the decision maker chooses then one design among the Pareto front ones.

The variables of the sizing problem are the size of FCS and the battery capacity. The mass and cost of the power sources are given in Table 2.7. The size of FCS is defined by its power rating. The FCS mass is assumed to scale linearly with its power rating, and the same normalized efficiency shown in Figure 2.7 is used.

Table 2.7: Mass and cost scaling factors for the FCS and battery.

	Mass	**Cost**
FCS	2.5 kg/kW[4]	40 €/kW[5]
Battery	13.6 kg/kWh	800 €/kWh[6]

The battery size is varied by varying its capacity, whereas the number of cells is kept constant as it is determined by the DC bus voltage requirement. The battery mass is scaled linearly with its capacity with a scaling factor of 13.6 kg/kWh. This factor corresponds to the base plant design where the battery has an energy capacity of 1.5 kWh and weighs 20.4 kg (=0.34 kg/cell ×60 cells). With changing battery capacity, its internal resistance and maximum current also change as follows:

$$\begin{aligned} R_b &= R_b^{base}\frac{Q_b^{base}}{Q_b}, \\ I_{b,\max} &= I_{b,\max}^{base}\frac{Q_b}{Q_b^{base}}, \end{aligned}$$

where the battery resistance, R_b, (both charge and discharge resistances) scales linearly with the inverse of capacity. The battery maximum current, $I_{b,max}$, (both charge and discharge currents) scales linearly with the capacity. The superscript "base" refers to the base plant design.

In the sizing process, the FCS power rating is varied between 0 and 100 kW, and the battery capacity is varied between 0 and 20 Ah (corresponding to 0–4.4 kWh). The hydrogen consumption is evaluated using PMP. For that purpose, the FCS power rating range is divided into 21 values with a step of 5 kW. Likewise, the battery capacity range is divided into 21 values with a step of 1 Ah. PMP is then applied to calculate the best consumption for each pair of FCS power rating and battery capacity.

2.4.1 Drivability Constraints

The drivability is considered as a constraint of the sizing problem. Taking into account that the cost plays a major role for the majority of customers, very high top speed may

[4]This is the 2011 status of fuel cell vehicular systems according to [10].

[5]According to [74], the cost status for fuel cell vehicular systems is US$49 and US$47, for 2011 and 2012 respectively, per kW of net power based on projection to high volume manufacturing of 500000 units/year.

[6]Determined by a comprehensive consideration of [29, 56].

not be of interest for customers as long as it is acceptable, since speed limitations exist in most countries. This also applies to acceleration time, where very short times may also not be of interest as long as the vehicle accelerates in an acceptable time. This does not apply, for example, for sport vehicles, where the top speed and acceleration time are the major interest of the customers, whereas the cost plays a minor role.

Top speed represents the maximum speed that can be sustained on a horizontal road. The power sources are sized so that they achieve a minimum top speed of 140 km/h. The power required to sustain a specific speed over an extended time should be met by the FCS alone since the battery is used as an energy buffer and, therefore, it cannot deliver power for a long time. Therefore, the FCS power rating is the major determinant of the top speed, whereas the role of battery size comes solely from its effect on battery mass and hence on vehicle mass.

Gradeability corresponds to the maximum speed that can be sustained on a slope. The power sources are sized so that they achieve at least a maximum speed of 90 km/h on 6.5% grade with a payload of 300 kg. Like the top speed, the gradeability is mainly determined by the FCS power rating.

Figure 2.19 shows the maximum speed the can be sustained on a horizontal road and on a grade of 6.5% with payload as a function of FCS power rating. The maximum speed is limited to 160 km/h by the motor. The curves are shown as areas, where the base line of each area represents a 20 Ah battery and the top line represents the case of no battery (0 Ah). With increasing battery size, the vehicle mass increases and, therefore, bigger FCS is required to sustain a certain maximum speed. The effect of mass is more important for a grade of 6.5% than for a grade of 0%, since for the former case the mass-dependent gravity force attributes significantly to the traction force.

Acceleration time represents the minimum time required to accelerate the vehicle from standstill to 100 km/h. An upper limit of 12 s is used as a constraint for the power sources size. Figure 2.20 shows the speed profile and motor power demand during a

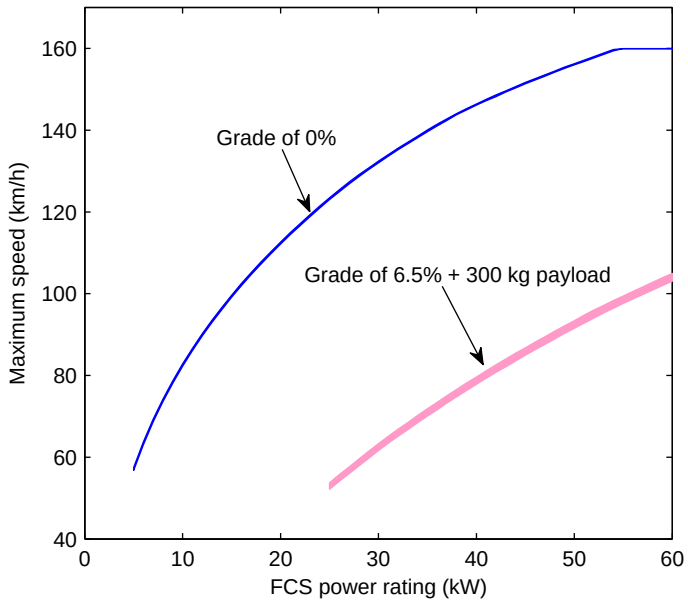

Figure 2.19: Maximum speed as a function of FCS power rating.

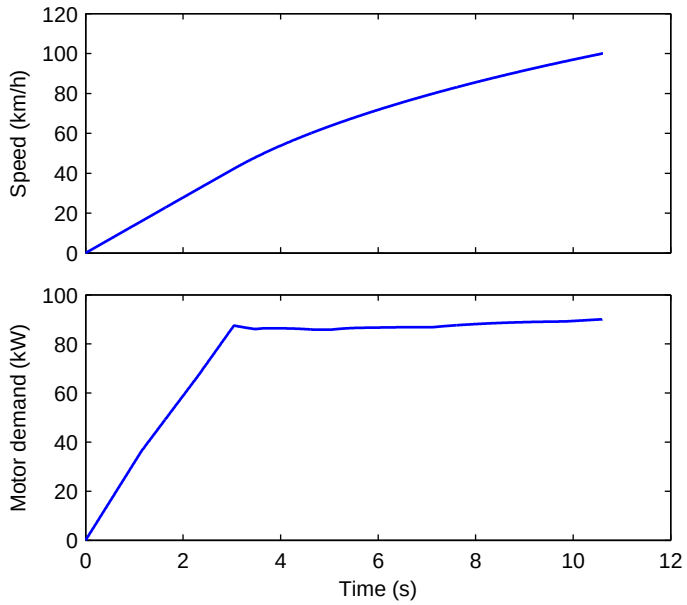

Figure 2.20: Speed profile and motor demand during the maximum acceleration 0–100 km/h.

strong acceleration 0–100 km/h, which is achieved by the base plant design within 10.6 s. for relatively small power sources, the demand may not be possible to meet, which leads to prolonging the acceleration time. For the evaluation of acceleration time a sample time of 0.1 s is used (in comparison to 1 s for driving cycles) in order to improve the accuracy. During acceleration, the FCS delivers the load alone when it is possible; otherwise, when the demand exceeds the FCS capability, the battery delivers the rest demand as long as it is able to do that according to its power capability and available energy. The battery is assumed at 60% SOC at the beginning of acceleration.

The constraints used for the drivability are closely related to the commonly used PNGV (Partnership for a New Generation of Vehicles) requirements of hybrid vehicles, which set a minimum top speed of 85 mph (= 136.8 km/h), a minimum top speed of 55 mph (= 88.5 km/h) at 6.5% grade, and 12 s as a higher limit of the minimum acceleration time from standstill to 60 mph (= 96.5 km/h) [75].

Figure 2.21 shows the lines that represent the minimum sizes that achieve each constraint, so that to the left of each line, the corresponding constraint is not satisfied, and to the right of each line, the corresponding constraint is satisfied. The area to the left of all lines represents the insufficient sizes that violate at least one of the constraints. The top speed is a weaker constraint than the gradeability, so that the solutions that satisfy the gradeability constraint necessarily satisfy the top speed constraint.

2.4.2 Results and Discussion

Figure 2.22(a) shows the results of hydrogen consumption over NEDC, where the hydrogen consumption is displayed as isolines with labels indicating the hydrogen consumption in gram. The dark gray represents the impossible sizing, where the speed profile of the driving cycle cannot be followed completely, whereas the light gray highlights the region of insufficient sizing, where the drivability constraints are violated. Figure 2.22(b) shows

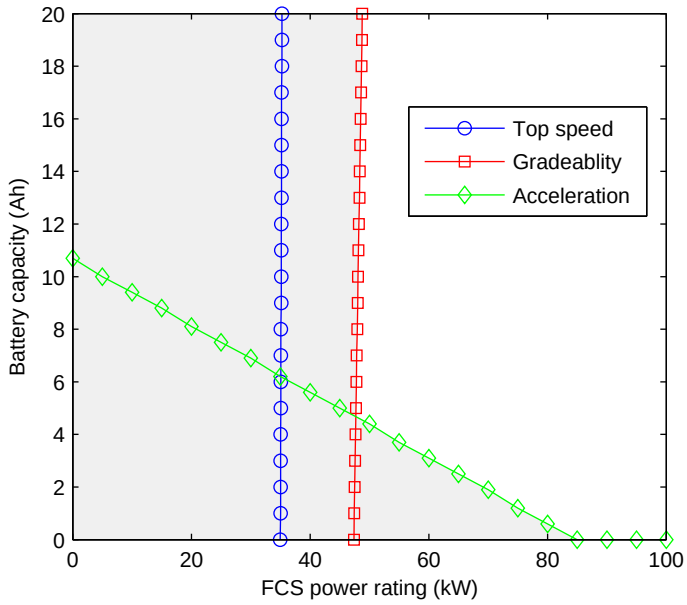

Figure 2.21: Limits of FCS power rating and battery capacity that fulfill the drivability constraints. The grayed area represents the insufficient sizing in terms of drivability.

the effect of FCS power rating on hydrogen consumption for a battery capacity of 6.8 Ah, and Figure 2.22(c) shows the effect of battery capacity on consumption for an FCS power rating of 50 kW. The same analysis is depicted in Figure 2.23 for HWFET. The results over the two driving cycles can be summarized in the following observations:

- The effect of the battery capacity increase on hydrogen consumption is significant at low capacities (<5 Ah), whereas it is marginal at high capacities. At low capacities, increasing the capacity increases the amount of regenerative braking which accounts for the main hydrogen saving. At high capacities, two contradicting effects are taking place, so that increasing the capacity decreases the battery internal resistance (leading to lower losses in the battery and, therefore, lower consumption), however, increases the battery mass and hence the vehicle mass leading to higher consumption. The latter effect is quite small since the battery mass is already small (i.e., for 0 Ah and 20 Ah, the battery mass is 0 and 60 kg, respectively). For a moderate FCS power rating around 50 kW, the acceleration constraint has an advantageous side-effect of setting a minimum battery capacity leading to relatively low consumption.
- The effect of FCS power rating on hydrogen consumption comes from two main factors. First, increasing the FCS power rating increases the vehicle mass (by 250 kg for FCS power rating between 0 and 100 kW). Second, varying the FCS power rating shifts the FCS power that accepts the peak FCS efficiency. The minimum hydrogen consumption is achieved when the FCS power rating is about four times the average demand, since then the average demand coincides with the peak efficiency. The minimum consumption over NEDC is obtained for an FCS power rating of 15 kW, where the average demand is 4.0 kW. The minimum consumption over HWFET is obtained for an FCS power rating of 35 kW, where the average demand is 9.3 kW.

Each pair of FCS power rating and battery capacity represents a possible plant de-

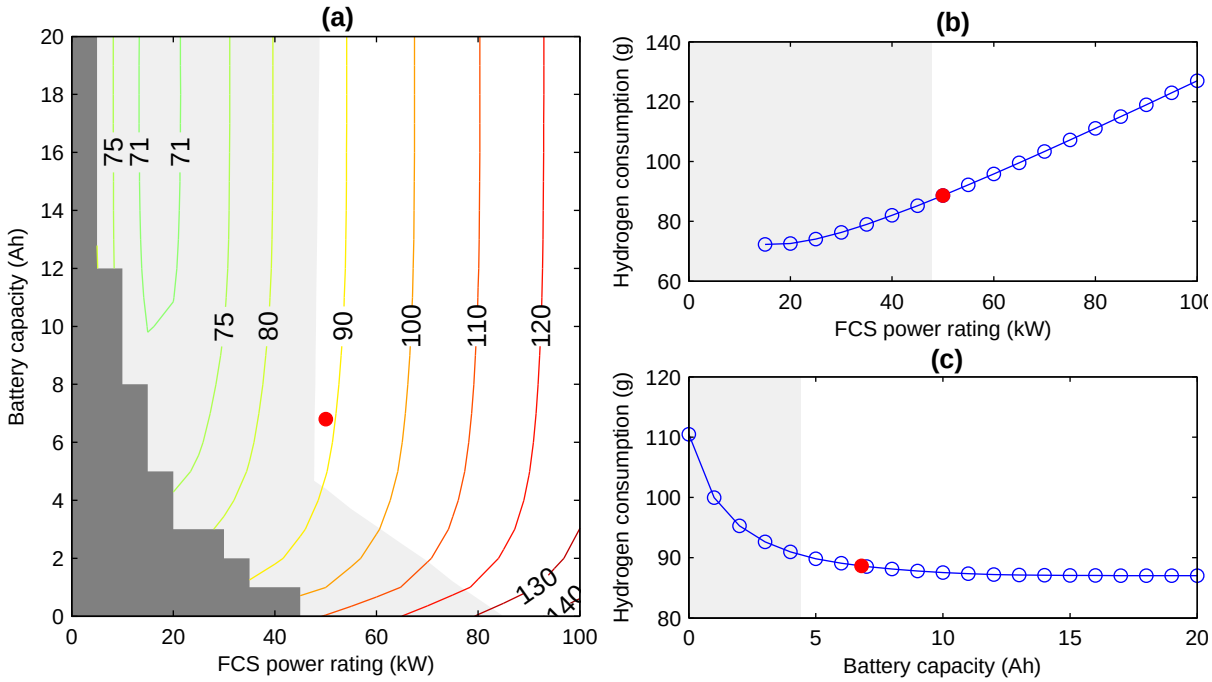

Figure 2.22: Hydrogen consumption versus FCS power rating and battery capacity over NEDC. (a) Consumption isolines in gram; (b) Consumption versus FCS power rating for battery capacity of 6.8 Ah; (c) Consumption versus battery capacity for FCS power rating of 50 kW. The red circle marks the base plant design.

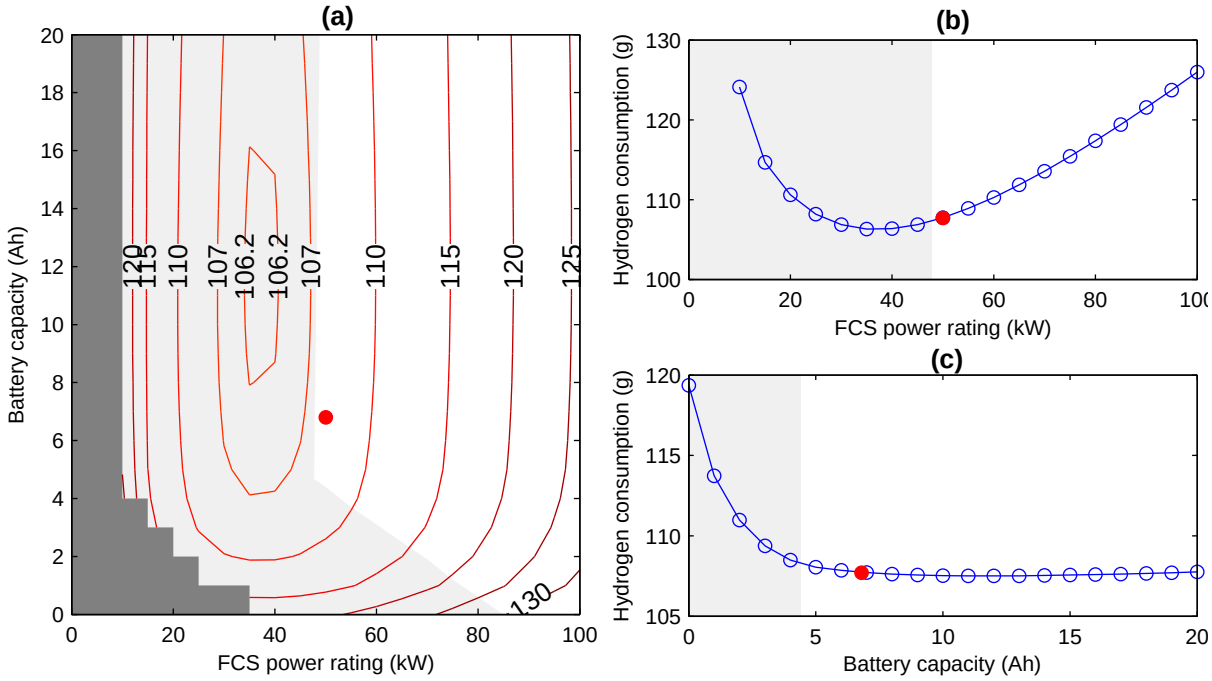

Figure 2.23: Hydrogen consumption versus FCS power rating and battery capacity over HWFET. (a) Consumption isolines in gram; (b) Consumption versus FCS power rating for battery capacity of 6.8 Ah; (c) Consumption versus battery capacity for FCS power rating of 50 kW. The red circle marks the base plant design.

sign, with a corresponding performance in terms of cost and hydrogen consumption. Figure 2.24 shows, for example, the performance of all possible designs (termed "unconstrained") in the cost-hydrogen consumption plane. The solutions that respect the drivability constraints represent a subset (termed "constrained") of the possible solutions. Considering the hydrogen consumption and the cost as two objective functions to be minimized, the designer would be interested only in the designs that achieve the best trade-off between the two objectives. The best trade-off is called Pareto front, which is a collection of the non-dominated solutions. In order to test a solution whether it belongs to the Pareto front (i.e., whether it is a Pareto solution), the solution is compared with all the other solutions. If the solution is not dominated by any other solution, then it belongs to Pareto front. So, for each driving cycle, two Pareto fronts are obtained: a global unconstrained one and a constrained one as shown in Figure 2.24. Any non-Pareto solution corresponds to an inefficient design that unnecessarily increases the cost and/or hydrogen consumption.

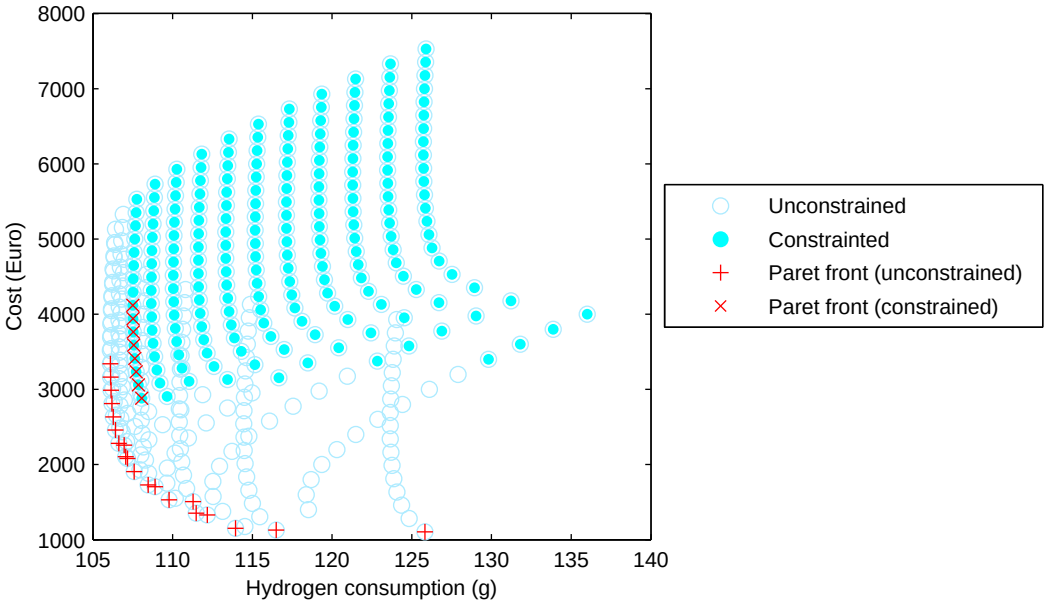

Figure 2.24: Extraction of Pareto fronts for HWFET.

Figure 2.25 shows the Pareto solutions in the decision space (FCS power rating and battery capacity) for the two driving cycles. In other terms, Figure 2.25 shows the most efficient designs in terms of cost and hydrogen consumption with and without drivability constraints. For the two driving cycles, there is no intersection between the unconstrained and constrained Pareto solutions. This is attributed to the fact that the minimum hydrogen consumption is obtained for designs outside the constrained region.

All the solutions of Pareto front are mathematically equally optimal. Choosing one solution rather than the others requires weighing the relative importance of the two objective functions: cost and hydrogen consumption. For each Pareto solution x of the decision space, the weight w_i for the i-th objective function can be calculated as follows [76]:

$$w_i = \frac{\left(f_i^{\max} - f_i(x)\right) / \left(f_i^{\max} - f_i^{\min}\right)}{\sum_{m=1}^{2} \left(f_m^{\max} - f_m(x)\right) / \left(f_m^{\max} - f_m^{\min}\right)}, \tag{2.20}$$

where $f_i^{\max}$ and $f_i^{\min}$ are the maximum and minimum values, respectively, of the i-th

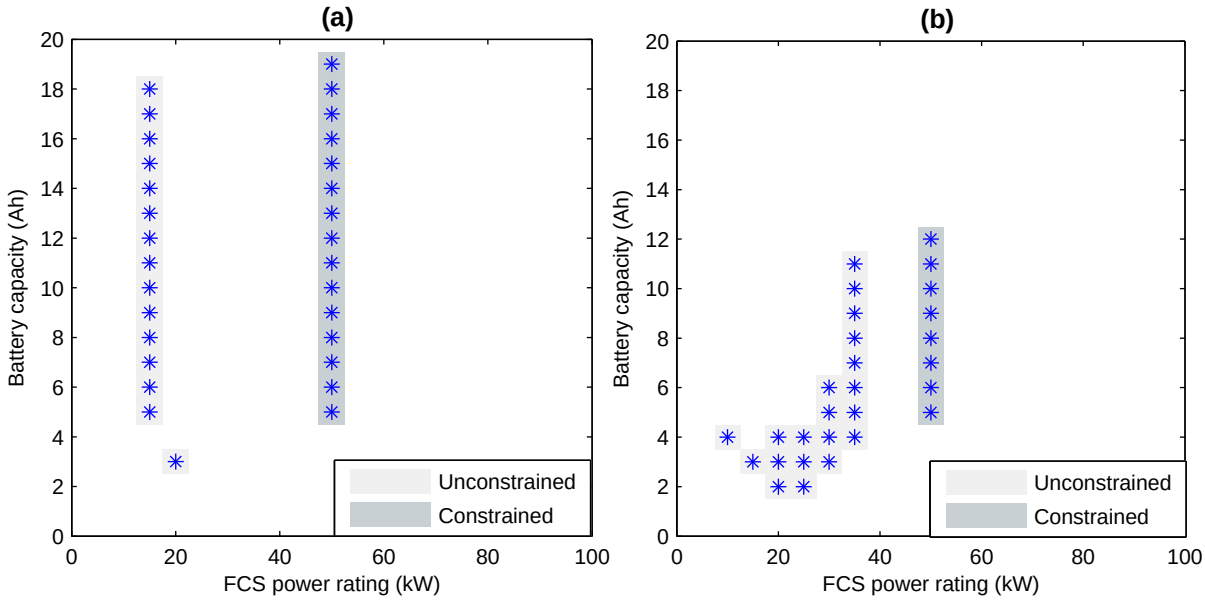

Figure 2.25: The specifications that achieve the best trade-off between cost and hydrogen consumption. (a) NEDC; (b) HWFET.

objective function as obtained from the Pareto front. In our case, two weights w_1 (corresponding to hydrogen consumption) and w_2 (corresponding to cost) are assigned to each Pareto solution. The weight represents the relative distance of the solution from the maximum (worst) value of each objective function, so that the weight w_i has a maximum value for the best solution in terms of the i-th objective. The denominator of equation (2.20) makes the weight vector (w_1, w_2) sum up to 1 for each solution. For example, for w_1=1 (w_2=0), the solution that achieves the minimum hydrogen consumption is chosen, whereas for w_1=0 (w_2=1) the solution that achieves the minimum cost is selected. For w_1 and w_2 between 0 and 1, a compromise between the two objectives is achieved.

Here three solutions $\{(w_1, w_2) = (1, 0), (0.5, 0.5), (0, 1)\}$ are reported in Table 2.8 and Table 2.9 for NEDC and HWFET, respectively, for the unconstrained and constrained cases. The results are graphically illustrated in Figure 2.26, where the values of cost and consumption are given as a percentage of the maximum for each Pareto front. As expected, for the same weight, both hydrogen consumption and cost are higher in the constrained case. For NEDC and unconstrained case, prioritizing the hydrogen consumption (w_1=1,w_2=0) can save up to 9.3% hydrogen (in comparison to w_1=0,w_2=1), whereas prioritizing the cost (w_1=0,w_2=1) can save up to 65% cost (in comparison to w_1=1,w_2=0). For equal weights given to the two objectives, the last savings figures become 6.8% for hydrogen and 51% for the cost. For the constrained case, the potential hydrogen saving is smaller of 3.1% and the potential cost saving is 46%. The same trend is observed for HWFET, where for the unconstrained case, the potential hydrogen saving is 15.7% and the potential cost saving is 67%, whereas for the constrained case, the potential hydrogen saving is 0.5% and the potential cost saving is 30%.

As a summary of sizing process, the following points can be stated:

- The optimal powertrain size depends on the driving cycle (as illustrated for NEDC and HWFET). So, there is no reference optimal size that is optimal for all systems

Table 2.8: Numerical sizing results over NEDC.

	Unconstrained			**Constrained**		
(w_1,w_2)	(1,0)	(0.5,0.5)	(0,1)	(1,0)	(0.5,0.5)	(0,1)
Hydrogen consumption (g)	70.3	72.2	77.5	87.0	87.8	89.8
Cost (€)	3776	1835	1329	5353	3588	2882
FCS power rating (kW)	15	15	20	50	50	50
Q_b (Ah) (energy (kWh))	18 (3.97)	7 (1.54)	3 (0.66)	19 (4.19)	9 (1.99)	5 (1.10)

Table 2.9: Numerical sizing results over HWFET.

	Unconstrained			**Constrained**		
(w_1,w_2)	(1,0)	(0.5,0.5)	(0,1)	(1,0)	(0.5,0.5)	(0,1)
Hydrogen consumption (g)	106.1	109.8	125.8	107.5	107.7	108.1
Cost (€)	3341	1529	1106	4118	4118	2882
FCS power rating (kW)	35	25	10	50	50	50
Q_b (Ah) (energy (kWh))	11 (2.43)	3 (0.66)	4 (0.88)	12 (2.65)	7 (1.54)	5 (1.10)

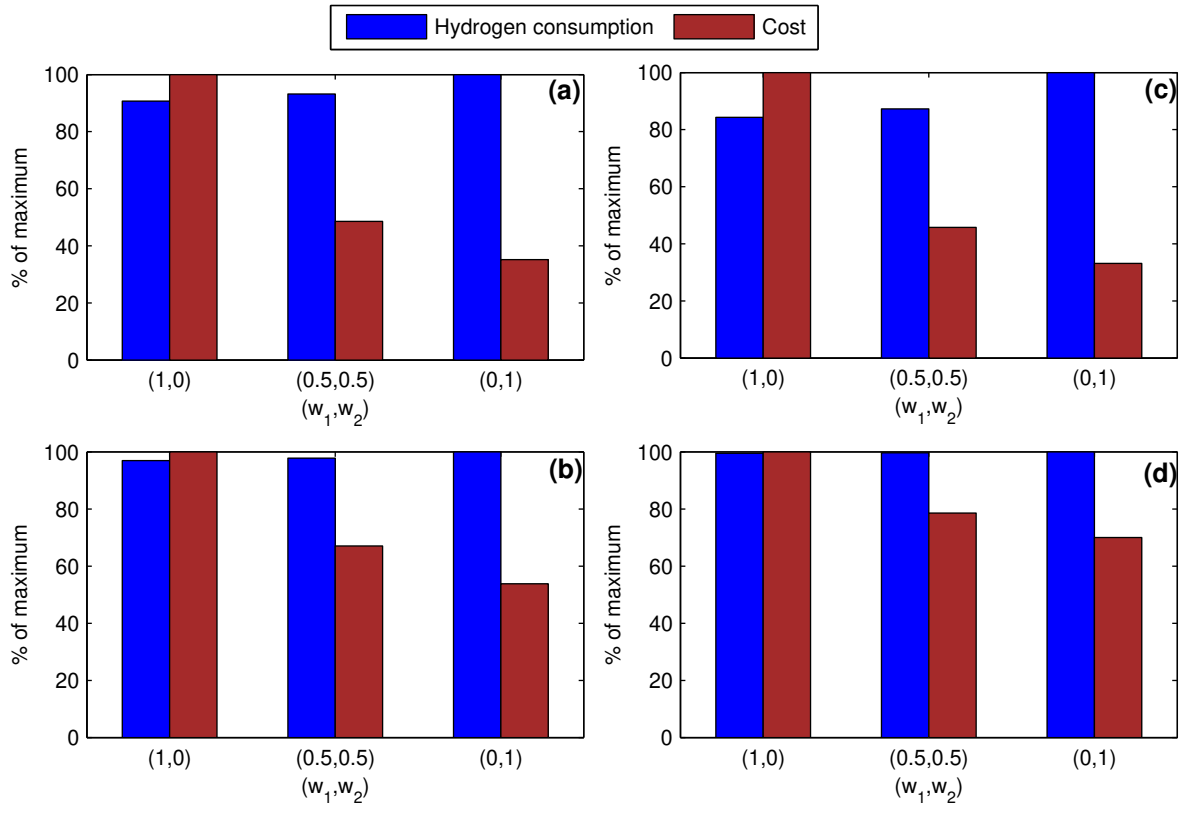

Figure 2.26: Selected solutions of the following Pareto fronts: (a) NEDC unconstrained; (b) NEDC constrained; (c) HWFET unconstrained; (d) HWFET constrained.

in all conditions. This issue mainly affects the hydrogen consumption where the minimum consumption is achieved when the average demand coincides with the peak FCS efficiency.

- Considering the hydrogen consumption as the only objective function to be minimized may lead to significantly costly powertrain, so the cost needs to be considered as an objective as well. A reasonable compromise can then be obtained that reduces the cost drastically with only a marginal increase in hydrogen consumption.

- The drivability performance (i.e., mainly gradeability and acceleration time) constraints the sizing process. Without such constraints, the optimal powertrain size may be unreasonably small.

- Direct comparison between all the possible powertrain sizes when several objective functions are considered would be a tedious task. The best option is to choose first the sizes that represent the most efficient trade-off between the objectives (i.e., Pareto front). The resulting refined possible sizes can then be used by the decision maker, who chooses among them based on predefined design preferences (i.e., how much weight is given to each objective).

- Among the designs that respect the drivability constraints, the minimum cost is achieved at the minimum FCS size of 50 kW, and the corresponding minimum battery capacity of 5 Ah. For this design, the FCS accounts for about 70% of the total cost (i.e., 2000 € out of 2882 €). This explains why it is non-economical to choose a larger FCS system (with smaller battery) because the reduction in battery size cannot compensate the increase in FCS size. If the FCS cost were significantly lower or the battery cost were significantly higher, the minimum cost would favor larger FCS and smaller battery.

- The hydrogen consumption and cost have been evaluated only at designs grid with a resolution of 5 kW for FCS power rating and 1 Ah for battery capacity. Slightly more efficient Pareto fronts can be obtained with finer grid or, alternatively, by using an evolutionary multi-objective optimization.

- Without hybridization, satisfying the acceleration time constraint requires a minimum FCS of 85 kW, which achieves a hydrogen consumption of 134.16 g and 129.81g over NEDC and HWFET, respectively. Therefore, the base hybrid vehicle saves 34% and 17% hydrogen in comparison to the only-FCS topology. These improvements are higher than those reported in Figure 2.13, which did not consider the downsizing of FCS due to hybridization.

- The following simple sizing procedure results in a good performance. The FCS power rating is chosen as a minimum that satisfies the top speed and gradeability constraints (i.e., 50 kW), and then the problem turns into a one-dimensional sizing, where the battery capacity is chosen as a compromise between acceleration, hydrogen consumption and cost, as shown in Figure 2.27. The range of 5–10 Ah is the most interesting range since it achieves most of the hydrogen saving potential and the minimum acceleration time.

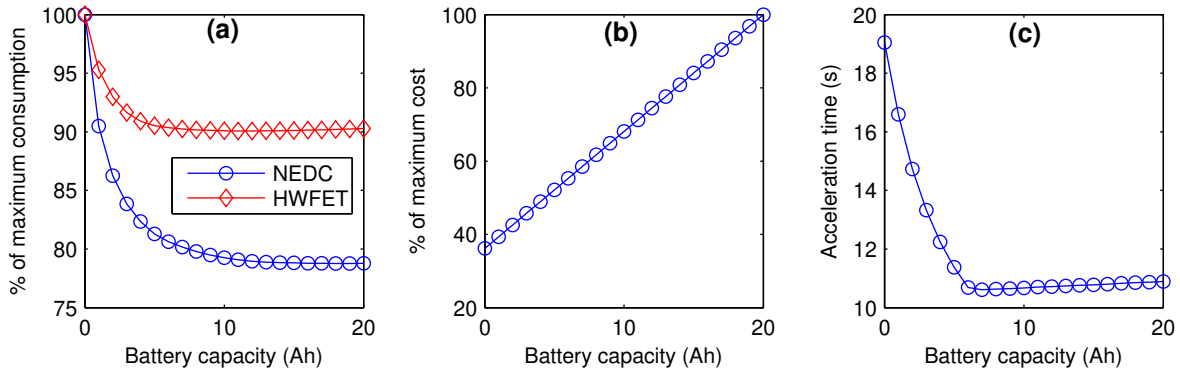

Figure 2.27: Battery sizing for an FCS of 50 kW. (a) Hydrogen consumption referenced to maximum; (b) Cost referenced to maximum; (c) Acceleration time 0–100 km/h.

2.4.3 Battery Longevity-Conscious Sizing

The aforementioned sizing procedure assumes that the battery will remain functioning for the entire vehicle lifetime using the optimal PMS (optimal in terms of hydrogen consumption). The battery service life depends on the operating conditions; therefore, an important question should be addressed: what if the battery reaches its end-of-life (EOL) before the vehicle required lifetime. There are basically two approaches to address this question [29, 77]:

- In the first approach, the same PMS (that minimizes the hydrogen consumption) is used and the battery is replaced once it reaches its EOL. This way, the cost of battery replacements needs to be considered in the cost of powertrain, whereas the hydrogen consumption evaluation stays intact. The PMS used in this approach will be denoted BLNCS (*Battery Longevity-Nonconscious Strategy*).
- The second approach is to modify the PMS so that the battery can last for the planned vehicle lifetime. In this case, the cost evaluation remains as before, whereas additional hydrogen needs to be consumed to relieve some stress from the battery if needed. The PMS used in this approach will be denoted BLCS (*Battery Longevity-Conscious Strategy*).

Investigating the effect of battery lifetime on the hydrogen consumption requires a quantitative model for battery aging.

There are two methods to quantitatively characterize the battery aging: the cycle number and the Ah-throughput (or equivalently energy-throughput). The cycle counting is suitable for lab conditions where the cycles are well defined and can be repeatedly applied to the battery; however, it cannot be used in traction applications where every charge or discharge event is different [78, 79]. Therefore, the Ah-throughput is used to express the battery aging. Over a given driving cycle of duration t_f and for charge sustaining performance (initial SOC and final SOC are the same), the Ah-throughput is defined as:

$$Ah_{dc} = \frac{1}{2}\int_0^{t_f} |I_b(t)|\,\mathrm{d}t. \tag{2.21}$$

The factor 1/2 is used so that the Ah-throughput considers only the discharged charge.

The total Ah-throughput, Ah_{tot}, that the battery can provide over its lifetime is given by:

$$Ah_{tot} = 0.9NQ_b, \tag{2.22}$$

where Q_b is the initial capacity that is the same as the rated capacity of a fresh battery; N is the cycle life of the battery measured at rated conditions for 100% DoD (depth-of-discharge). The battery EOL is reached when the capacity fades to 80% of its initial one. Assuming a linear capacity fade profile, the average battery capacity over its cycle lifetime is then $0.9Q_b$; so the factor 0.9 appears in equation (2.22).

In the simplest battery aging model, which is used here, dividing Ah_{tot} by Ah_{dc} gives the total number of driving cycles that can be driven before the battery EOL. More sophisticated models take into account other stress factors such as the charge-discharge rate, DoD and temperature while counting the Ah-throughput [78, 79, 80].

The vehicle lifetime t_{tot} is taken as 5000 hours, which is the DOE target for fuel cell vehicular systems [10]. This corresponds to about 167000 km total driving distance over NEDC. In order for the battery to survive the vehicle lifetime, the Ah_{dc} must be smaller than Ah_{target} given by:

$$Ah_{target} = \frac{t_f}{t_{tot}} Ah_{tot}. \tag{2.23}$$

If the Ah_{dc} achieved by the PMS is lower than the target, then the battery can survive the vehicle lifetime. Otherwise, the battery needs to be replaced in the first approach $floor(Ah_{dc}/\ Ah_{target})$ times, or the PMS needs to be modified (in the second approach) so that Ah_{dc} is reduced to Ah_{target}, which explains the use of the subscript "target."

Reducing the Ah_{dc} in BLCS, when necessary, can be attained by augmenting the hydrogen consumption by a penalty function of the battery current as follows:

$$J = \int_0^{t_f} \{\dot{m}_h(t) + \alpha\,|I_b(t)|\}\,\mathrm{d}t. \tag{2.24}$$

The penalty factor α has the unit of g/(A.s) and it determines the weight given to the Ah_{dc} in minimizing J. Increasing α, causes the Ah_{dc} to decrease and hydrogen consumption to increase, and vice versa. For zero α, the conventional PMS optimization problem, which considers only hydrogen consumption, is obtained. For infinite α, the battery current would be always zero resulting in the pure fuel cell drive. By tuning α, the Ah_{dc} can be reduced to Ah_{target}.

Two factors would play a role in finding the right value of α; these are the battery capacity and battery cycle life. From equations (2.22) and (2.23), with increasing Q_b and/or N, the Ah_{target} increases; hence, lower value of α is required which results in less sacrifice in hydrogen consumption (i.e., smaller increase in hydrogen consumption in comparison to the conventional optimization problem).

Figure 2.28 illustrates the effect of battery cycle life on the Pareto front for drivability-constrained sizing. From now on, only the plant designs that satisfy the drivability constraints are considered. The term "ideal" is used to refer to the practically ageless

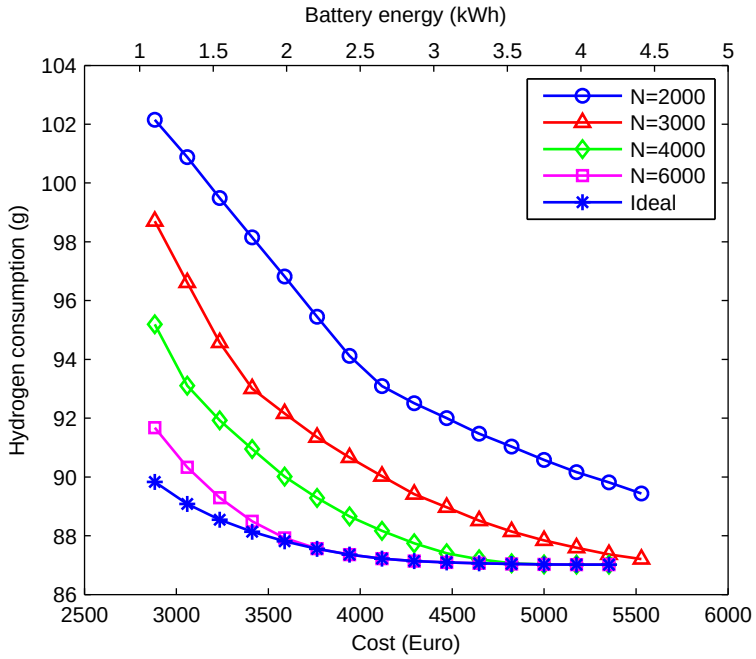

Figure 2.28: Effect of battery cycle life on the Pareto front between cost and hydrogen consumption with BLCS over NEDC.

battery where the battery has a very long cycle life so that its lifetime does not affect the sizing process. For variable battery cycle life, the Pareto front is achieved always for an FCS size of 50 kW (the same as the ideal case), so that the variation in plant cost in the Pareto front comes from the variation in battery capacity. As shown in Figure 2.28, the amount of hydrogen, which needs to be compromised for extending the battery service life to match the vehicle lifetime, increases with decreasing battery capacity and decreasing battery cycle life.

Figure 2.29 shows the current of a 5-Ah battery (1.1 kWh) for the ideal case and for a cycle life of 2000 cycles with BLCS. The ideal battery achieves an Ah_{dc} of 2.9 Ah. This value needs to be reduced to an Ah_{target} of 0.6 Ah for N=2000 in order for the battery to survive the vehicle life. The result is a significant reduction in battery contribution increasing the hydrogen consumption by about 14% (i.e., from 89.2 g to 102.2 g).

In order to compare the two PMS design approaches, BLCS and BLNCS, it is more convenient to use a single objective function to minimize rather than two by converting the hydrogen consumption into cost and adding it to the powertrain cost. The cycle-normalized cost is used here defined as:

$$\begin{aligned} Cycle-normalize\ cost \quad &= \quad (plant\ cost) \times \frac{t_f}{t_{tot}} + \\ &\quad (hydrogen\ consumption) \times (hydrogen\ cost). \end{aligned} \tag{2.25}$$

Figure 2.30 compares the two approaches to consider the battery lifetime in terms of the NEDC-normalized cost for two hydrogen cost scenarios, 10 €/kg and 5 €/kg[7]. For the

[7]In [81], a stochastic analysis is performed to determine the hydrogen cost in the early market introduction of fuel cell vehicles to make them competitive with the conventional ICE-based ones. It was concluded that the hydrogen would cost about US$4-12 per kilogram, with US$7 as the most likely case.

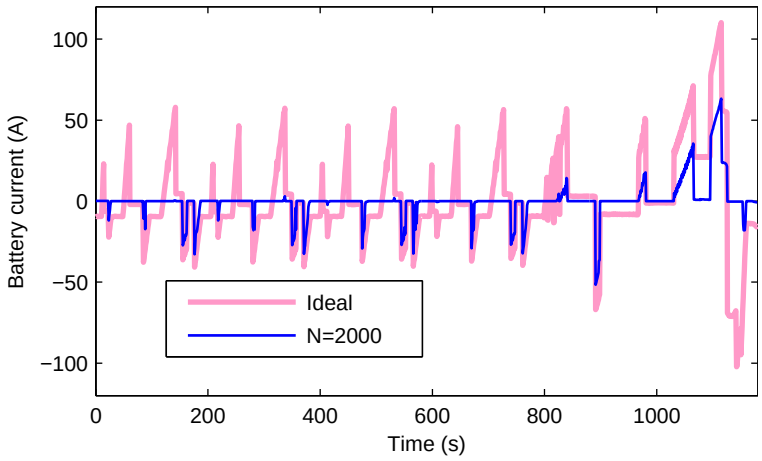

Figure 2.29: Battery current for an ideal battery and a battery with a cycle life of 2000 cycles for a capacity of 5 Ah with BLCS over NEDC.

two approaches decreasing the battery cycle life leads to an increase in NEDC-normalized cost. This cost increase for BLNCS comes from either using small batteries requiring more often replacement or oversizing the battery requiring less often replacement, which one is more economical. Whereas, this cost increase for BLCS comes from either using small batteries requiring more hydrogen consumption or oversizing the battery requiring less hydrogen consumption, which one is more economical. It is clear that the BLCS option is far much economical in compensating short battery lifetimes. The BLNCS option results in a cost increase of 21% and 36% (for hydrogen cost of 10 and 5 €/kg, respectively) for N=2000 in comparison to the ideal battery, whereas the corresponding increase for BLCS is about 10%. In other terms, for batteries with short lifetime, it is more economical to have a PMS that uses the battery less aggressively than a PMS that exhausts the battery so that it needs to be replaced or extensively oversized.

Table 2.10 gives the numerical details of the sizing optimization for the BLCS option. For a hydrogen cost of 10 €/kg, the contribution of hydrogen cost to the NEDC-normalized cost is significant, so that the optimization tends to choose larger battery for shorter battery cycle life in order not to increase hydrogen consumption too much. In comparison, for a hydrogen cost of 5 €/kg, the optimization chooses the smallest possible battery, because the contribution of hydrogen consumption is smaller and decreasing the hydrogen consumption by choosing larger battery cannot simply compensate the increase in plant cost.

Table 2.10: Sizing optimization results over NEDC.

Battery cycle life (cycles)	**10 €/kg hydrogen**			**5 €/kg hydrogen**		
	FCS (kW)	Battery (kWh)	NEDC-normalized cost in €(hydrogen, plant)	FCS (kW)	Battery (kWh)	NEDC-normalized cost in €(hydrogen, plant)
2000	50	2.43	1.200(0.941,0.258)	50	1.10	0.700(0.511,0.189)
3000	50	1.76	1.154(0.930,0.224)	50	1.10	0.683(0.494,0.189)
4000	50	1.54	1.131(0.919,0.212)	50	1.10	0.665(0.476,0.189)
6000	50	1.32	1.104(0.903,0.201)	50	1.10	0.647(0.458,0.189)
ideal	50	1.10	1.087(0.898,0.189)	50	1.10	0.638(0.449,0.189)

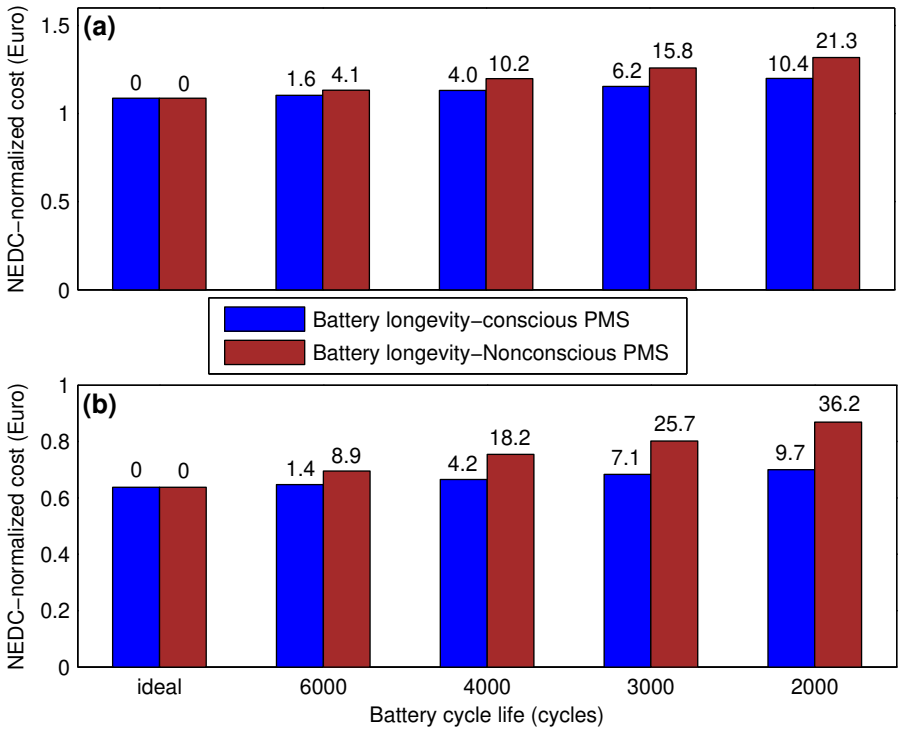

Figure 2.30: Comparison between BLCS and BLNCS options for the PMS design in terms of the NEDC-normalized cost. (a) Hydrogen cost of 10 Euro/kg; (b) Hydrogen cost of 5 Euro/kg. The numbers above the bars represent the percentage cost increase in comparison to the ideal battery.

2.5 Real-Time Strategy

The off-line optimal strategy is highly sensitive to the driving cycle, so that the optimal strategy over one driving cycle may result in a poor performance over other cycles. Figure 2.31 illustrates this idea. The figure shows two SOC trajectories of the UDDS. The first trajectory results from the application of the constant co-state optimized over HWFET for a charge sustaining performance. The application of HWFET optimum leads over UDDS to a final SOC of 0.75 (i.e., the upper SOC limit). The second trajectory represents the strategy optimized over UDDS itself, with the same final SOC of 0.75. First, the two SOC trajectories are completely different. Second, the HWFET optimum when applied to UDDS results in a hydrogen consumption of 121.4 g corresponding to 17% more hydrogen than the UDDS optimum of 103.4 g. In conclusion, the optimal strategy over one driving cycle may behave very poorly over other driving cycles.

The last example illustrates the fact that the off-line optimal strategy, represented by the optimal co-state in PMP, is very sensitive to driving cycle. Therefore, if PMP is to be used in real-time, the co-state needs to be updated in real-time.

The real-time controller used here is given by:

$$\lambda(t) = \lambda_0 + K_p\left(x_{ref} - x(t)\right) + K_i \int_0^t \left(x_{ref} - x(\tau)\right) \mathrm{d}\tau, \tag{2.26}$$

where the co-state is adapted through a proportional-integral (PI) controller of the battery SOC, with λ_0 is the initial co-state, K_p is the proportional gain and K_i is the integral

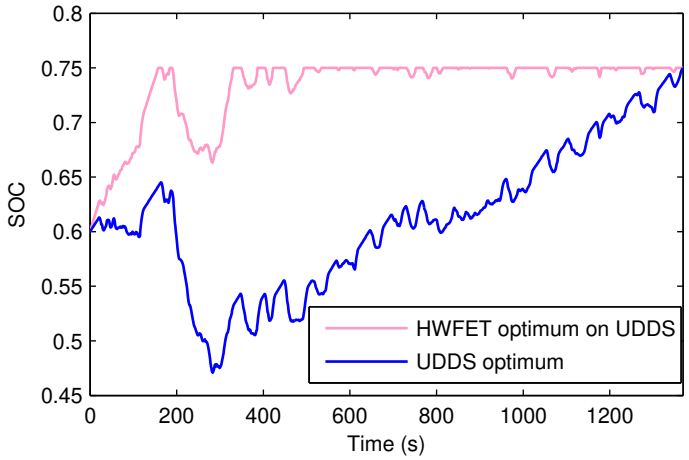

Figure 2.31: Illustration of the high sensitivity of the off-line optimal strategy to the driving cycle.

gain. It controls the battery SOC around a constant reference, x_{ref}, of 0.6 and outputs the co-state which is then used in real-time when minimizing the Hamiltonian defined in equation (2.14). The advantages of this controller have been experimentally evaluated by the author in [72].

The structure of the real-time PMS is depicted in Figure 2.32. The PMS accepts the power demand and the current SOC as inputs and outputs the power contribution of FCS and battery. In comparison to the off-line optimal PMS, the real-time PMS uses only the current state to decide the current co-state and, therefore, the current control action that minimizes the Hamiltonian.

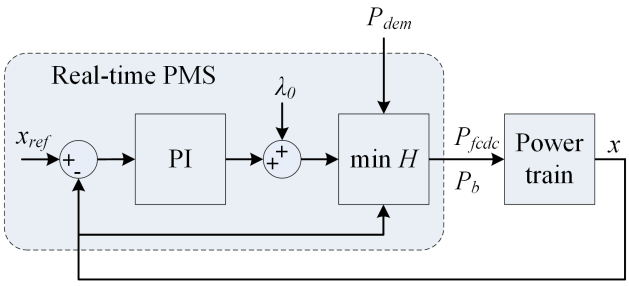

Figure 2.32: Schematic of the real-time power management strategy.

In order to optimize the controller parameters, λ_0, K_p and K_i, the optimization objectives have to be first established. The objectives of optimization are:

- Hydrogen consumption as close as possible to the off-line optimum;
- The co-state adaptation needs to be sufficiently fast (i.e., SOC control sufficiently strong). Very weak SOC control may lead to the situation encountered in Figure 2.31, where the SOC reaches its upper limit and remains there (i.e., no regenerative braking more possible) or reaches its lower limit and remains there (i.e., no further assistance from the battery is possible);
- The resulting strategy needs to be robust and performs well over various driving cycles of different nature (urban and highway cycles).

Two performance indices of the real-time controller are defined: J_1 evaluates the performance in terms of hydrogen consumption and J_2 evaluates the performance in terms of charge sustenance. The two performance indices are defined as follows:

$$\begin{aligned} J_1 &= \frac{1}{N_{dc}} \sum_i \frac{HC^i - HC^i_{opt}}{HC^i_{opt}} \times 100\,(\%), \\ J_2 &= \max_i \left| x^i_f - x_{f,ref} \right|. \end{aligned} \tag{2.27}$$

Each set of controller parameters leads for a driving cycle i to a specific final SOC of x^i_f and a specific hydrogen consumption of HC^i. HC^i_{opt} represents the off-line optimal hydrogen consumption which depends on x^i_f. So, the ratio $\left(HC^i - HC^i_{opt}\right)/HC^i_{opt}$ represents the percentage deviation from the off-line optimal hydrogen consumption. The deviations of all driving cycles are averaged to form J_1, where N_{dc} is the number of driving cycles engaged in the optimization. J_2 represents the maximum deviation from the charge sustenance.

Optimizing the real-time controller over many driving cycles at once enriches the training set of the controller and, therefore, improves its robustness when applied to real-world applications. Considering the percentage deviation of real-time hydrogen consumption from the off-line optimum as an objective to minimize, rather than the absolute hydrogen consumption itself, enables grouping many driving cycles in the optimization. The absolute consumption may vary significantly between driving cycles depending on its duration and nature. Therefore, if considering the absolute consumption, the optimization will be biased toward the driving cycles with higher consumption and other low consumption cycles will be of minor importance. The deviation from the charge sustenance, J_2 , is used here as an index of the controller strength.

Minimizing the two objectives leads to a multi-objective optimization problem (see Appendix B) with the controller parameters as the optimization variables. The ranges of the optimization variables were as follows: λ_0 is limited between 0 and 100, K_p between 0 and 1000, and K_i between 0 and 1. The real-time strategy is optimized over three driving cycles NEDC, UDDS and HWFET (i.e., N_{dc} =3) and its robustness is evaluated over J. 10-15.

The resulting Pareto front is shown in Figure 2.33; it represents the most efficient trade-off between the two objective functions. Each Pareto solution corresponds to a set of strategy parameters. Figure 2.34 and Table 2.11 illustrate the performance of three Pareto solutions with three values of J_2 of 0.001 (almost perfect charge sustenance), 0.05 and 0.1. With increasing J_2, the SOC control gets weaker and the SOC becomes freer to move around the reference resulting in closer hydrogen consumption to the off-line optimum. The driving cycle J. 10-15 was not included in the optimization of the real-time PMS; however, the performance of the real-time strategy over it in terms of SOC sustenance and hydrogen consumption resembles that of the cycles engaged in the optimization which indicates the robustness of the controller.

All the Pareto solutions are mathematically equally optimal. Choosing one of them as a design of the real-time PMS requires weighing the relative importance of the two objective functions. It can be argued that the strength of SOC control is favorable as long as it does not affect the hydrogen consumption so much. For example, for J_2 of 0.05 in

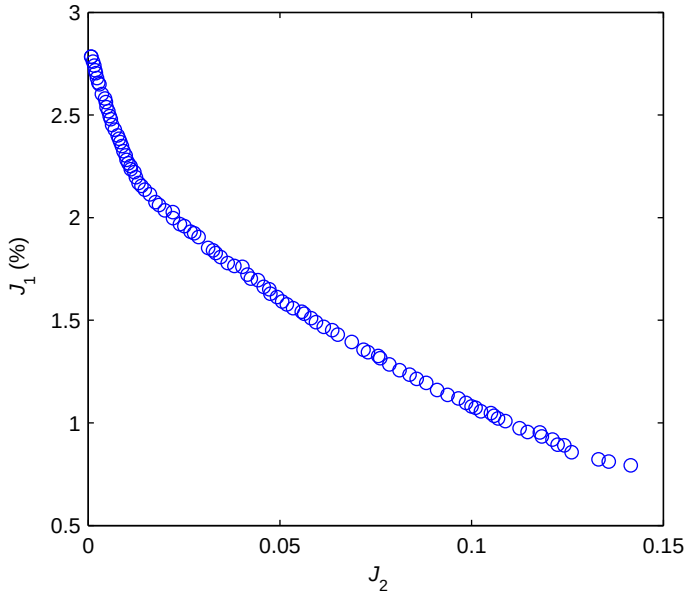

Figure 2.33: Pareto front of the real-time PMS.

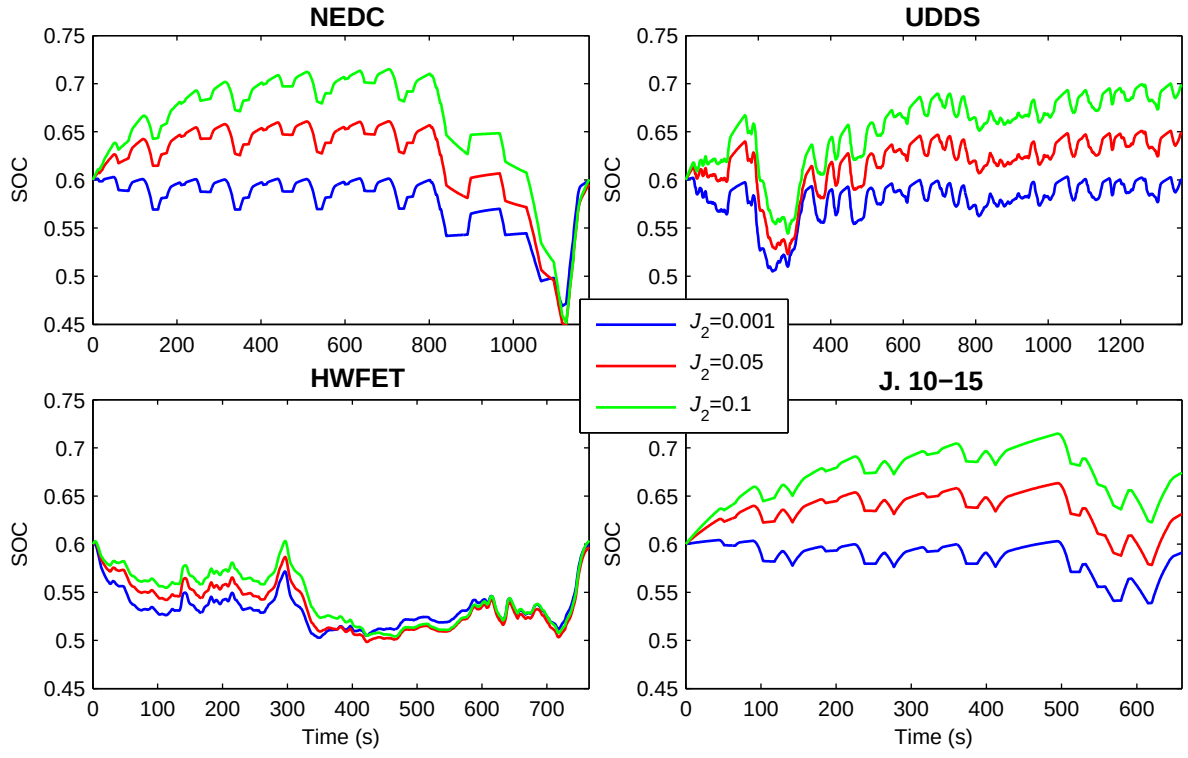

Figure 2.34: State trajectories of three Pareto solutions.

Table 2.11: Performance of the real-time strategy in terms of final SOC and hydrogen consumption (referenced to off-line optimum) for three Pareto solutions.

Driving cycle	J_2 =0.001, J_1=2.8%		J_2 =0.05, J_1=1.6%		J_2 =0.1, J_1=1.1%	
	Final SOC	Consumption (%)	Final SOC	Consumption (%)	Final SOC	Consumption (%)
NEDC	0.599	5.2	0.596	3.2	0.601	2.0
UDDS	0.601	2.1	0.649	1.1	0.699	0.9
HWFET	0.599	1.1	0.597	0.6	0.604	0.4
J. 10-15	0.591	1.4	0.631	0.6	0.674	0.5

comparison to perfect charge sustenance, the hydrogen consumption can be decreased by 2% over NEDC and about 1% over the other driving cycles. However, increasing J_2 to 0.1 significantly weakens the SOC control with a marginal gain in hydrogen consumption. So, J_2 of 0.05 may be considered as a good compromise between the two objective functions.

2.6 Experimental Study

In this section, the power management optimization of an experimental fuel cell/battery hybrid system is carried out. The off-line optimal strategy is obtained using PMP. As described in Section 2.5, the real-time strategy is optimized over NEDC, UDDS and HWFET and its robustness is additionally evaluated over J. 10-15.

The layout and specifications of the test bench are given in Appendix C. The test bench is supposed to simulate the vehicle on a small scale. The hybrid power source of the vehicle has a maximum fuel cell power of 50 kW and a 1.5 kWh battery. The net power of the test bench FCS is limited to 700 W. The ratio of vehicle FCS power to the test bench FCS power of 70 ($\approx$ 50 kW/0.7 kW) is used as a scaling factor between the vehicle and test bench, so that the vehicle power demand calculated by the vehicle model in Section 2.1 is divided by this scaling factor when it is applied to the test bench.

Using the same scaling factor to downscale the vehicle battery size, the battery of the test bench should have an energy of 21 Wh (=1500 Wh/70). Assuming a 37 V nominal battery voltage in the test bench, a 0.6 Ah battery capacity is required in the test bench. Actually, the battery used has a capacity of 30 Ah, which is quite large in comparison to the required capacity. So, only 0.6 Ah from the entire capacity is considered around 60% SOC, and the reported experimental SOC corresponds to the required capacity, not to the actual one.

The multi-objective optimization was conducted withλ_0, K_p and K_i as optimization variables, and J_1 and J_2 defined in equation (2.27) as the objectives to be minimized. The ranges of the optimization variables were as follows: λ_0 is limited between 1 and 2, K_p between 0 and 10, K_i between 0 and 0.01. The solution that achieves the minimum J_2 (i.e., of about 0.002 which is practically a charge sustaining performance) is considered, since it corresponded to J_1 of only 0.75%. The corresponding optimal parameters are: λ_0=1.23, K_p=2.10 and K_i=0.

The experimental evaluation of the real-time strategy is shown in Figures 2.35 and 2.36 for NEDC and J. 10-15, respectively. NEDC is included in the strategy optimization, whereas J. 10-15 is not so that it is used to test the robustness of the strategy over other driving cycles not included in its optimization. The battery contributes strongly to the demand during acceleration and regenerative braking phases, whereas the FCS delivers the cruising demand. The experiment reproduces the simulation results very well as illustrated by comparing the simulation and experiment in terms of state trajectories.

The battery used in this study is of high efficiency due to the oversized capacity, so that it is practically lossless. Consulting Section 2.3.5, for a lossless battery the optimal FCS power that minimizes the Hamiltonian is independent of the power demand, and it is solely dependent on the co-state. Therefore, the variation of the FCS power in Figures 2.35 and 2.36 is actually a result of the co-state variation.

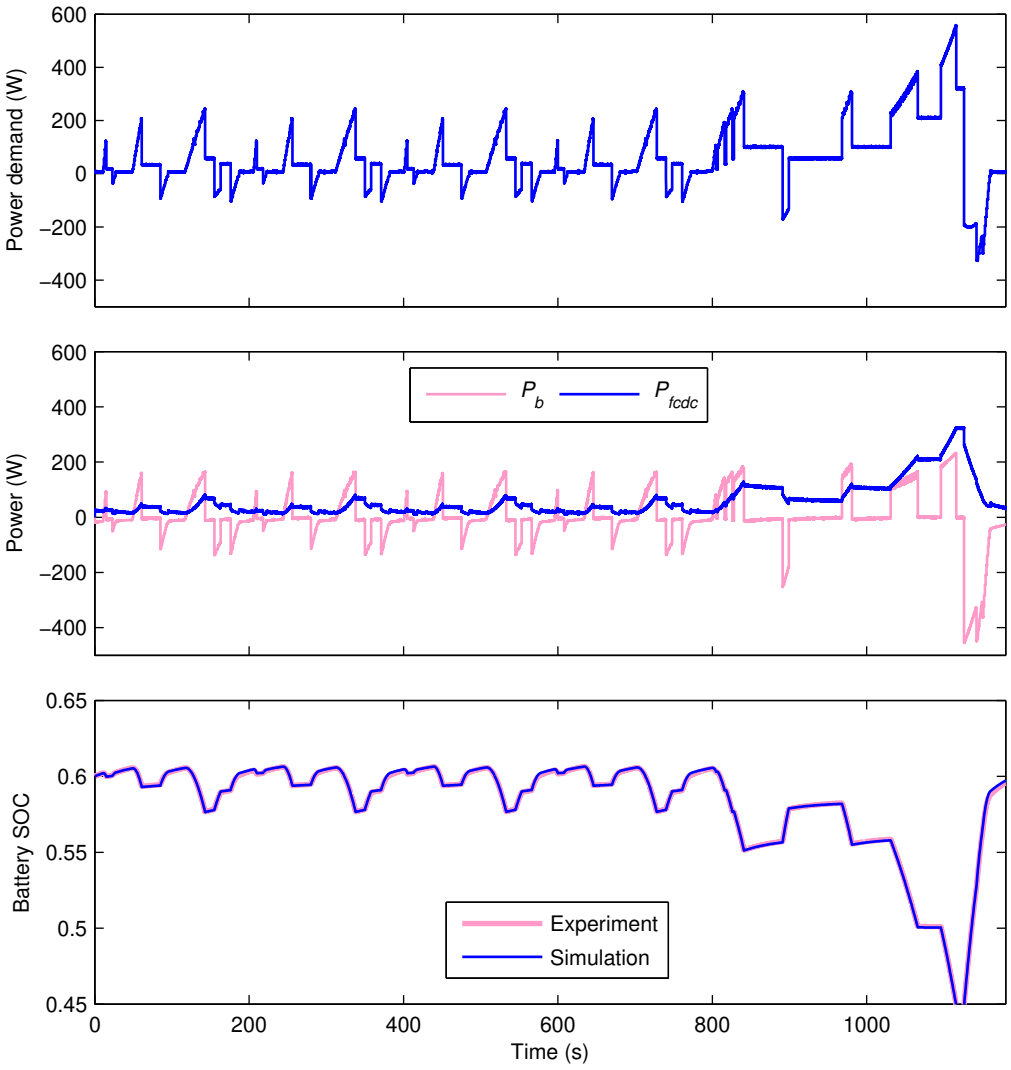

Figure 2.35: Experimental evaluation of the real-time power management strategy over NEDC.

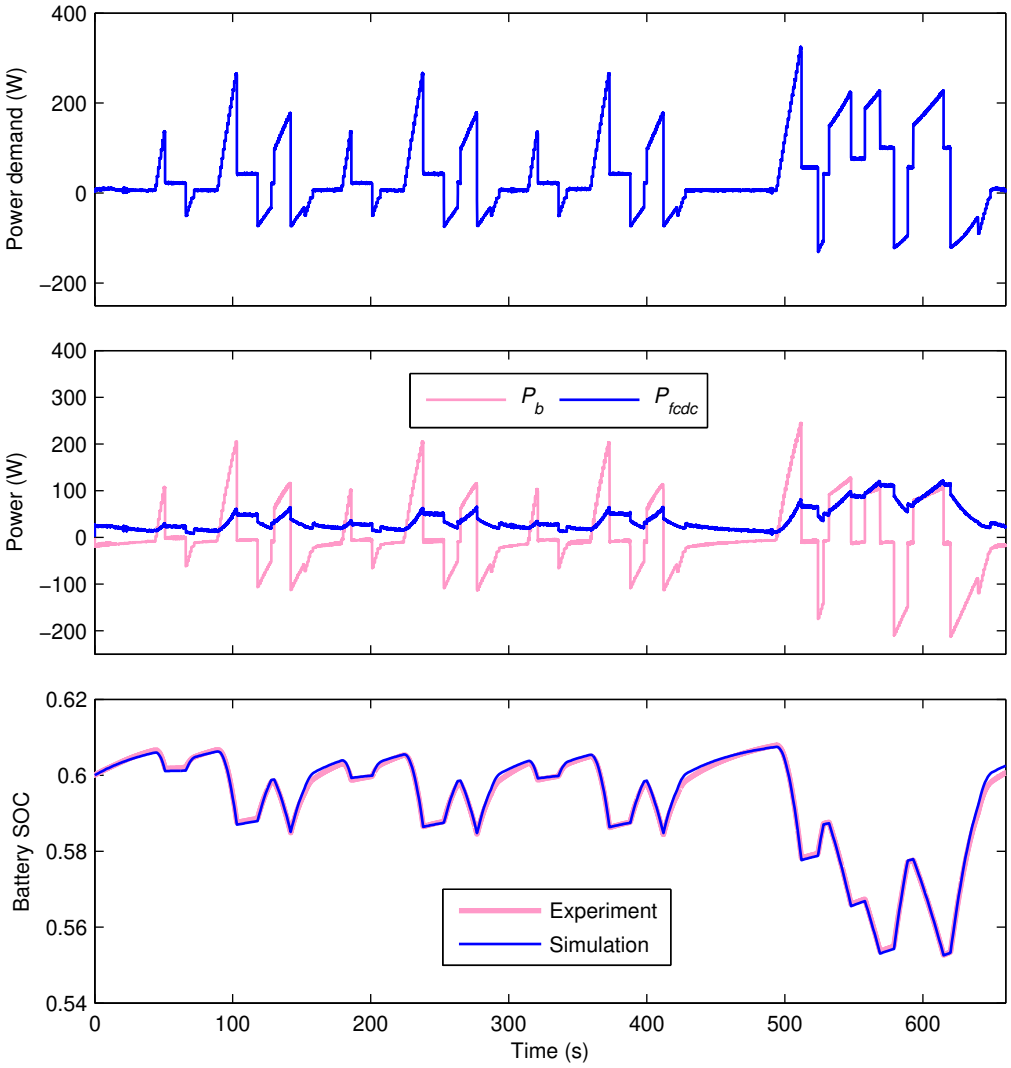

Figure 2.36: Experimental evaluation of the real-time power management strategy over J. 10-15.

Figure 2.37 shows the current and voltage waveforms of the FCS and battery over NEDC. Due to the high efficiency of the battery used, its voltage does not change significantly.

Figure 2.38 compares the off-line optimum and the real-time PMS in terms of hydrogen consumption. The off-line optimal hydrogen consumption is measured for different final SOC by applying the corresponding off-line optimal co-state trajectories. Three runs of the experiment are conducted for the real-time strategy, the average consumption is then considered. As expected from simulation and optimization, the hydrogen consumption of the real-time strategy is barely distinguishable from that of the off-line optimum.

The advantage of hybridization with respect to hydrogen consumption was evaluated by measuring the hydrogen consumption when only the FCS is used to drive the load and the battery is disconnected. The measured consumptions over the evaluation driving cycles are listed in the second column of Table 2.12, whereas the consumption of the optimized real-time strategy is listed in the third column. The figures of hydrogen saving are closely correlated with those given in Figure 2.13.

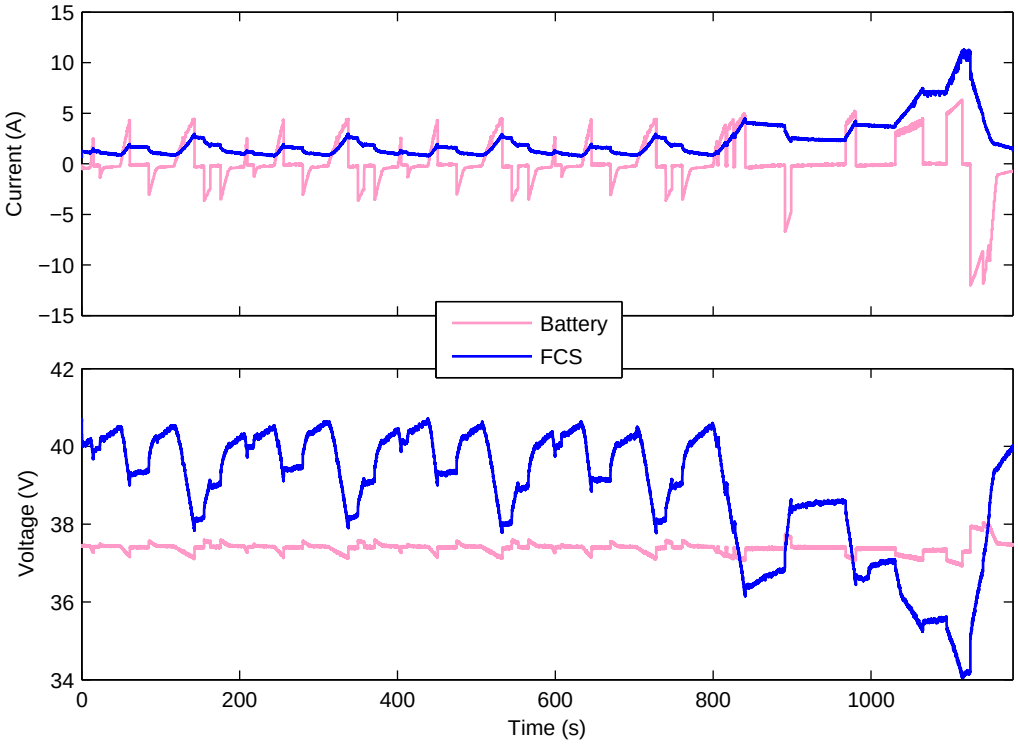

Figure 2.37: Current and voltage measurements over NEDC.

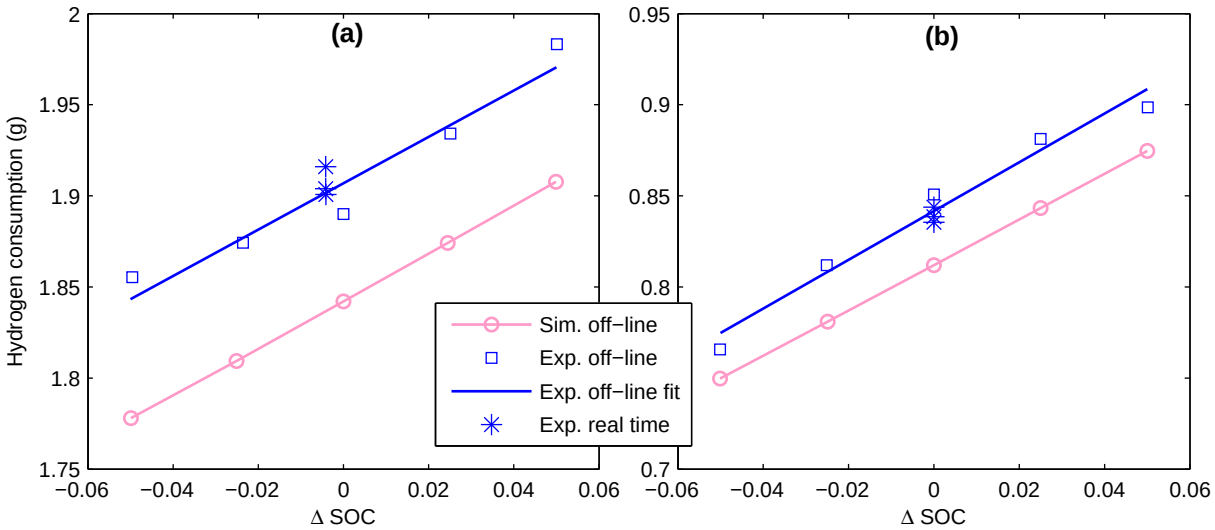

Figure 2.38: Experimental evaluation of the off-line optimal and real-time PMS in terms of hydrogen consumption as a function of the difference (final SOC – initial SOC). (a) NEDC; (b) J. 10-15.

Table 2.12: Experimental comparison between only fuel cell drive and hybrid drive in terms of hydrogen consumption.

Driving cycle	Only FCS (g)	Hybrid (g)	Improvement (%)
NEDC	2.31	1.91	17
UDDS	2.61	2.01	23
HWFET	2.43	2.15	11
J. 10-15	1.04	0.84	19

2.7 Conclusions

In this chapter, fuel cell/battery hybrid systems for passenger vehicles were investigated in terms of PMS design and optimization, and in terms of powertrain sizing.

The PMS optimization was first performed assuming a complete knowledge of the driving cycle, resulting in an off-line optimal strategy that globally minimizes the hydrogen consumption. DP and PMP have been compared as two possible off-line optimization techniques. The comparison revealed that both algorithms achieve the global optimal PMS, whereas PMP has the advantage of negligible required computation resources (i.e., time and memory).

A real-time capable PMS was designed and optimized while using the off-line optimal PMS as a benchmark. The optimization of the real-time PMS was formulated as multi-objective optimization problem, taking into account hydrogen consumption and charge sustenance as two optimization objectives. Special emphasize is put on the inclusion of multiple driving cycles, of different nature, in the optimization to increase the robustness of the strategy.

The sizing of the power sources, i.e., FCS and battery, took into account hydrogen consumption and plant cost as two objectives. The sizing process was approached by two nested loops. The outer loop represents an exhaustive search algorithm that iterates over all the possible designs (FCS size and battery size), and for each design the objective functions are evaluated within the inner loop that represents the optimization of the PMS by PMP. The most efficient designs (i.e., Pareto front), which represent the most efficient trade-off between the objectives, were then extracted and analyzed.

The effect of battery lifetime on the sizing process was investigated by using an Ampere-hour throughput model to quantify the battery aging. To include the effect of battery lifetime in the sizing process, two approaches were compared: the first approach (BLNCS) assumes an optimal PMS (in terms of hydrogen consumption) and assumes that the battery is replaced once it reaches its EOL. The second approach (BLCS) modifies the PMS so that the battery can last for the entire planned vehicle lifetime. It was found that the second approach is far more economical especially for batteries with short lifetime.

The off-line and real-time PMS optimization techniques were validated on a small-scale experimental fuel cell/battery hybrid system. The experimental measurements replicated the simulation results very well, thanks to the good models of the test bench components. The optimized real-time PMS was found to have a hydrogen consumption indistinguishable from the off-line optimum.

Chapter 3

Fuel Cell/Supercapacitor Hybrid

In this chapter, a fuel cell/supercapacitor vehicular hybrid system is investigated in terms of power management optimization and sizing. The vehicle model introduced in Section 2.1 is adopted in Section 3.1 for the calculation of the power demand of the hybrid power source for standard driving cycles. In Section 3.2, the two off-line optimization techniques, Dynamic Programming (DP) ans Pontryagin's Minimum Principle (PMP), are applied and compared. The sizing of power sources (i.e., fuel cells and supercapacitor) is addressed in Section 3.3, taking into account hydrogen consumption and plant cost. The design and optimization of a real-time capable power management strategy is introduced in Section 3.4. Experimental results obtained from a small test bench are presented in Section 3.5. The experimental study discusses, in addition to power management strategy design and optimization, other issues like the effect of FCS power dynamics limitation on hydrogen consumption, and the inclusion of such limitation in the off-line optimization techniques. Moreover, experimental results of an alternative power sources topology (direct coupling of FCS and supercapacitor without converters) are presented.

3.1 Vehicle Model

The topology of the fuel cell/supercapacitor vehicle is depicted in Figure 3.1. The FCS is coupled to the DC bus via a unidirectional DC/DC converter, whereas the supercapacitor is interfaced with the DC bus by a bidirectional converter. One converter is used to regulate the DC bus voltage, whereas the second one is used to control the power sharing between the two power sources. The parameters of the vehicle model are the same as those used for the fuel cell/battery vehicle listed in Table 2.1.

The power demand, P_{dem}, is the sum of the supercapacitor DC/DC converter power, P_{scdc}, and the power of FCS DC/DC converter, P_{fcdc}; i.e.,

$$P_{dem} = P_{fcdc} + P_{scdc}. \tag{3.1}$$

The FCS is modeled by its efficiency shown in Figure 2.7. Its converter is modeled by its constant efficiency of 95%. A 50 kW FCS is assumed in this study.

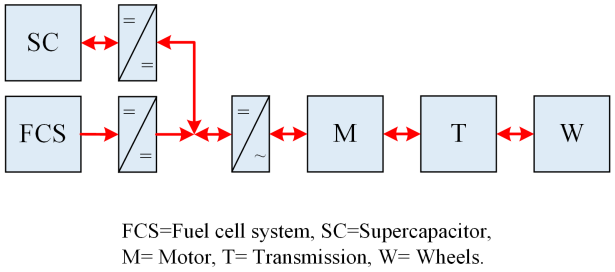

Figure 3.1: Schematic of fuel cell/supercapacitor hybrid powertrain.

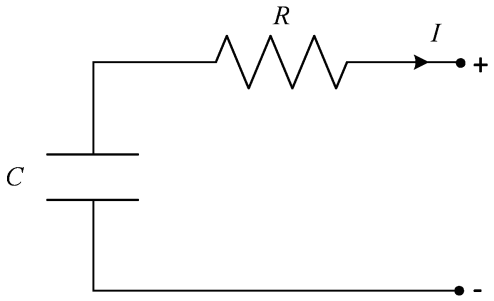

Figure 3.2: Equivalent circuit of the supercapacitor model.

The supercapacitor is modeled by the internal-resistance model of Figure 3.2. This model is the same as that used for the battery in Figure 2.8(a), however, with a capacitor instead of a voltage source because the open circuit voltage of the supercapacitor changes linearly with its SOC. The supercapacitor converter is modeled by its constant efficiency of 95%. The building block of the supercapacitor bank is a Boostcap BCAP3000P270 from Maxwell Technologies, which is characterized by a capacitance of 3000 F, a rated voltage of 2.7 V and an internal resistance of 0.29 mΩ [81].

The supercapacitor open circuit voltage, V_{sc}, varies linearly with its SOC; i.e.,

$$\text{SOC} = \frac{V_{sc}}{V_{sc,\max}}, \tag{3.2}$$

where$V_{sc,\max}$ is the maximum open circuit voltage, which equals the rated voltage. To be consistent with the literature, the supercapacitor state-of-energy (SOE), rather than its SOC, is used as the state of the system (i.e., x=SOE), which is calculated according to equation (3.3) and its dynamics is governed by equation (3.4):

$$\begin{aligned} x_{sc}(t) &= \frac{E(t)}{E_{sc}} = \left(\frac{V_{sc}(t)}{V_{sc,max}}\right)^2, \\ &= x_{sc}(0) - \frac{1}{E_{sc}}\int_0^t I_{sc}(\tau)V_{sc}(\tau)\mathrm{d}\tau, \end{aligned} \tag{3.3}$$

$$\dot{x}_{sc}(t) = \frac{-I_{sc}V_{sc}}{E_{sc}} = \frac{-V_{sc}}{2R_{sc}E_{sc}}\left(V_{sc} - \sqrt{V_{sc}^2 - 4R_{sc}P_{sc}(t)}\right), \tag{3.4}$$

where $E(t)$ is the remaining energy content, E_{sc} is the energy capacity, I_{sc} is the supercapacitor current, R_{sc} is its internal resistance and P_{sc} is its power.

The supercapacitor SOE is constrained between 25% and 95% at any time. The lower SOE limit corresponds to half of the maximum voltage, and the upper SOE limit is set below 1 as a safety margin. The SOE constraints restrict the usable energy to 70% of its maximum energy capacity.

110 cells are assumed to form the supercapacitor bank. This choice is based on observations of typical supercapacitor design in literature, where the number of cells is typically chosen so that the average voltage matches the DC bus voltage [51, 82]. The DC bus voltage is chosen as 220 V, the same used for the fuel cell/battery vehicle. For 110 cells, the supercapacitor voltage varies between about 150 V and 290 V, with 220 V as an average value. The total energy of the supercapacitor bank is about 330 Wh, whereas its usable energy is about 230 Wh.

3.2 Off-Line Optimization

For finding the off-line optimal PMS, the two algorithms, DP (see Section 2.2.1) and PMP (see Section 2.2.2) have been applied. A supercapacitor initial and final SOE of 0.8 is assumed for the off-line optimization. The supercapacitor current is limited to ±300 A.

The resulting state trajectories are shown in Figure 3.3 over NEDC. The two algorithms achieve almost identical state trajectories, with the same hydrogen consumption of 91.97 g. It is interesting to notice that this consumption is higher than the consumption of FCS/battery hybrid (88.63 g from Table 2.5), even though the supercapacitor attains higher efficiency than the battery (round-trip efficiency of the battery was 93.6%, whereas it is 98.8% for supercapacitor). This is attributed to, first, the losses of the supercapacitor DC/DC converter (with 100% efficiency of supercapacitor converter, the consumption is 89.38 g) and, second, the state constraints are active more often in the case of supercapacitor due to its lower energy content.

3.3 Sizing

In this section the effect of FCS and supercapacitor sizes on the vehicle performance will be discussed. The sizing procedure used here is the same used to size the fuel cell/battery hybrid vehicle in Section 2.4. For an objective comparison between battery and supercapacitor, the supercapacitor converter efficiency is set here to 100% and its mass is set to zero, so that the ideal scenario is considered.

The variables of the sizing problem are the size of FCS and the size of supercapacitor bank. The size of FCS is defined by its power rating. The supercapacitor size is varied by varying the number of cells connected in series. The mass and cost scaling factors of the power sources are given in Table 3.1. The cost of supercapacitor cell of 30 € is calculated assuming a cost of 0.01 € per Farad of capacitance [29].

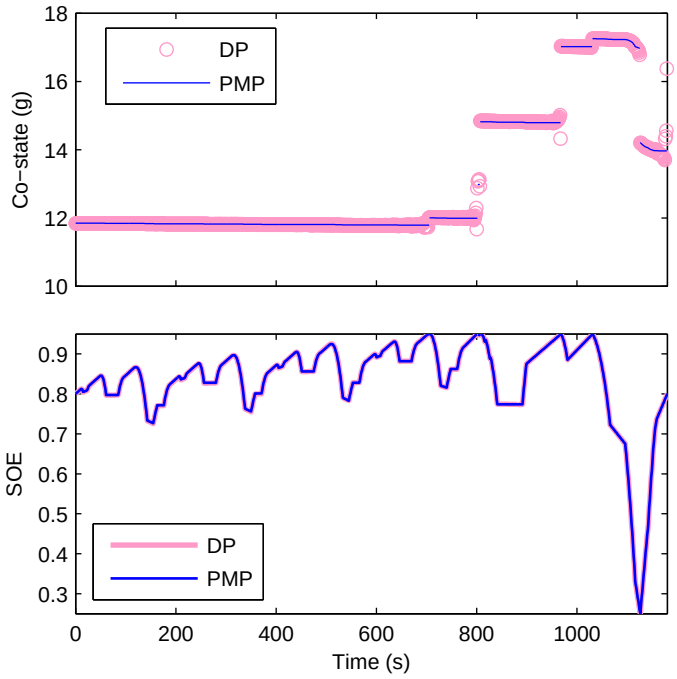

Figure 3.3: Comparison between DP and PMP in terms of state and co-state trajectories over NEDC.

Table 3.1: Mass and cost scaling factors for the FCS and supercapacitor.

	Mass	**Cost**
FCS	2.5 kg/kW	40 €/kW
Supercapacitor	0.51 kg/cell	30 €/cell

In the sizing process, the FCS power rating is varied between 0 and 100 kW, and the number of supercapacitor cells is varied between 0 and 300 cells. The hydrogen consumption is evaluated using PMP. For that purpose, the FCS power rating range is divided into 21 values with a step of 5 kW, and the number of supercapacitor cells is divided into 31 values with a step of 10 cells. PMP is then applied to calculate the best consumption for each pair of FCS size and supercapacitor size.

Figure 3.4 depicts the hydrogen consumption over NEDC and HWFET, where the consumption is displayed as isolines with labels indicating the hydrogen consumption in gram. The dark gray represents the impossible sizing, where the speed profile of the driving cycle cannot be followed completely, whereas the light gray highlights the region of insufficient sizing, where the drivability constraints are violated.

As done in Section 2.4, the Pareto front that represents the best trade-off between hydrogen consumption and cost has been extracted. By using the weighting procedure of equation (2.20), three solutions have been picked up from the Pareto front. The weight vector (w_1,w_2) of (1,0) prioritizes only the hydrogen consumption, and the weight vector of (0,1) prioritizes only the plant cost, whereas a vector of (0.5,0.5) equally favors the cost and consumption. The corresponding solutions are reported in Table 3.2 and Table 3.3 for NEDC and HWFET, respectively.

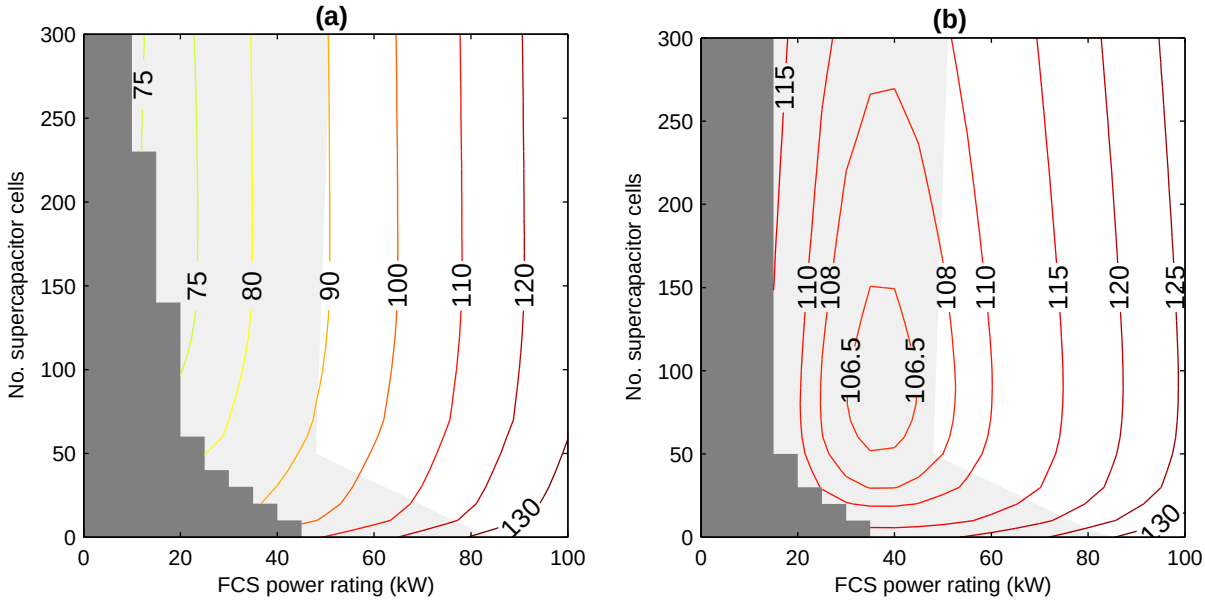

Figure 3.4: Hydrogen consumption (in gram) versus FCS power rating and number of supercapacitor cells. (a) NEDC; (b) HWFET.

Table 3.2: Numerical sizing results over NEDC.

	Unconstrained			**Constrained**		
(w_1,w_2)	(1,0)	(0.5,0.5)	(0,1)	(1,0)	(0.5,0.5)	(0,1)
Hydrogen consumption (g)	73.7	79.9	107.6	89.4	91.3	98.3
Cost (€)	5700	2500	1800	7400	4400	3400
FCS power rating (kW)	15	25	45	50	50	55
No. Cells (energy (Wh))	170 (516)	50 (152)	0 (0)	180 (547)	80 (243)	40 (122)

Table 3.3: Numerical sizing results over HWFET.

	Unconstrained			**Constrained**		
(w_1,w_2)	(1,0)	(0.5,0.5)	(0,1)	(1,0)	(0.5,0.5)	(0,1)
Hydrogen consumption (g)	106.0	108.5	118.5	107.4	108.0	109.7
Cost (€)	4100	2100	1400	4700	3500	3400
FCS power rating (kW)	15	25	45	50	50	55
No. Cells (energy (Wh))	90 (273)	30 (91)	0 (0)	90 (273)	50 (152)	40 (122)

As a summary of sizing process, the following points can be stated as a comparison between battery and supercapacitor as an ESS:

- The required supercapacitor energy for the minimum hydrogen consumption is far much less than that for the battery. This is mainly attributed to the significantly lower supercapacitor specific energy. E.g., one kWh ESS energy requires a 13.6 kg battery whereas it requires a 168 kg supercapacitor;
- The battery is oversized in terms of energy in order to fulfill the power requirements, so that the size of the battery is determined by its power. In contrast,

the supercapacitor is sized by its energy. For example, for an FCS of 50 kW, the minimum battery size (satisfying the acceleration constraint) was about 1 kWh in order to have a power of 29 kW at 60% SOC. In comparison, the minimum supercapacitor energy required to fulfill the same constraint is only 140 Wh achieving a power of 33 kW at 80% SOE. Smaller battery is not enough because of low power, whereas smaller supercapacitor is not enough because of the low energy so that the supercapacitor gets fully depleted before finishing the acceleration phase;

- Comparing the optimal powertrain size between battery and supercapacitor, the battery leads to more hydrogen-efficient and cost-efficient powertrain. This trend would only intensify if we consider the additional cost and mass of the supercapacitor converter, which has not been considered in this study. This may explain the fact that the vast majority of full hybrid vehicles currently use batteries as an ESS. This trend may change in future with increasing the energy density and decreasing the cost of supercapacitors.

Figure 3.5 compares the Pareto fronts of the battery for variable cycle life with that of the supercapacitor. For an ideal battery, the fuel cell/battery powertrain is more economical. The supercapacitor can become a favorable option compared to a battery with poor lifetime of 2000 cycles or less. The same conclusion is obtained by comparing the NEDC-normalized costs listed in Table 3.4 with Table 2.10. As said before, the supercapacitor requires increasing its energy density and reducing its cost to be competitive with the battery.

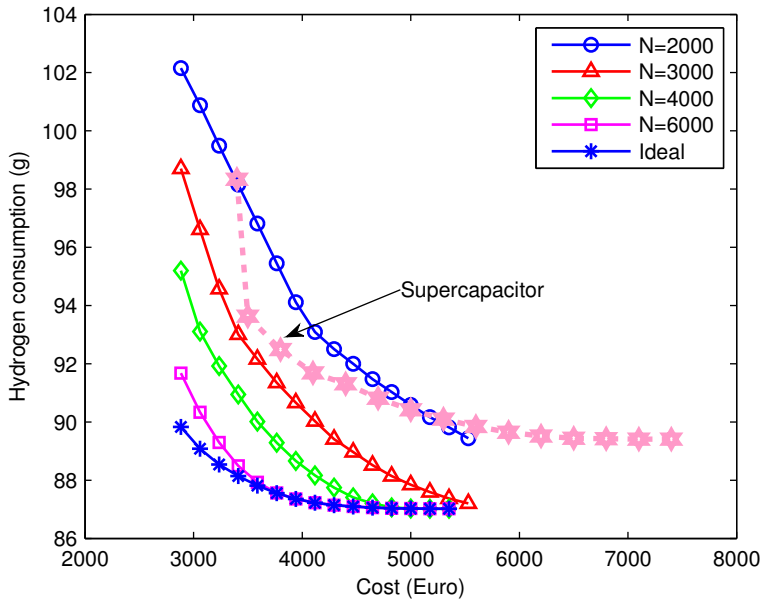

Figure 3.5: Comparison between supercapacitor and battery of variable cycle life in terms of Pareto front over NEDC.

In this study, the cold start-up time and cold start-up energy of FCS has not been considered. According to [10], the 2017 target for cold start-up time of FCS is 30 s. Vehicle operation during this phase (in addition to the possibility of using the ESS in heating up the FCS) may require significant energy from the ESS depending on the driving cycle. This issue would also favor battery over supercapacitor especially in FCHVs.

Table 3.4: Sizing optimization results over NEDC.

Hydrogen price (€/kg)	FCS (kW)	Supercapacitor (Wh)	NEDC-normalized cost in € (hydrogen, plant)
10	50	152	1.166 (0.936, 0.229)
5	50	152	0.698(0.468, 0.229)

3.4 Real-Time Strategy

The real-time controller used here is given by:

$$\lambda(t) = \lambda_0 + K_p \left(x_{ref} - x(t)\right) + K_i \int_0^t \left(x_{ref} - x(\tau)\right) \mathrm{d}\tau. \tag{3.5}$$

It has a proportional-integral (PI) form where λ_0 is the initial co-state, K_p is the proportional gain and K_i is the integral gain. The same controller scheme was used in Section 2.5 for the fuel cell/battery hybrid. However, the reference state is made variable for the supercapacitor as given by:

$$x_{ref}(t) = x_{f,ref} - K_{ref} \left(v(t)/v_{\max}\right)^2. \tag{3.6}$$

The reference state is proportional to the vehicle speed, $v(t)$, squared, with $x_{f,ref}$ is the reference state for zero speed and it is also the target final SOE, K_{ref} is a tuning parameter and v_{max} is the speed scaling factor which can be chosen as the vehicle top speed. Figure 3.6 depicts the structure of the real-time strategy, where the reference state variation with vehicle speed is represented by the block named Fcn. Using a variable reference state for the supercapacitor has been proposed in literature as a method to optimally exploit the already small ESS energy content [83]. It is based on the idea that increasing the vehicle speed (and, thus, its kinetic energy) increases the expected amount of recoverable braking energy in the future.

The real-time strategy used for the battery as an ESS in Section 2.5 had three tuning parameters, whereas the strategy used for the supercapacitor possess four parameters to be tuned by optimization, i.e., λ_0, K_p, K_i and K_{ref}. The parameters can be also optimized using the same formulation used for the battery as will be done in the next section.

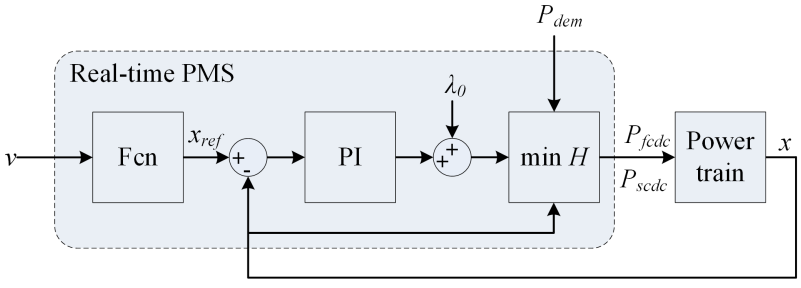

Figure 3.6: Schematic of the real-time power management strategy.

3.5 Experimental Study

In this section, the power management optimization of an experimental fuel cell/ supercapacitor hybrid system is carried out. The off-line optimal strategy is obtained using PMP, and the real-time strategy is optimized over UDDS (as a representative of city driving) and HWFET (as a representative of highway driving). The topology of Figure 3.1, with DC/DC converters in front of FCS and supercapacitor, is the main concern in this experimental study; an alternative topology is experimentally elaborated in Section 3.5.3.

The layout and specifications of the test bench are given in Appendix C. The vehicle power demand calculated by the vehicle model in Section 3.1 is divided by a scaling factor of 30 when it is applied to the test bench. The test bench supercapacitor is operated around 60% SOE.

The losses of the supercapacitor DC/DC converter lead to high optimal dynamics of the FCS power. The limitation of FCS power dynamics in the off-line optimization and real-time strategy has not been yet discussed because the ESS high efficiency encountered so far lead to relatively slow FCS dynamics (see Section 2.3.5). In addition to the typical optimization constraints (i.e., power and state constraints), the limitation of the P_{fcdc} change rate is accounted for here as a hard constraint; i.e.,

$$|\Delta P_{fcdc}/T_s| \leq \overline{\dot{P}_{fcdc}}, \tag{3.7}$$

where ΔP_{fcdc} is the change of P_{fcdc} between two successive time points, T_s is the sample time (of 1 s) and $\overline{\dot{P}_{fcdc}}$ is the value of rate limiter with W/s as a unit.

The constraint (3.7) is included in the formulation of PMP simply by limiting the range of control actions that is scanned when minimizing the Hamiltonian. This means that the dimensionality of the problem is kept unchanged; i.e., the supercapacitor SOE is the only state of the system. The global optimality of this approach will be discussed in Section 3.5.1. Other alternative methods to account for FCS dynamics in the optimization are discussed in Section 3.5.2.

The effect of FCS load dynamics on the hydrogen consumption is illustrated in Figure 3.7(a). The data points are recorded by varying $\overline{\dot{P}_{fcdc}}$ in the constraint (3.7) between 10 and 700 W/s, where 700 W/s represents the unconstrained case. For each value, the actual $\max(|\Delta P_{fcdc}/T_s|)$ and the relative increase in hydrogen consumption in comparison to the unconstrained case are obtained. There is a clear trade-off between the FCS dynamics and the hydrogen consumption, so that, for example, reducing the FCS dynamics from 450 W/s to 10 W/s is accompanied by an increase of 6% in hydrogen consumption over UDDS. This trade-off is attributed to the fact that reducing $\overline{\dot{P}_{fcdc}}$ narrows the admissible control window, over which the Hamiltonian is minimized, resulting in a less favorable value. In our case, the $\overline{\dot{P}_{fcdc}}$ of 10 W/s is considered from now on to put emphasis on the FCS life time which is strongly affected by its load dynamics. Figure 3.7(b) compares the optimal FCS converter power contribution over UDDS for the unconstrained case (corresponding to $\max(|\Delta P_{fcdc}/T_s|)$=450 W/s) and for the constrained case (corresponding to $\max(|\Delta P_{fcdc}/T_s|)$=10 W/s).

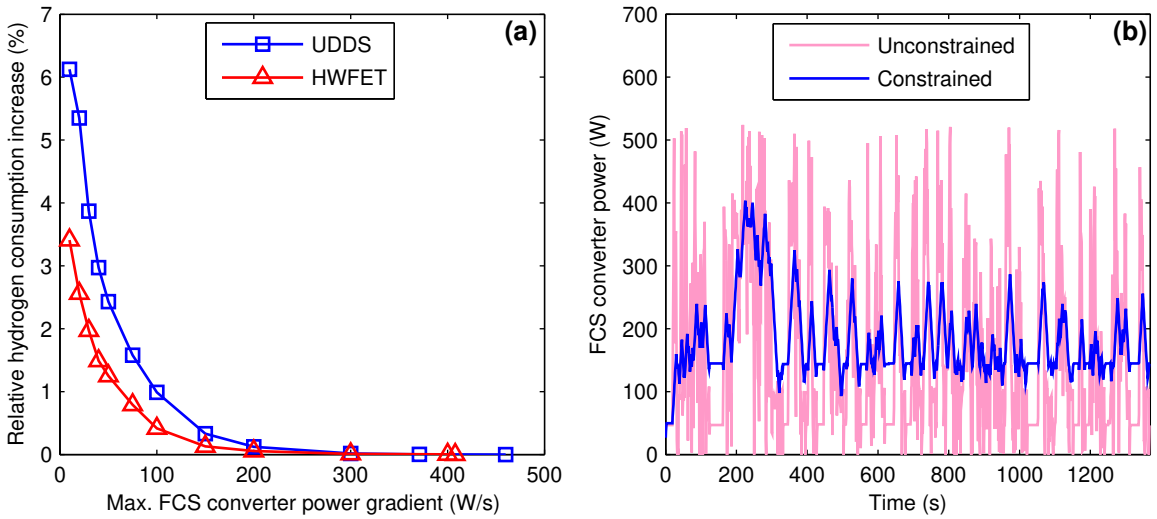

Figure 3.7: Effect of the allowed FCS dynamics on the off-line optimal strategy. (a) Effect on hydrogen consumption over UDDS and HWFET; (b) Effect on fuel cell power over UDDS.

The real-time PMS depicted in Figure 3.6 is adopted here with a reference state $x_{f,ref}$ of 0.6 and v_{max} of 100 km/h. The strategy parameters, λ_0, K_p, K_i and K_{ref}, are to be chosen by optimization. The ranges of the optimization variables are as follows: λ_0 is limited between 3 and 5, K_p between 0 and 100, K_i between 0 and 0.01 and K_{ref} between 0 and 0.3.

The resulting Pareto front is shown in Figure 3.8. To verify the optimality of the Pareto solutions, random sets of the PMS parameters are tested and the results are shown in Figure 3.8, as well. The performance of the random parameter sets in terms of J_1 indicates that the search space is only about 4% wide, which is the difference between the best and the worst J_1. This small optimization window is a result of the strong constraints on the FCS dynamics. For example, relaxing the allowed dynamics to 100 W/s would result in an optimization window of about 12%. The Pareto front indicates a small trade-off between the two objectives. The parameters that lead to the perfect charge sustenance (J_2=0) is considered so that the evaluation of the hydrogen consumption requires only one experimental run. This choice corresponds to the parameters: λ_0=3.50, K_p=36.95, K_i =0.0075 and K_{ref}=0.088. The performance of the PMS with the optimized parameters is subsequently experimentally evaluated.

Figures 3.9 and 3.10 show the experimental evaluation of the real-time strategy over UDDS and HWFET, respectively. The supercapacitor delivers the high dynamics of the load, whereas the FCS contribution is quite smooth with a maximum change rate of 10 W/s. The experiment reproduces the simulation results very well as illustrated by comparing the simulation and experiment in terms of state trajectories.

As said before, the use of two DC/DC converters, a unidirectional for the FCS and a bidirectional for the supercapacitor, achieves two goals: first, the control of bus voltage and, second, the active control of the sharing between the two power sources. As shown in Figure 3.11, the bus voltage is kept controlled around 37 V, even though the FCS and supercapacitor terminal voltages change with power (and state in case of supercapacitor). Keeping the bus voltage constant is advantageous in the electric vehicles in order to get the full power capability from the traction motor.

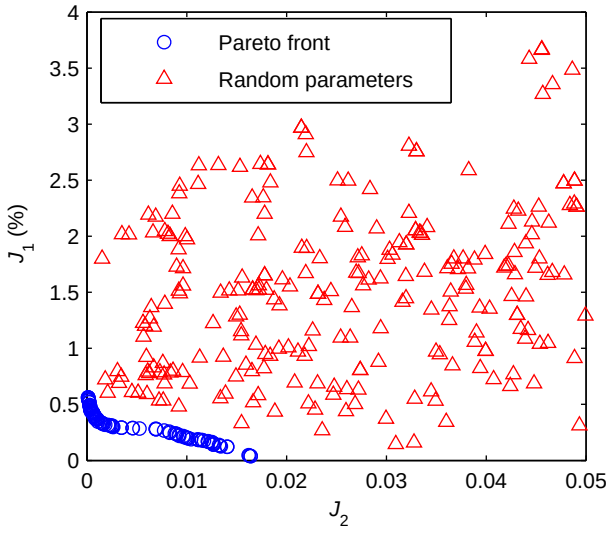

Figure 3.8: Optimization results of the real-time power management strategy.

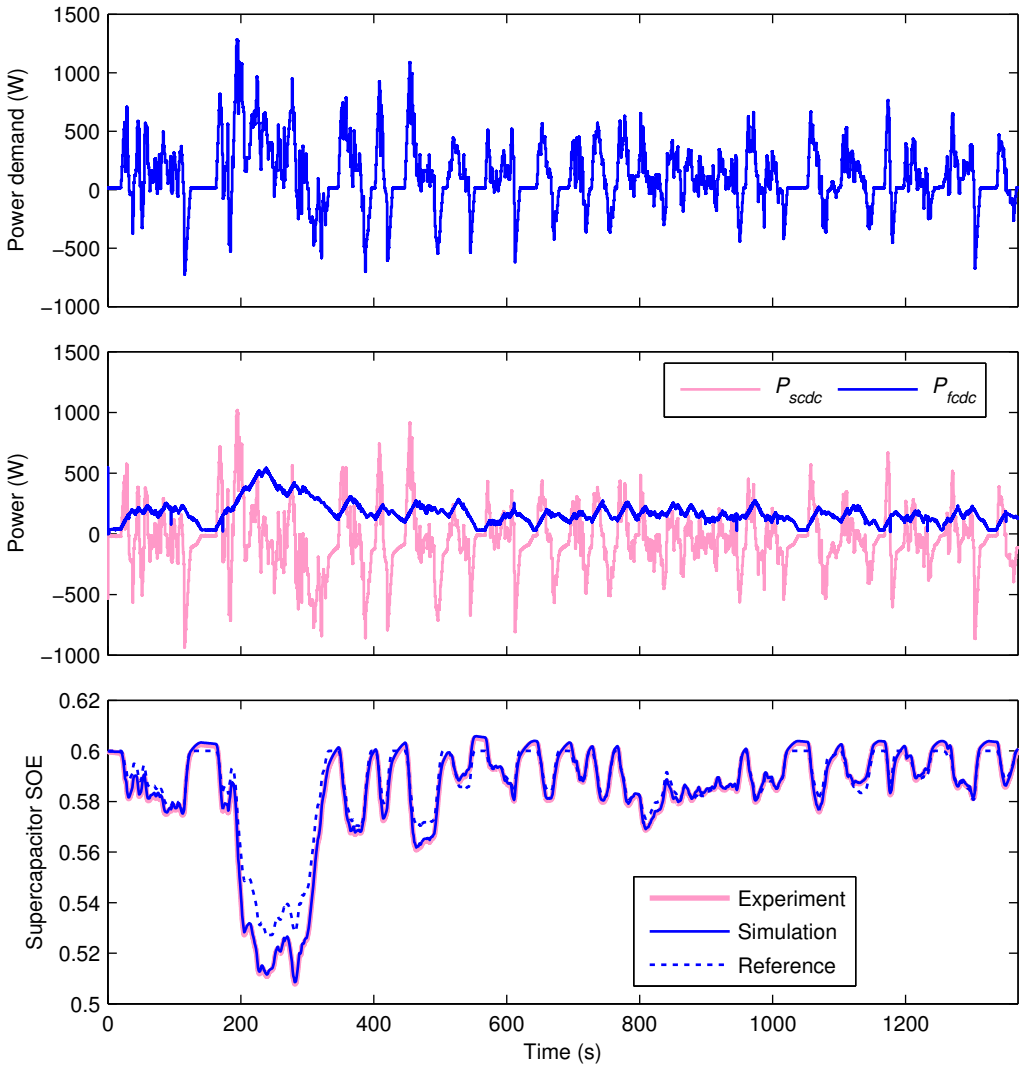

Figure 3.9: Experimental evaluation of the real-time power management strategy over UDDS.

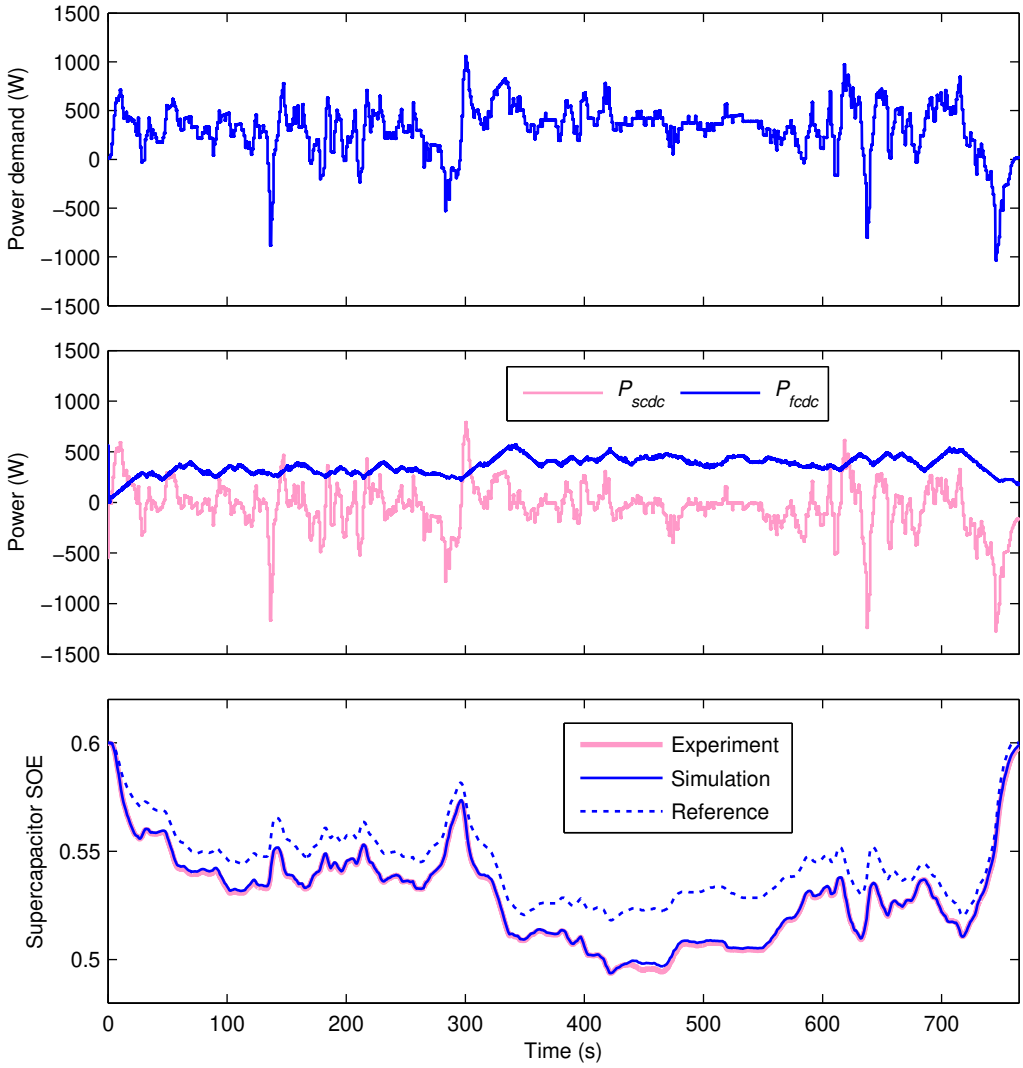

Figure 3.10: Experimental evaluation of the real-time power management strategy over HWFET.

Figure 3.12 illustrates a comparison between the off-line optimum and real-time PMS in terms of hydrogen consumption. The hydrogen consumption is shown versus the difference between the final SOE and the initial SOE. The off-line optimum is experimentally evaluated over each driving cycle by applying several optimal co-state trajectories. The charge sustaining off-line optimal hydrogen consumption can then be obtained by linear regression of the measurements. As expected from the design, the hydrogen consumption of the real-time PMS is within 1% of the off-line optimum.

3.5.1 Dynamic Programming

The correct formulation of the optimization problem when the FCS power dynamics is limited requires the definition of P_{fcdc} as a state of the system (in addition to the supercapacitor SOE), and its change between successive time points as the control variable of the system. The new state is governed in this case by the discrete dynamic equation:

$$P_{fcdc}(k+1) = P_{fcdc}(k) + u(k). \tag{3.8}$$

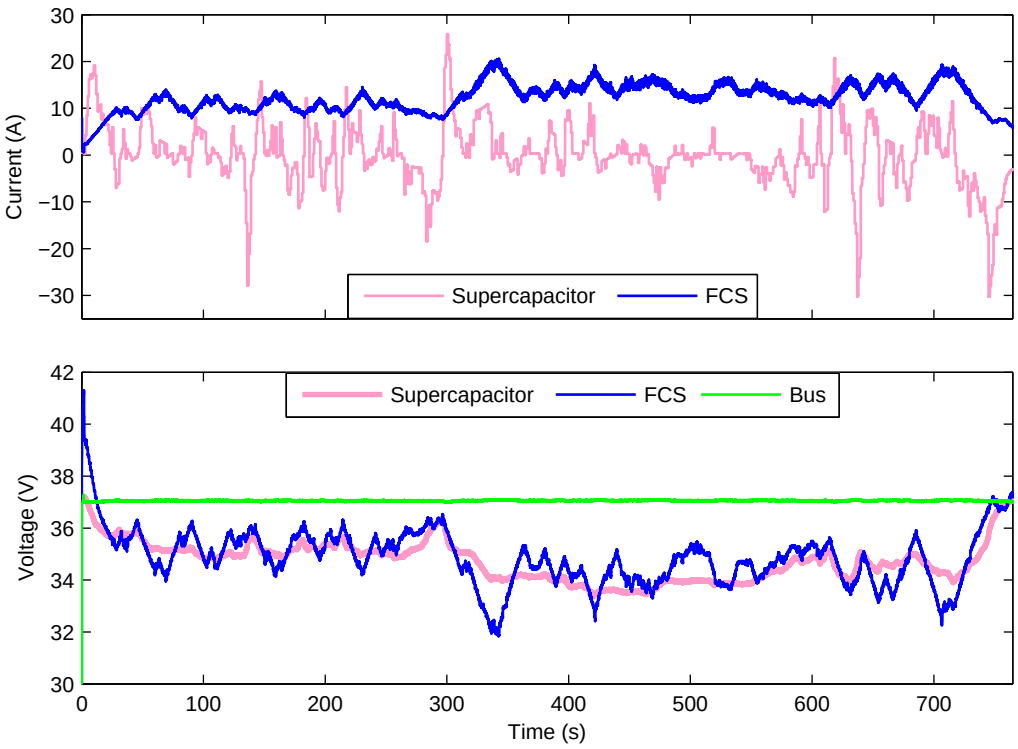

Figure 3.11: Current and voltage measurements over HWFET.

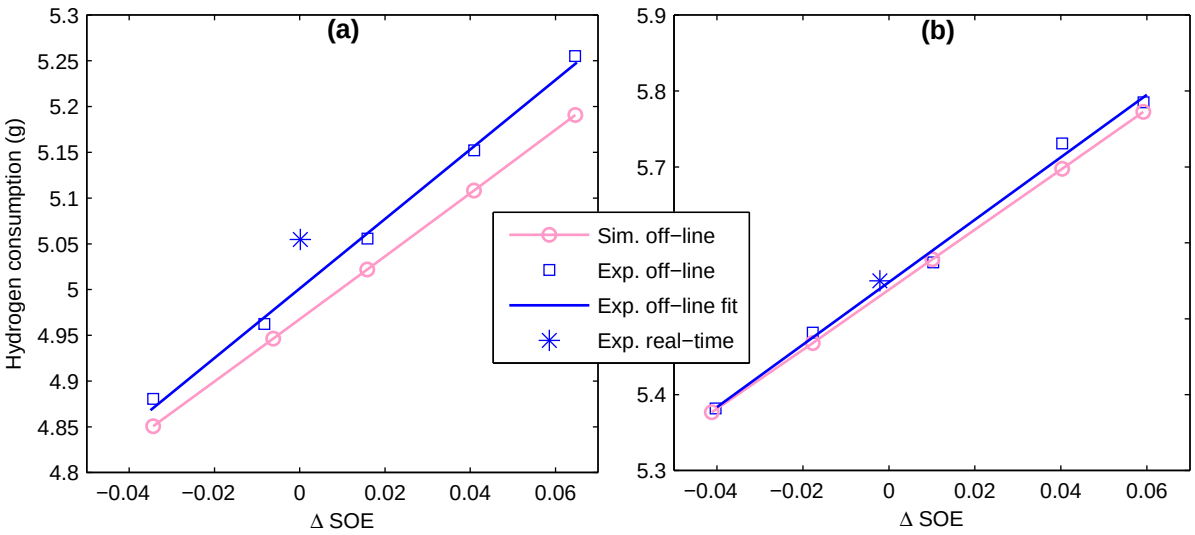

Figure 3.12: Experimental evaluation of the off-line optimal and real-time PMS in terms of hydrogen consumption as a function of the difference (final SOE – initial SOE). (a) UDDS; (b) HWFET.

The control variable, u, in this case is the change of the new state between successive time points. Therefore, it is limited between $-\overline{\dot{P}_{fcdc}}T_s$ and $+\overline{\dot{P}_{fcdc}}T_s$ according to constraint (3.7) if the optimal P_{fcdc} trajectory does not hit the lower and upper power limits of the FCS (i.e., $0 \leq P_{fcdc}(k) \leq 700$ W).

DP is applied to the constrained system with SOE and P_{fcdc} as two states and u as a control variable. SOE is discretized with a resolution of 0.001 and P_{fcdc} with a resolution of 10 W. The control action is discretized with a resolution of 1 W. A comparison between DP and PMP in terms of SOE trajectories over UDDS is depicted in Figure 3.13, for the

unconstrained and the constrained cases. As it is clear, for the unconstrained case, the two solutions are identical, whereas they differ for the constrained case. In terms of hydrogen consumption, DP and PMP consumption is identical for the unconstrained case, whereas, for the constrained case, DP consumes 1.7% and 0.7% less hydrogen than PMP over UDDS and HWFET, respectively.

The co-state associated with the new state, P_{fcdc}, is calculated from the derivative of the DP optimal cost-to-go function with respect to P_{fcdc} at each time point for the constrained case, and it is shown in Figure 3.14 over UDDS. The previous PMP formulation uses actually a suboptimal trajectory of the new co-state (i.e., a constant of zero), which resulted in the sub-optimality of PMP solution. The following question then arises: is it possible to account for P_{fcdc} as a state in the PMP? Theoretically this is possible, and the Minimum Principle states that the new co-state ends up at zero at the final time, since the corresponding state, P_{fcdc}, is free at the final time [25]. However, this has been proven difficult to tackle since the new co-state is of very low magnitude and any small error in its integration would result in a drift from the terminal boundary condition of zero, making the algorithm extremely difficult to converge.

3.5.2 Fuel Cell Dynamics Limitation Through Penalty Function

In the previous sections, the limitation of FCS dynamics has been achieved by a hard constraint on the power change rate. Another method to achieve that is to augment the cost function of the optimization problem (which has been so far the hydrogen consumption) by a penalty function that penalizes the change rate. For a proper formulation of such penalty function, the objective of the limitation needs first to be explicitly defined. Here

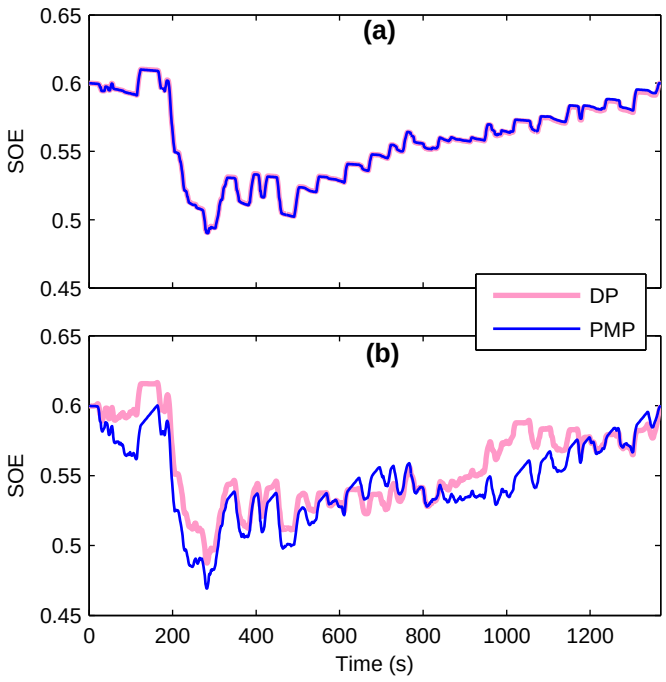

Figure 3.13: Comparison between DP and PMP state trajectories over UDDS. (a) Unconstrained FCS dynamics; (b) Constrained FCS dynamics.

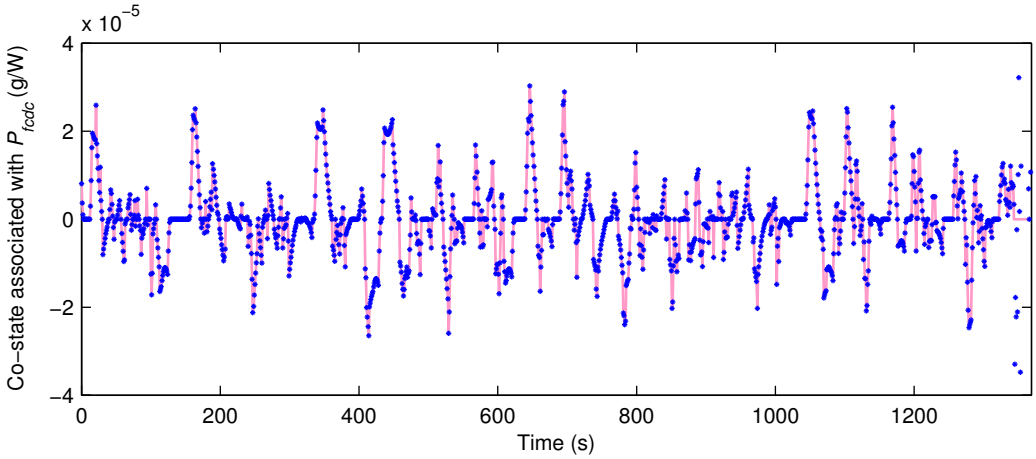

Figure 3.14: The optimal trajectory of the co-state associated with P_{fcdc} as calculated by DP for constrained FCS power dynamics over UDDS.

the objective is set to minimize the average power change rate over the driving cycle, so the two objectives are given by:

$$\begin{aligned} J_1 &= \sum_{k=0}^{K-1} T_s \dot{m}_h \left(P_{fcdc}(k)\right), \\ J_2 &= \frac{1}{K} \sum_{k=0}^{K-1} \frac{|\Delta P_{fcdc}(k)|}{T_s}, \end{aligned} \tag{3.9}$$

where J_1 is the hydrogen consumption and J_2 is the average change rate.

In order for the problem to be solvable using the off-line optimization algorithms, the two objectives need to be combined in one single objective, so that the total objective to be minimized can be formulated as follows:

$$\min \sum_{k=0}^{K-1} \left\{ T_s \dot{m}_h \left(P_{fcdc}(k)\right) + \alpha \left(\frac{|\Delta P_{fcdc}(k)|}{T_s} \right) \right\}, \tag{3.10}$$

where the coefficient α is introduced as a weighting factor. For different values of the coefficient α, different compromises between the two objectives J_1 and J_2 can be reached.

So far, we have illustrated two methods to limit the FCS dynamics: hard constraint and linear penalty function. The linear penalty function has been chosen because it matches the objective function J_2. Quadratic penalty function may also be used [84], where the combined objective function to be minimized is then given by:

$$\min \sum_{k=0}^{K-1} \left\{ T_s \dot{m}_h \left(P_{fcdc}(k)\right) + \alpha \left(\frac{|\Delta P_{fcdc}(k)|}{T_s} \right)^2 \right\}. \tag{3.11}$$

Figure 3.15 compares the three approaches to limit the FCS dynamics in terms of the obtained Pareto front with DP. As expected the linear penalty function achieves the best Pareto front. As said, this result is obtained because the linear penalty matches the objective J_2. The hard constraint gives the worst compromise between the two objectives.

This illustrates the idea that the method used to limit the FCS dynamics has an influence on the results. Choosing one method rather than the other requires a well defined objective that we want to minimize, and then the best way is to use a penalty function that matches this objective. The objective of limiting the FCS dynamics is to prolong its lifetime. Then, an explicit formula that relates the operating conditions to the FCS aging is required, which can then be embedded in the optimization problem as a penalty function.

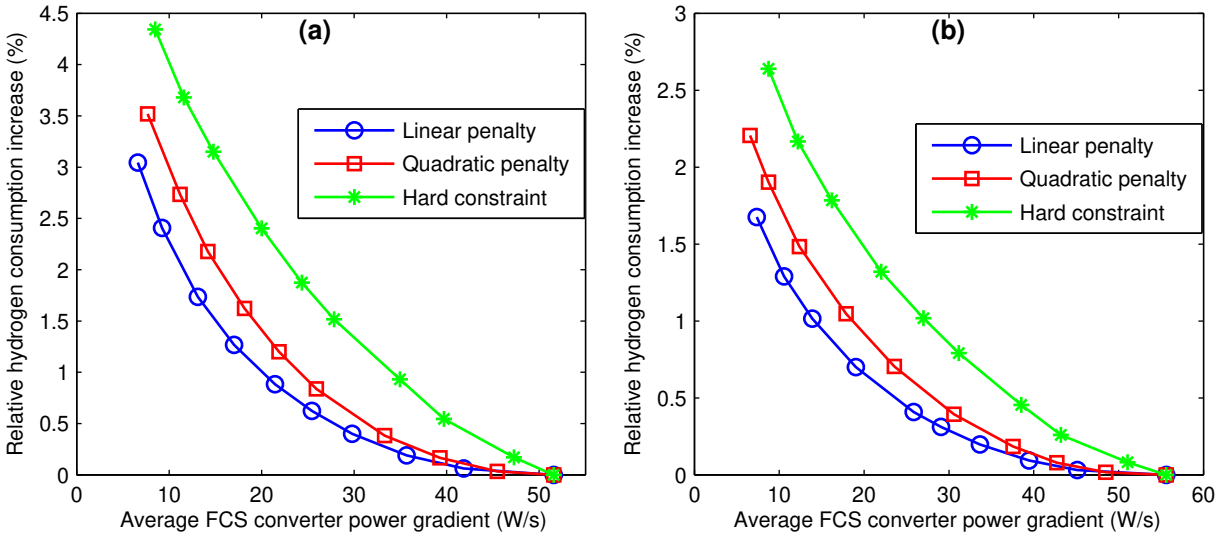

Figure 3.15: Comparison between three methods to limit the FCS dynamics. (a) UDDS; (b) HWFET.

3.5.3 Alternative Topology of Fuel Cell / Supercapacitor Hybrid

So far we have considered the fuel cell/supercapacitor topology shown in Figure 3.1, where two DC/DC converters are used; unidirectional one for the FCS and a bidirectional one for the supercapacitor. One converter is used to regulate the DC bus voltage, whereas the other is responsible for the realization of power distribution between the two power sources.

It is also possible to use the topology shown in Figure 3.16(a), where the FCS and supercapacitor are both connected directly to the bus without converters. This topology is used in Honda FCX fuel cell vehicle [17]. In this case, the bus voltage is determined by the supercapacitor, and the FCS power is determined by the bus voltage and the FCS characteristic polarization curve.

The operating principle of this topology is illustrated in Figure 3.16(b) which shows the FCS voltage as a function of its current (or power). The bus voltage is mainly determined by the supercapacitor SOC, whereas the supercapacitor power has a smaller effect due to its low internal resistance. For a bus voltage V_1, for example, according to the FCS characteristics, the FCS delivers the power P_1. For a lower supercapacitor SOC, corresponding to a voltage V_2, the contribution of the FCS increases. So, the system is self regulating, where the contribution of the FCS increases with decreasing supercapacitor charge level.

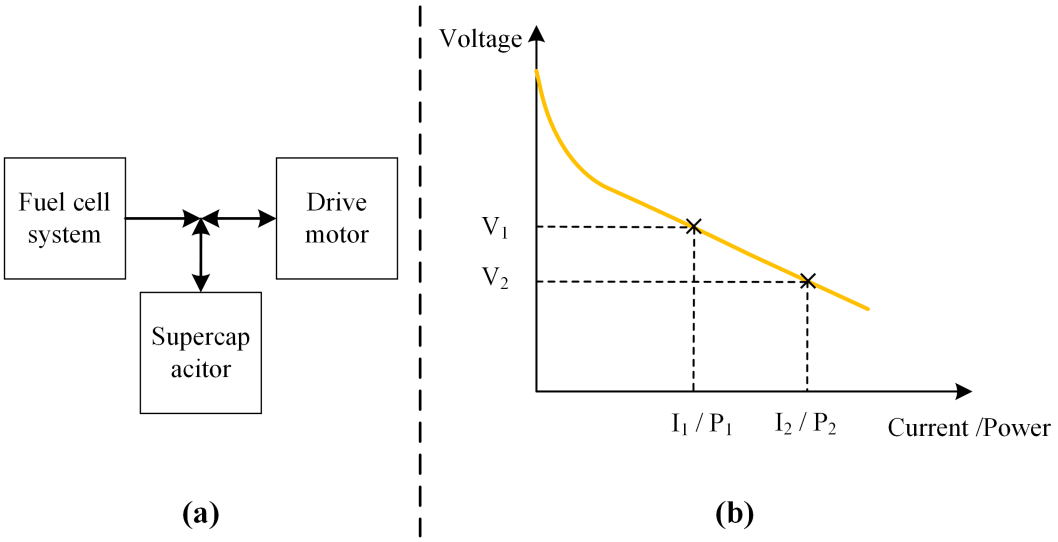

Figure 3.16: Direct coupling between fuel cell system and supercapacitor. (a) Topology schematic; (b) Operating principle for two bus voltage levels.

Figures 3.17 and 3.18 show the experimental evaluation over UDDS and HWFET, respectively. The results correspond to the charge sustaining performance where the initial and final supercapacitor voltage is the same. The FCS power follows the bus voltage, so that decreasing the bus voltage increases the FCS power as expected from the FCS polarization curve.

Having no converters makes the topology attractive since it saves the losses caused by the converters. Over UDDS, the hydrogen consumption was 3.00 g corresponding to a decrease of about 41% in comparison to the real-time strategy with converters. Likewise, for HWFET, the hydrogen consumption was 4.14 g corresponding to about 25% in comparison to the real-time strategy with converters. This significant hydrogen saving is not typical, because the efficiency of the converters in the test bench is relatively low in comparison to the typical efficiencies for the converters used in vehicles. However, this topology has three drawbacks:

- The bus voltage becomes variable, which determinately affects the high power capability of the traction motor;
- The ability to actively control the system is removed;
- This topology imposes limitations on the design voltages of the FCS and supercapacitor. The converters provide isolation between the power source and the DC bus so that the power source voltage may be higher or lower than the bus voltage. Therefore, with converters, the design voltages of the power sources can be chosen more freely.

3.6 Conclusions

In this chapter, fuel cell/supercapacitor hybrid systems for passenger vehicles were investigated in terms of PMS design and optimization, and in terms of powertrain sizing.

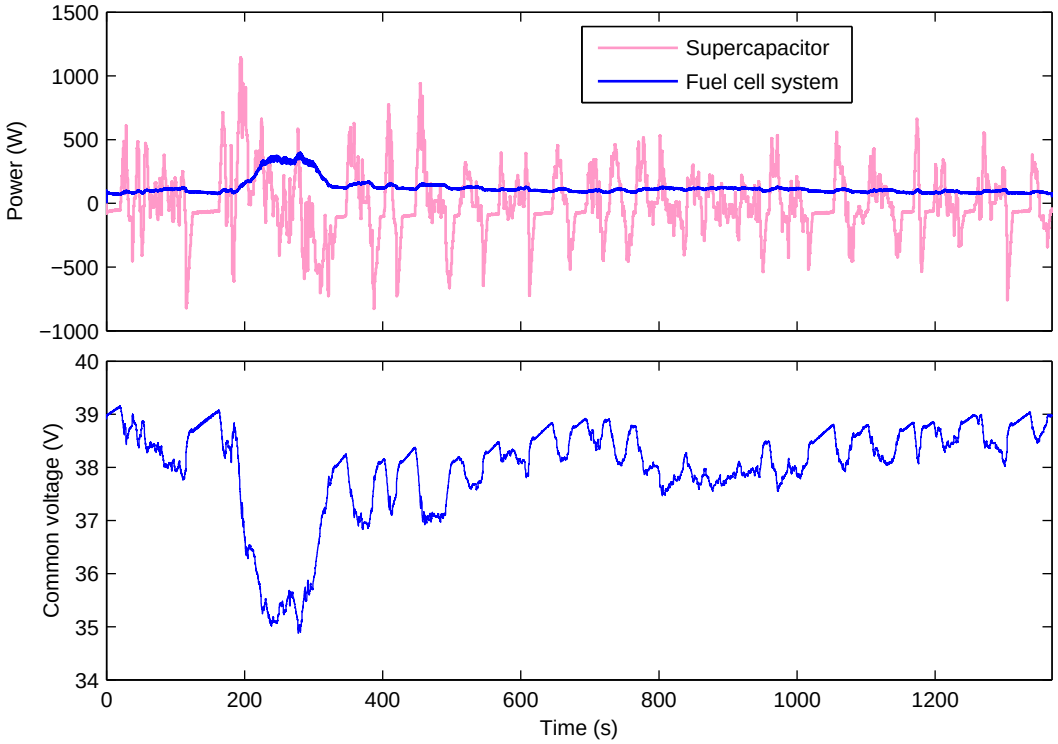

Figure 3.17: Experimental evaluation of the DC/DC converters-free fuel cell/supercapacitor topology over UDDS.

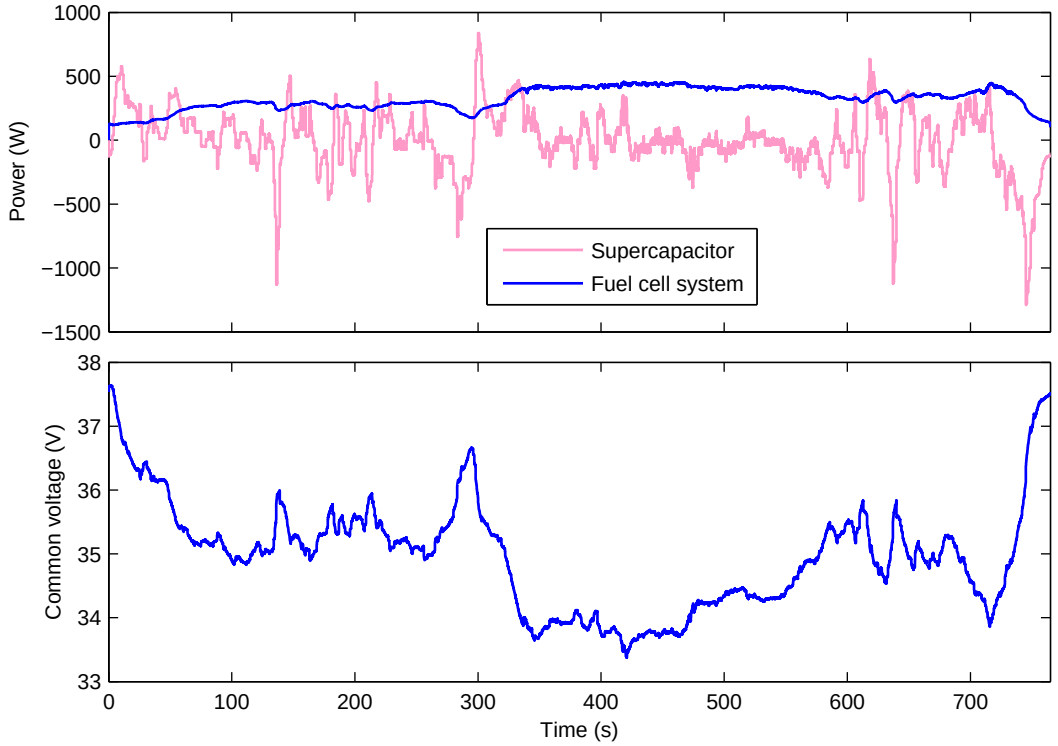

Figure 3.18: Experimental evaluation of the DC/DC converters-free fuel cell/supercapacitor topology over HWFET.

The same methodologies used for fuel cell/battery hybrid systems in Chapter 2 were used also here. DP and PMP were compared as two possible off-line optimization techniques, and it was found that both algorithms are identical in terms of the global optimality of the off-line PMS. A real-time capable PMS was designed and optimized while using the off-line optimal PMS as a benchmark.

The sizing of the power sources, i.e., FCS and supercapacitor, took into account hydrogen consumption and plant cost as two objectives. In comparison to batteries as an ESS, the supercapacitors resulted in less economical powertrain designs. Supercapacitors can be a more economical option only in comparison to batteries with short cycle life.

The off-line and real-time PMS optimization techniques were validated on a small-scale experimental fuel cell/supercapacitor hybrid system. The experimental measurements replicated the simulation results very well, thanks to the good models of the test bench components. The effect of FCS dynamics limitation on hydrogen consumption was investigated using a hard constraint on the FCS power change rate. Other methods, based on penalty functions, were additionally investigated to limit the FCS dynamics. The experimental evaluation inspected alternative passive self-regulating fuel cell/supercapacitor topologies without DC/DC converters.

Chapter 4

Fuel Cell/Battery/Supercapacitor Hybrid

In this chapter, a fuel cell/battery/supercapacitor vehicular hybrid system is investigated in terms of power management optimization. The same vehicle modeling approach used in Section 2.1 is adopted in Section 4.1, however, with a transit bus as an application. In Section 4.2, the two off-line optimization techniques, DP and PMP, are applied and compared in terms of the global optimality. The design and optimization of a real-time capable power management strategy is introduced in Section 4.3. Experimental results obtained from the test bench are presented in Section 4.4. This chapter is based on the two author's publications [85, 86].

4.1 Vehicle Model

A schematic of the fuel cell/battery/supercapacitor vehicle is shown in Figure 4.1. The battery is directly connected to the DC bus, whereas the FCS is coupled to the bus via a unidirectional DC/DC converter that enables the control of the FCS output power. A bidirectional DC/DC converter in front of the supercapacitor provides isolation between the supercapacitor and the battery that operates at different voltage level and enables the control of the supercapacitor power. Its bidirectional operation enables discharging and charging of the supercapacitor. The DC bus feeds the induction electric motor through an inverter. The motor shaft is coupled to the wheels through a single-speed transmission line that includes the reduction gearbox and differential.

The topology shown in Figure 4.1 is the typical one used for transit buses in literature [29, 51], due to its advantages over other possible alternative topologies. In this topology, the DC bus voltage is the same as the battery voltage, so that no direct bus voltage regulation exists. A bidirectional DC/DC converter can be placed between the battery and the DC bus enabling the DC bus voltage regulation, which is beneficial in order to get the full power capability of the traction motors all the time; however, this comes at the expense of additional hydrogen consumption due to the power losses in the converter. Moreover, in comparison to fuel cell/battery hybrid systems, the supercapacitor helps

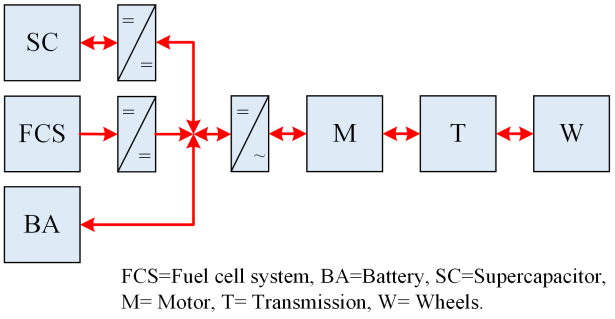

Figure 4.1: Schematic of fuel cell/battery/supercapacitor hybrid powertrain.

reduce the power burden on the battery by supplying most of the transient power demands and, therefore, the battery voltage does not change significantly. Another alternative topology is to place the bidirectional converter in front of the battery, rather than the supercapacitor. In this case, the bus voltage is determined by the supercapacitor, which exhibits strong voltage variations due to its low energy content (in comparison to the battery) and the high sensitivity of supercapacitor voltage to its charge level.

The parameters of the vehicle model are given in Table 4.1. The Citaro FuelCell Hybrid transit bus from Mercedes Benz [87] is used as a reference for the vehicle parameters. The vehicle is driven by two motors mounted on the rear axle. The same efficiency map of Figure 2.2 is used for each motor after scaling the speed and torque. In the braking phases, a maximum of 60% of the braking torque is assumed available for recuperation, whereas the rest is lost in the mechanical brakes.

Table 4.1: Transit bus model parameters.

	Parameter	**Value**
Vehicle	Mass, m (kg)	15000
	Drag coefficient, C_d	0.79
	Frontal area, A_f (m^2)	7.86
	Auxiliary power, P_{aux} (kW)	10
Wheels	Inertia, Θ_w($kg.m^2$)	20.5
	Radius, r (m)	0.48
	Friction coefficient, C_r	0.009
Transmission	Efficiency, η_{trans}	0.95
	Gear ratio, G	22.63
Motor	Number	2
	Max. torque (N·m)	465
	Max. speed (rpm)	11000
	Max. mechanical power (kW)	120
	Efficiency, η_m	Figure 2.2; speed scale (1.1), torque scale (1.72)
Constants	Gravity constant, g (m/s^2)	9.81
	Air density, ρ (kg/m^3)	1.2

As a result of the vehicle model, the power demand, P_{dem}, required at the DC bus is calculated as the sum of the traction motors power and the power required by the vehicle accessories. This total power should be met by the three power sources; i.e.,

$$P_{dem} = P_{fcdc} + P_b + P_{scdc}, \tag{4.1}$$

where P_{fcdc} is the output power of the FCS DC/DC converter (P_{fc} is the FCS output power), P_b is the battery power, and P_{scdc} is the output power of the supercapacitor DC/DC converter (P_{sc} is the supercapacitor power). Two transit bus driving cycles are used for the evaluation: Manhattan driving cycle and NurembergR36 driving cycle. Their speed profiles are shown in Figure 4.2.

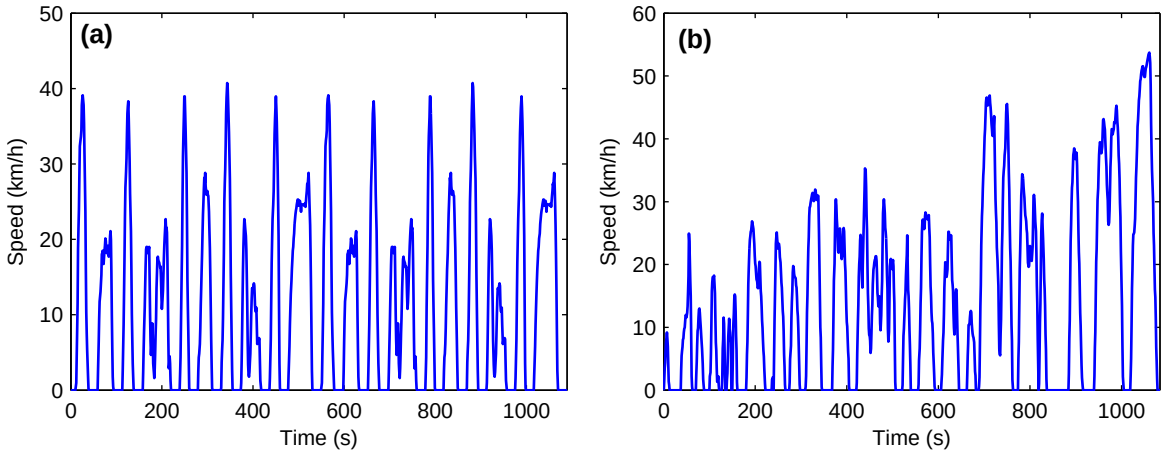

Figure 4.2: Evaluation driving cycles. (a) Manhattan; (b) NurembergR36.

The FCS has a maximum power rating of 120 kW and it is modeled by its efficiency shown in Figure 2.7. The FCS DC/DC converter is modeled by a constant efficiency of 95%.

The battery is modeled by its open circuit voltage, V_b, and its internal resistance, R_b. The battery state-of-charge (SOC) is used as the first state of the system (i.e., x_b=SOC), which is governed by the dynamic equation:

$$\begin{aligned} \dot{x}(t) &= \frac{-I_b(t)}{Q_b} = \frac{-1}{2R_bQ_b}\left(V_b - \sqrt{V_b^2 - 4R_bP_b(t)}\right), \\ &= f_b\left(x_b(t), P_b(t)\right). \end{aligned} \tag{4.2}$$

The function f_b is generally a function of SOC since the two parameters, V_b and R_b, depend on SOC; however, as will be seen later, the optimal SOC trajectory spans a narrow SOC window and, therefore, the two parameters are assumed constant. This assumption is particularly valid for Li-Iron Phosphate (LIP) battery cell, where the open circuit voltage stays almost constant at 3.3 V over a wide SOC operation range. The 20 Ah LIP prismatic cell AMP20 from A123 Systems is considered as the building block of the battery bank. The cell open circuit voltage and the cell internal resistance have been estimated from the product datasheet [88] to be 3.3 V and 2 mΩ , respectively. Two hundred cells are connected in series, with which a nominal DC bus voltage of about 650 V is obtained.

The supercapacitor state-of-energy (SOE) is used as the second state of the system (i.e., x_{sc}=SOE), which is governed by the dynamic equation:

$$\begin{aligned} \dot{x}_{sc}(t) &= \frac{-I_{sc}V_{sc}}{E_{sc}} = \frac{-V_{sc}}{2R_{sc}E_{sc}}\left(V_{sc} - \sqrt{V_{sc}^2 - 4R_{sc}P_{sc}(t)}\right), \\ &= f_{sc}\left(x_{sc}(t), P_{sc}(t)\right). \end{aligned} \tag{4.3}$$

The building block of the supercapacitor bank is the Boostcap BCAP3000P270 from Maxwell Technologies, which is characterized by a capacitance of 3000 F, a rated voltage of 2.7 V, and an internal resistance of 0.29 mΩ [81]. The supercapacitor bank is formed by 320 cells connected in series. The DC/DC converter efficiency, η_{scdc}, is assumed constant of 95%.

4.2 Off-Line Optimization

The off-line optimal power management strategy (PMS) refers to the strategy that globally minimizes the hydrogen consumption over a specific driving cycle between given initial and final system states. The objective function to be minimized is then given by:

$$J = \int_0^{t_f} \dot{m}_h\left(P_{fcdc}(t)\right) \mathrm{d}t. \tag{4.4}$$

The optimization problem is constrained by the power limits of the three power sources as expressed in (4.5). The FCS power is limited by its power rating. The battery power is limited by the cell allowed terminal voltage and the constraints on the DC bus voltage. The minimum/maximum cell terminal voltage is 1.65 V/3.8 V and the DC bus voltage is limited to 400-800 V (corresponding to 2-4 V per cell), meaning the cell terminal voltage is limited to 2-3.8 V, which corresponds to about 260 kW maximum discharging power and about 190 kW maximum charging power. The supercapacitor power is limited by the monitoring electronics and the DC/DC converter; in the optimization, the limits of ±300 kW are used for P_{scdc}. In addition to the state dynamic equations (4.2) and (4.3) , the system states are constrained within a certain window. x_b is limited between 0.45 and 0.75. x_{sc} is allowed to be between 0.25 and 0.95 at any time. The initial system states, $x_{b,0}$ and $x_{sc,0}$, and the final states, $x_{b,f}$ and $x_{sc,f}$, should be predefined. For the evaluation, the initial and final battery state is set to 0.6, whereas the initial and final supercapacitor state is set to 0.8.

$$\begin{aligned} &P_{fcdc,\min} \le P_{fcdc} \le P_{fcdc,\max}, \\ &P_{scdc,\min} \le P_{scdc} \le P_{scdc,\max}, \\ &P_{b,\min} \le P_b \le P_{b,\max}, \\ &x_{b,\min} \le x_b \le x_{b,\max}, \qquad x_{sc,\min} \le x_{sc} \le x_{sc,\max}, \\ &x_b(0) = x_{b,0}, \qquad x_{sc}(0) = x_{sc,0}, \\ &x_b(t_f) = x_{b,f}, \qquad x_{sc}(t_f) = x_{sc,f}. \end{aligned} \tag{4.5}$$

In the subsequent sections, two algorithms are used to solve the off-line optimization problem: DP and PMP. Sections 2.2.1 and 2.2.2 give the formulation of DP and PMP, respectively, for a single-state single-control system, where the battery SOC was the only state and the FCS power was the only control variable. In comparison, for the triple hybrid system, fuel cell/battery/supercapacitor, we have two states and two control variables. Therefore, it is worth restating the algorithms formulation. To simplify the formulation of the subsequent equations, the column vectors $\mathbf{x} = [x_b, x_{sc}]^{\mathrm{T}}$, $\mathbf{f} = [f_b, f_{sc}]^{\mathrm{T}}$, and $\mathbf{u} = [P_b, P_{sc}]^{\mathrm{T}}$ will be used, where the superscript T stands for transpose.

4.2.1 Dynamic Programming (DP)

The algorithm starts by discretizing the time span of the driving cycle into K+1 points with a sample time T_s. Two-dimensional state grid is established at each time point, where one dimension corresponds to x_b (with M+1 levels and a state resolution of Δx_b) and the second dimension corresponds to x_{sc} (with N+1 levels and a state resolution of Δx_{sc}). Likewise, two-dimensional control space with the resolutions ΔP_b and ΔP_{sc} is used. Then, the optimal cost-to-go function is evaluated at each time point k and each state-space point in a recursive manner starting from the final sample time K as expressed by:

$$\begin{aligned} J_k^*(\mathbf{x}^{m,n}) &= \min_{\mathbf{u}\in\mathbf{U}(k)} \left\{ \dot{m}_h(\mathbf{u},k)T_s + J_{k+1}^*\left(\mathbf{x}^{m,n} + T_s\mathbf{f}(\mathbf{x}^m,\mathbf{u})\right)\right\}, \\ & \quad k = 0,\, 1,\, \ldots,\, K;\; m = 0,\, 1,\, \ldots,\, M;\; n = 0,\, 1,\, \ldots,\, N. \end{aligned} \tag{4.6}$$

The subscript k refers to the time point and the superscripts (m, n) refer to a state point on a state grid. $J_k^*(\mathbf{x}^{m,n})$ represents the minimum hydrogen consumption that can be achieved starting from the state $\mathbf{x}^{m,n}$ at time point k and ending at the final state $\mathbf{x}_f = [x_{b,f}, x_{sc,f}]^{\mathrm{T}}$ at the final time point K. The final cost-to-go value, J_K^*, is set to zero for $\mathbf{x}_f$ and a large value otherwise in order to consider only the solutions that lead to $\mathbf{x}_f$. The result of the minimization is an optimal state-feedback control law that relates each state point and each time point with the corresponding optimal control that minimizes the cost-to-go. The optimal control map is then used to calculate the optimal DP solution moving forward in time starting from the predefined initial states. For the implementation of DP, the following settings are used: Δx_b=Δx_{sc}=0.001 and ΔP_b=ΔP_{sc}=1 kW.

4.2.2 Pontryagin's Minimum Principle (PMP)

The PMP uses the concept of the system Hamiltonian defined as follows:

$$H(\mathbf{x},\mathbf{u},\boldsymbol{\lambda},k) = \dot{m}_h(\mathbf{u},k) - \boldsymbol{\lambda}^{\mathrm{T}}\mathbf{f}(\mathbf{x},\mathbf{u}), \tag{4.7}$$

where $\boldsymbol{\lambda} = [\lambda_b, \lambda_{sc}]^{\mathrm{T}}$, and λ_b and λ_{sc} are the co-states (i.e., Lagrange multipliers) associated with x_b and x_{sc}, respectively. The Minimum Principle states that the optimal control variable minimizes the Hamiltonian, that is:

$$H(\mathbf{x}^*,\mathbf{u}^*,\boldsymbol{\lambda}^*,k) \leq H(\mathbf{x}^*,\mathbf{u},\boldsymbol{\lambda}^*,k). \tag{4.8}$$

According to the Minimum Principle, the optimum co-states are governed by:

$$\begin{aligned}\dot{\boldsymbol{\lambda}}^* &= \frac{\partial H}{\partial \mathbf{x}}(\mathbf{x}^*, \mathbf{u}^*, \boldsymbol{\lambda}^*, k), \\ &= -\left[\lambda_b^* \frac{\partial f_b}{\partial x_b}\left(x_b^*, P_b^*\right), \lambda_{sc}^* \frac{\partial f_{sc}}{\partial x_{sc}}\left(x_{sc}^*, P_{sc}^*\right)\right]^{\mathrm{T}}. \end{aligned} \tag{4.9}$$

The function f_b in equation (4.2) is, in general, a function of x_b, since V_b and R_b vary with x_b; however, as stated earlier, these two parameters are assumed constant and, therefore, f_b becomes independent of x_b. As a result, according to equation (4.9), the optimal co-state, λ_b^*, is constant. This does not apply to λ_{sc}^*, since V_{sc}, and hence f_{sc}, depends on x_{sc}.

In summary, PMP requires the evaluation of the Hamiltonian at each time point to calculate the optimal control actions. This requires the optimal co-states to be known at each time. equation (4.9) defines the evolution of the optimal co-states with time. It can be integrated forward starting from an initial value $\boldsymbol{\lambda}_0$. As it is known from the single-state case, the co-states are determined by the predefined final states, $\mathbf{x}_f$. So, in order to calculate the optimal initial co-states that lead to $\mathbf{x}_f$, an iterative procedure over the entire driving cycle is required. At iteration i, where $\boldsymbol{\lambda}_0^i$ is used, the difference between the obtained final states and the required ones is evaluated and the initial co-states at iteration i+1 are calculated by Newton's method expressed in equation (4.10) with the help of the Jacobian matrix at iteration i, $\Im^i$. The iterations stop once the required final states are obtained (within a resolution of 0.001 for both states).

$$\boldsymbol{\lambda}_0^{i+1} = \boldsymbol{\lambda}_0^i + \left[\Im^i\right]^{-1}\left(\mathbf{x}_f - \mathbf{x}_f^i(t_f)\right), \quad \text{where } \Im^i = \left.\frac{\partial \mathbf{x}(t_f)}{\partial \boldsymbol{\lambda}_0}\right|_{\boldsymbol{\lambda}_0^i}. \tag{4.10}$$

Using equation (4.10), the two initial co-states, $\lambda_b(0)$ and $\lambda_{sc}(0)$, are tuned simultaneously for the final states $x_b(t_f)$ and $x_{sc}(t_f)$ to match their preset values, $x_{b,f}$ and $x_{sc,f}$. If the resulting states trajectories respect the states bounds constraints, the problem is solved. Otherwise, an algorithm is needed to account for those constraints. The algorithm of Section 2.2.2.1 works for one state; an extension is proposed here to account for two states where the bounds constraints of supercapacitor SOE can get active. The case where the battery SOC bounds constraints are also active is not encountered and hence not considered. The algorithm for the two-state system is outlined below:

1. Solve the unconstrained problem to get the initial co-states $\lambda_b(0)$ and $\lambda_{sc}(0)$ with the help of equation (4.10). As a result, we get a solution for the unconstrained problem that leads to the target final states. If the resulting states trajectories already respect their bounds, the problem is done; otherwise continue to the next step;

2. With the help of $\lambda_b(0)$ resulting from the step (1), the algorithm of Section 2.2.2.1 is applied to recursively find out the contact times of x_{sc} with the bounds, so that the resulting x_{sc} trajectory respects the constraints;

3. It is possible that, due to the activation of x_{sc} constraints in step (2), $x_b(t_f)$ does not coincide with the target value, $x_{b,f}$, rather a deviation of $\Delta = x_b(t_f) – x_{b,f}$ arises, where Δ is larger than the resolution of 0.001. In this case, the algorithm is repeated from step (1) with a new target final x_b of $x_{b,f} – \Delta$ instead of $x_{b,f}$.

Figures 4.3 and 4.4 depict a comparison between PMP and DP in terms of the resulting states and co-states trajectories over Manhattan and NurembergR36, respectively. Over Manhattan, PMP achieves a hydrogen economy of 11.853 kg/100 km in comparison to 11.855 kg/100 km for DP. Over NurembergR36, hydrogen consumptions of 10.077 kg/100 km and 10.079 kg/100 km are obtained with PMP and DP, respectively. Therefore, both algorithms achieve almost the same hydrogen consumption with a difference below 0.02%. Those tiny discrepancies between the two algorithms in terms of hydrogen economy and states trajectories are attributed to the truncation errors and the finite resolution used in each one of them, and the their results can be practically considered identical.

In terms of computation time and memory requirements, PMP requires negligible resources in comparison to DP. The exact time reduction depends on many factors like the state resolution and the code optimization. In our case, the PMP solution could be obtained within few minutes whereas the DP required hours. In terms of memory requirements, for DP, a map of $K\times(N+1)\times(M+1)$ elements of the optimal control polices resulted from equation (4.6) are kept in memory for post processing (i.e., calculation of the optimal states trajectories starting from $k=0$). DP takes an acceptable time for a single energy storage (and hence one state and one control variable). The computation time and memory requirements increase exponentially with the number of states and control variables. This phenomenon is usually referred to in literature as the "curse of dimensionality".

Figure 4.5 shows the off-line optimal power distribution over Manhattan between battery and supercapacitor. The high optimal battery contribution seems at first counterintuitive if we consider the fact that the supercapacitor has a higher efficiency than the battery as expressed by its lower internal resistance. This is attributed to the inefficiency of the

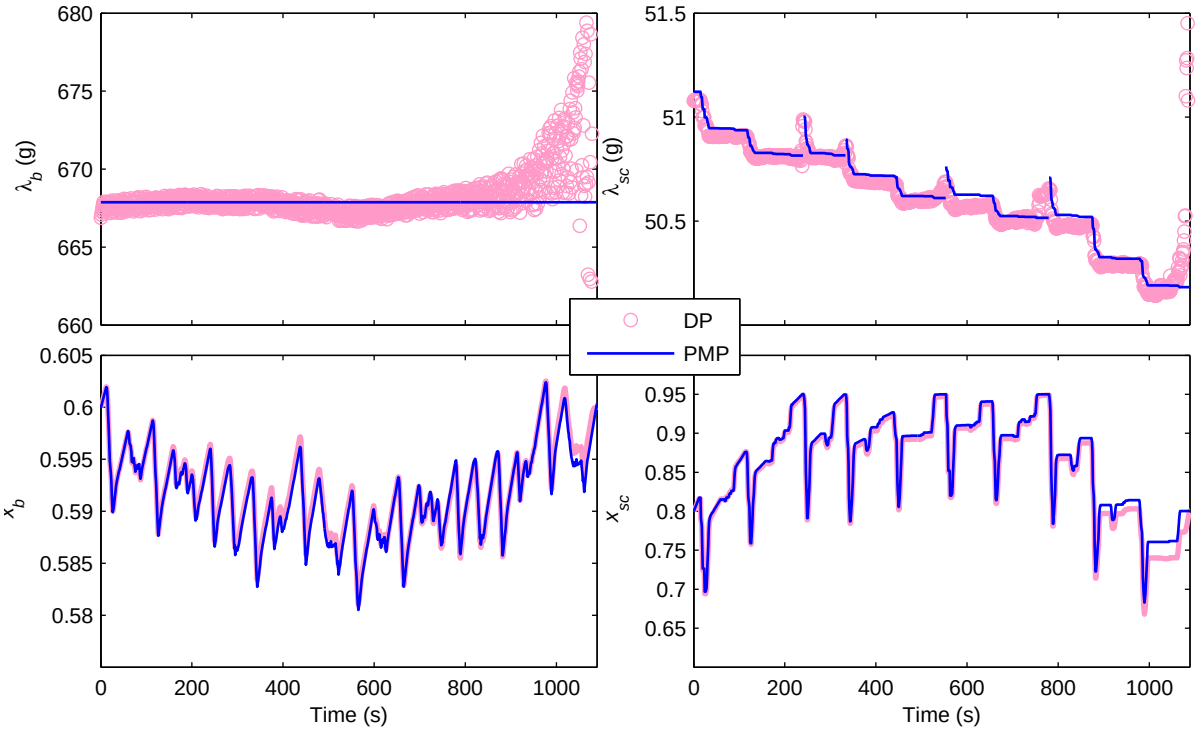

Figure 4.3: Off-line optimal states and co-states trajectories over Manhattan driving cycle.

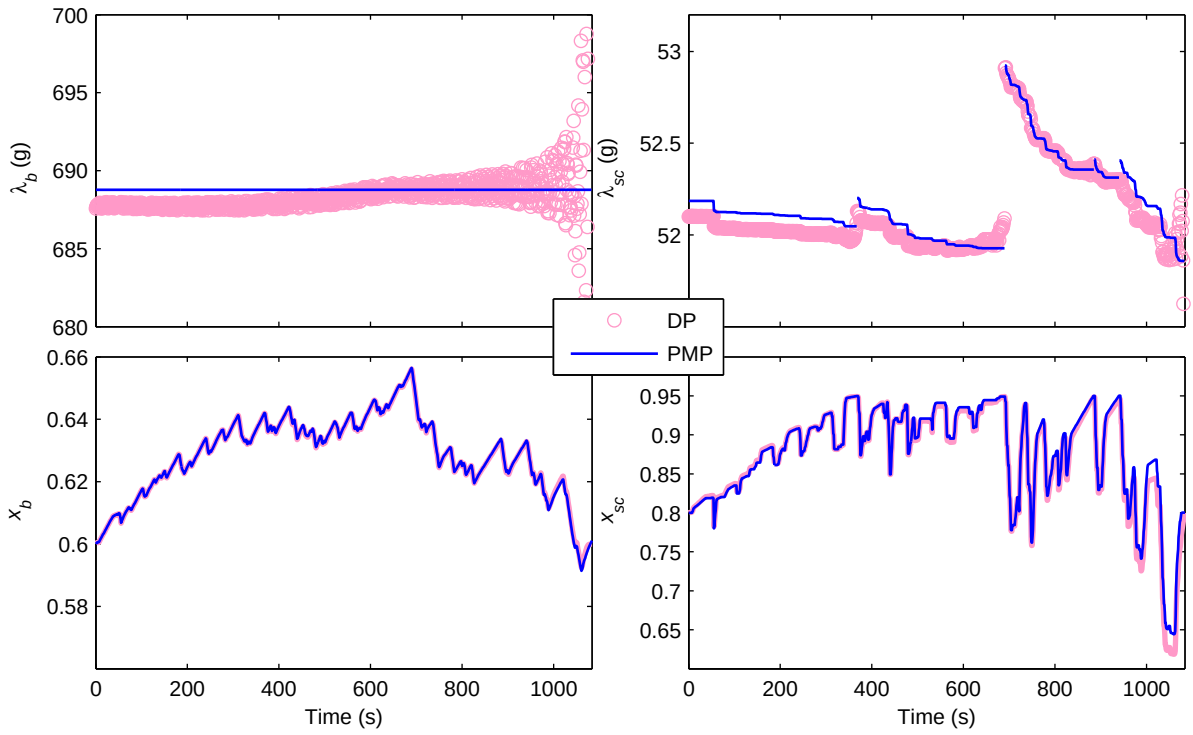

Figure 4.4: Off-line optimal states and co-states trajectories over NurembergR36 driving cycle.

supercapacitor DC/DC converter that overshadows the high supercapacitor efficiency.

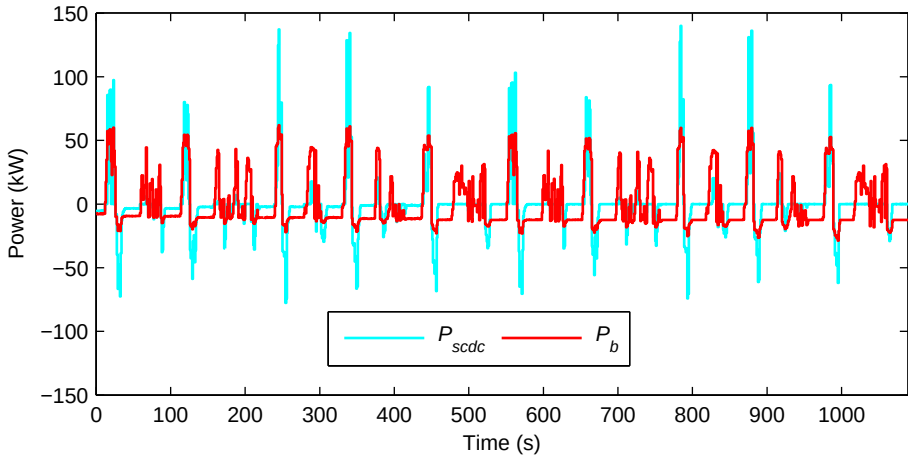

Figure 4.5: Off-line optimal power distribution between battery and supercapacitor over Manhattan driving cycle.

Table 4.2 compares three ESS scenarios: battery only; battery and supercapacitor with η_{scdc}=95% (i.e., base configuration); battery and supercapacitor with η_{scdc}=100%. The comparison includes the average battery loading (defined as the average absolute battery power), the hydrogen consumption (with the base configuration used as a reference of 0%), the round-trip efficiency (defined as the ratio of the discharged energy to the charging energy), and the average thermal power produced by the battery internal resistance, the supercapacitor internal resistance and the supercapacitor DC/DC converter. The results correspond to the off-line optimal PMS over Manhattan. Adding the supercapacitor to the battery improves the hydrogen consumption and reduces the battery loading and

Table 4.2: Effect of the ESS type and the supercapacitor DC/DC converter efficiency on the off-line optimal power management strategy over Manhattan driving cycle. BA=Battery; SC=Supercapacitor; DC=DC/DC converter.

ESS	η_{scdc} (%)	Av. BA power (kW)	Hydrogen consumption	Round-trip efficiency (%)			Av. thermal power (W)		
				BA	SC	SC+DC	BA	SC	BA+SC
BA	-	24.0	+2.2%	90.3	-	-	1220	0	1220
BA+SC	95	16.7	0%	94.9	98.3	88.7	434	81	515
BA+SC	100	4.4	-3.1%	96.8	98.3	98.3	71	200	271

its thermal power. Increasing η_{scdc} from 95% to 100% results in a dramatic reduction in battery loading and in the thermal power produced by the complete ESS. As stated before, the optimal distribution of power between the battery and the supercapacitor depends very much on η_{scdc} since the supercapacitor DC/DC converter is the main cause of losses when charging or discharging the supercapacitor.

The off-line optimization techniques cannot be used directly in real-time because they assume a complete knowledge of the driving cycle. Additionally, the off-line optimal solution takes only the hydrogen consumption into account without considering other important factors such as the battery power burden (and hence its lifetime). The battery in the off-line optimal strategy is unnecessarily overloaded, so that the advantage of using the supercapacitor is not fully exploited. This issue is dealt with when designing and optimizing the real-time PMS in the next section. However, the off-line optimal solution provides a benchmark that can be used when evaluating the real-time strategy. Additionally, the off-line optimum may provide some hints that can be useful for the design of the real-time strategy. For example, as can be seen from Figure 4.5, the battery power and the supercapacitor power have always the same sign, meaning that there is no charge exchange between them. This behavior is understandable considering the fact that any such charge exchange would be accompanied by losses in the battery, the supercapacitor, and its DC/DC converter. The real-time PMS will make use of this idea in the next section.

4.3 Real-Time Strategy

As illustrated in Figure 4.6(a), the fuel cell/battery/supercapacitor hybrid is a multiple-input-multiple-output system (MIMO), with P_{fcdc}, P_b and P_{scdc} as inputs (i.e., manipulated variables), and x_b and x_{sc} as outputs (i.e., controlled variables). The PMS takes as inputs the system states together with the vehicle speed and power demand, and distributes the demand among the power sources. The detailed structure of the proposed PMS is depicted in Figure 4.6(b). The PMS is based on two decoupled control loops: one for x_b with P_{fcdc} as the corresponding manipulated variable, and the other loop controls x_{sc} with P_b as manipulated variable. P_{scdc} is readily determined by the power balance.

The FCS power is determined by a proportional-integral controller (PI) of the battery

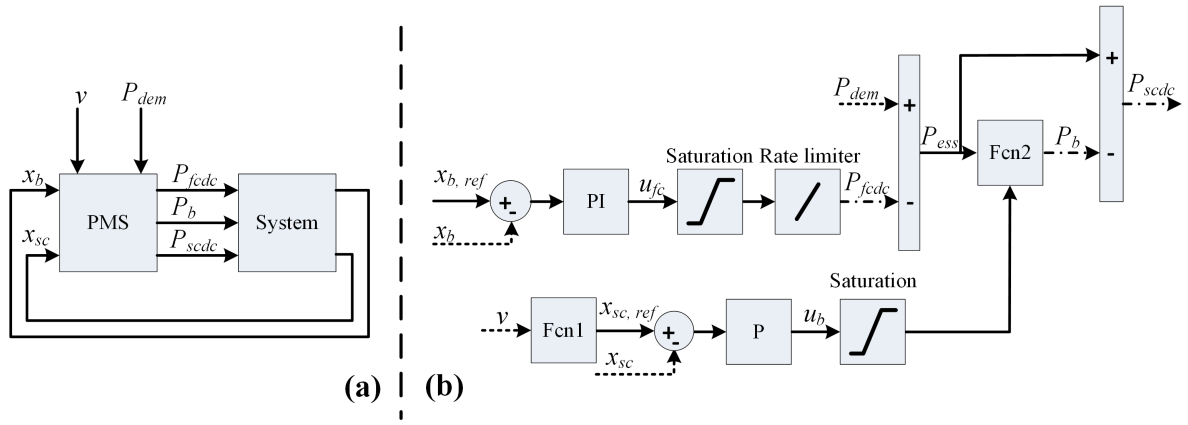

Figure 4.6: Schematic of the real-time power management strategy. (a) Position of the strategy as a controller of the system; (b) Detailed structure of the strategy.

state x_b around a constant reference, $x_{b,ref}$, of 0.6; thus,

$$u_{fc}(t) = K_{p,b}\left(x_{b,ref} - x_b(t)\right) + K_{i,b}\int_0^t \left(x_{b,ref} - x_b(\tau)\right)\mathrm{d}\tau. \tag{4.11}$$

The integral part of the controller guarantees a zero steady state error of the battery SOC. The controller output, u_{fc}, is limited by the FCS power rating, and its changing rate is limited to ± 1 kW/s before using it as a reference for the FCS converter. Having calculated the FCS power, the power required by the battery/supercapacitor hybrid ESS, P_{ess}, is determined as the difference $P_{dem} - P_{fcdc}$.

The distribution of P_{ess} among the battery and the supercapacitor is determined by a proportional controller of x_{sc} around a variable reference $x_{sc,ref}$. The controller output, u_b is given by:

$$u_b(t) = K_{p,sc}\left(x_{sc,ref}(t) - x_{sc}(t)\right), \tag{4.12}$$

and the speed-dependent reference is given by:

$$x_{sc,ref}(t) = x_{sc,ref}^{\max} - K_{ref,sc}\left(v(t)/v_{\max}\right)^2, \tag{4.13}$$

where $x_{sc,ref}$ varies linearly with the vehicle speed squared, $x_{sc,ref}^{\max}$ is the maximum reference corresponding to zero speed, $v_{\max}$ is the vehicle maximum speed of 80 km/h, and $K_{ref,sc}$ is the proportional factor. Equation (4.13) is represented in Figure 4.6(b) by the block named Fcn1. u_b represents the ratio of P_b to P_{ess}; or in other terms, the battery contribution in fulfilling P_{ess}. It is, therefore, bound within the range [-1, 1]. The battery power, P_b, is then calculated as:

$$P_b(t) = \begin{cases} +u_b(t)P_{ess}(t), & u_b(t) > 0 \,\&\, P_{ess}(t) > 0, \\ -u_b(t)P_{ess}(t), & u_b(t) < 0 \,\&\, P_{ess}(t) < 0, \\ 0, & \text{Otherwise}, \end{cases} \tag{4.14}$$

which is represented in Figure 4.6(b) by the block named Fcn2. If u_b is positive (i.e., x_{sc} is below the reference and the supercapacitor needs to be charged), the battery assists the supercapacitor in meeting the demand P_{ess} if it is positive; otherwise, the battery contribution is set to zero if P_{ess} is negative to allow charging the supercapacitor with

the maximum rate. On the other hand, if u_b is negative (i.e., x_{sc} is above the reference and the supercapacitor needs to be discharged), the battery assists the supercapacitor in meeting the demand P_{ess} if it is negative; otherwise, the battery contribution is set to zero if P_{ess} is positive to allow discharging the supercapacitor with the maximum rate.

It should be noted that this formulation of the real-time PMS does not allow a charge exchange between the battery and the supercapacitor. According to equation (4.14) and to the saturation of u_b, P_b lies always between 0 and P_{ess}, and P_{scdc} is the difference $P_{ess} - P_b$. Therefore, P_b and P_{scdc} have always the same sign. This feature of the real-time PMS distinguishes it from other strategies proposed in literature [49, 50], which are also based on PI controllers, however, with a charge exchange allowed between the battery and the supercapacitor. The advantages of this PMS formulations will be experimentally evaluated in Section 4.4.

The design of the PMS is reduced to the selection of controllers parameters, $K_{p,b}$, $K_{i,b}$, $K_{p,sc}$, $K_{ref,sc}$ and $x_{sc,ref}^{\max}$. The selection criteria are as follows: 1) The hydrogen consumption is minimized and, 2) the supercapacitor is responsible for most of the transient power so that the battery contribution is minimized.

For each driving cycle i, the first design index, J_1^i, is the percentage deviation of the hydrogen consumption, HC^i, from the off-line optimum, HC_{opt}^i, whereas the second index, J_2^i, is the average absolute battery power. Thus,

$$\begin{aligned} J_1^i &= \frac{HC^i - HC_{opt}^i}{HC_{opt}^i} \times 100\,(\%), \\ J_2^i &= \frac{1}{t_f^i} \int_0^{t_f^i} \left| P_b^i(t) \right| \mathrm{d}t. \end{aligned} \tag{4.15}$$

When the strategy is optimized over one driving cycle, the performance indices of equation (4.15) are the objectives to be minimized. Optimizing the strategy over several driving cycles is performed by averaging the performance indices of all driving cycles; i.e.,

$$\begin{aligned} J_1 &= \frac{1}{N_{dc}} \sum_{i=1}^{N_{dc}} J_1^i, \\ J_2 &= \frac{1}{N_{dc}} \sum_{i=1}^{N_{dc}} J_2^i, \end{aligned} \tag{4.16}$$

where N_{dc} is the number of driving cycles considered in the optimization. The resulting average indices, J_1 and J_2, constitute the objectives to be minimized. The same concept was used in Section 2.5 to account for several driving cycles in the optimization. Averaging the objective functions means that the same weight is given to all driving cycles in the optimization. For evaluation, the two driving cycles, Manhattan and NurembergR36, are here considered (i.e., $N_{dc} = 2$); however, the formulation can be used to account for any number of driving cycles.

Minimizing the two objectives leads to a multi-objective optimization problem with the controllers parameters as the optimization variables. The problem is solved by the multi-objective genetic algorithm explained in Appendix B.

It should be noted that evaluating the objective functions requires the system states at the beginning of the driving cycle to be the same as the states at the end of the driving cycle (i.e., charge sustaining performance). For a set of optimization variables to be tested by the optimization algorithm, the strategies are simulated over the driving cycle starting from initial states of 0.6 for the battery and 0.8 for the supercapacitor. If the final states are different from the initial states, the initial states are varied and the simulation is repeated until the charge sustenance is achieved, where the objective functions are then calculated. For most cases, the charge sustenance is obtained in the second simulation run if it is initiated by the final states of the first run.

The resulting Pareto front is shown in Figure 4.7. To verify the optimality of the Pareto solutions, random sets of the PMS parameters are tested and the results are shown in Figure 4.7, as well. The results indicate that there is a trade-off between the two objective functions. This trade-off is attributed to the fact that increasing the contribution of the battery decreases the contribution of the supercapacitor and, therefore, reduces the losses in the supercapacitor DC/DC converter.

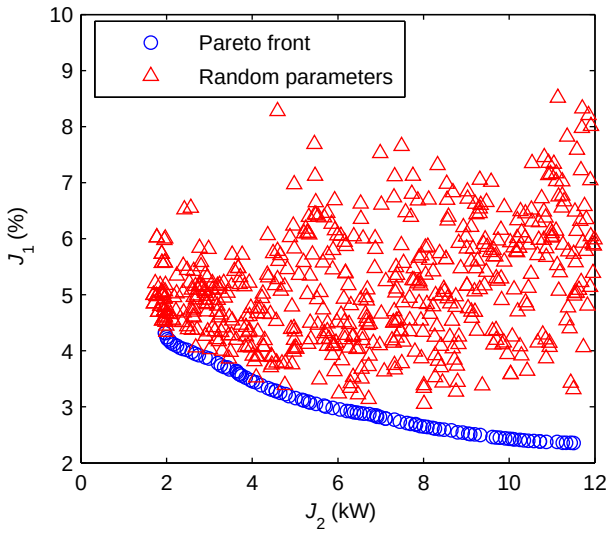

Figure 4.7: Optimization results of the real-time power management strategy.

All the solutions of the Pareto front are mathematically equally optimal. The choice among them requires weighing the relative importance of J_1 and J_2, and whether a certain battery contribution (i.e., J_2) is enough to assist the supercapacitor. To test the sufficiency of the battery contribution, the Pareto solutions are tested on the maximum acceleration performance between 0 and 60 km/h, which is achieved in about 11 s as shown in Figure 4.8. A speed over 60 km/h is rarely encountered in transit buses. The minimum J_2 that leads to x_{sc} >0.25 at the end of the acceleration phase is considered. Lower J_2 leads to an early depletion of the supercapacitor, so that the battery needs to deliver the whole ESS demand alone. As a result of this selection procedure, the Pareto solution that achieves J_2=2.5 kW is chosen, corresponding to J_1 of 4.0%.

Figure 4.8 shows the evaluation of the resulting PMS over the acceleration phase. At the end of the acceleration phase, the supercapacitor is almost depleted with a final state of 0.26 (remember that the minimum x_{sc} is 0.25). This means that J_2 of 2.5 kW is just sufficient to assist the supercapacitor even during harsh condition. J_2 may be increased if smaller supercapacitor is used.

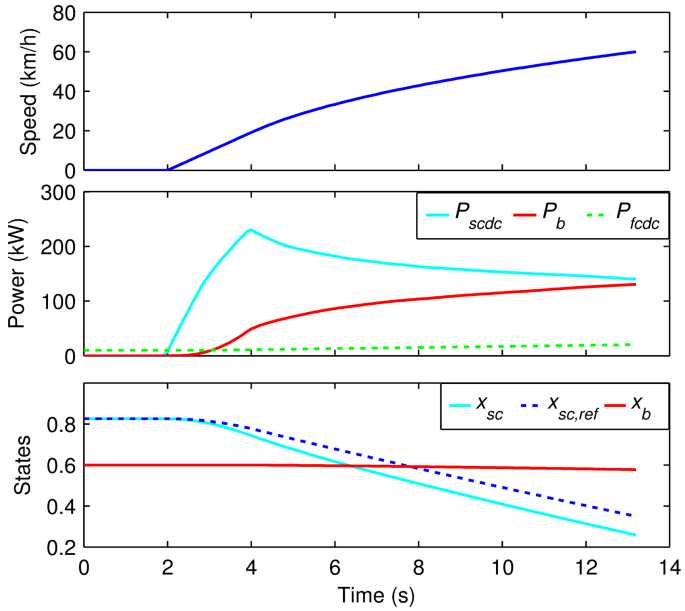

Figure 4.8: Evaluation of the real-time power management strategy over an acceleration 0-60 km/h.

Figures 4.9 and 4.10 show the evaluation of the PMS over Manhattan and NurembergR36. Here the battery controls the supercapacitor state around its variable reference, which is achieved by only small battery power in contrast to the aggressive conditions of Figure 4.8.

The increase of 4.0% (3.2% for Manhattan and 4.8% for NurembergR36) in hydrogen consumption of the real-time PMS in comparison to the off-line optimum is mainly attributed to the dramatic reduction in the power burden on the battery. For the off-line optimum, J_2=17.7 kW (16.7 kW for Manhattan and 18.7 kW for NurembergR36), whereas it is only 2.5 kW (1.8 kW for Manhattan and 3.2 kW for NurembergR36) for the real-time PMS, meaning a reduction of 85% in battery loading. As discussed at the end of Section 4.2, the off-line battery loading is very sensitive to the efficiency of supercapacitor DC/DC converter. The optimization problem was repeated with η_{scdc}=100%, and it was found that for J_2=2.5 kW of the real-time PMS, the real-time PMS achieves J_1=1.5%, since the off-line optimal battery loading is already small in this case.

4.4 Experimental Study

In this section, the optimization of the real-time PMS of an experimental fuel cell/ battery/ supercapacitor hybrid system is carried out following the methods developed in Section 4.3. The strategy of Figure 4.6 is adopted in the test bench, and its main advantageous features are illustrated by comparison with a conventional strategy. Manhattan driving cycle is used here for evaluation.

The layout and specifications of the test bench are given in Appendix C. The test bench is supposed to simulate the vehicle on a small scale. The hybrid power source of the vehicle has a maximum fuel cell power of 120 kW as given in Section 4.1. The net power of the test bench FCS is limited to 700 W. The ratio of test bench FCS power to the vehicle FCS power of 0.006 ($\approx$ 0.7 kW/120 kW) is used as a scaling factor between the vehicle

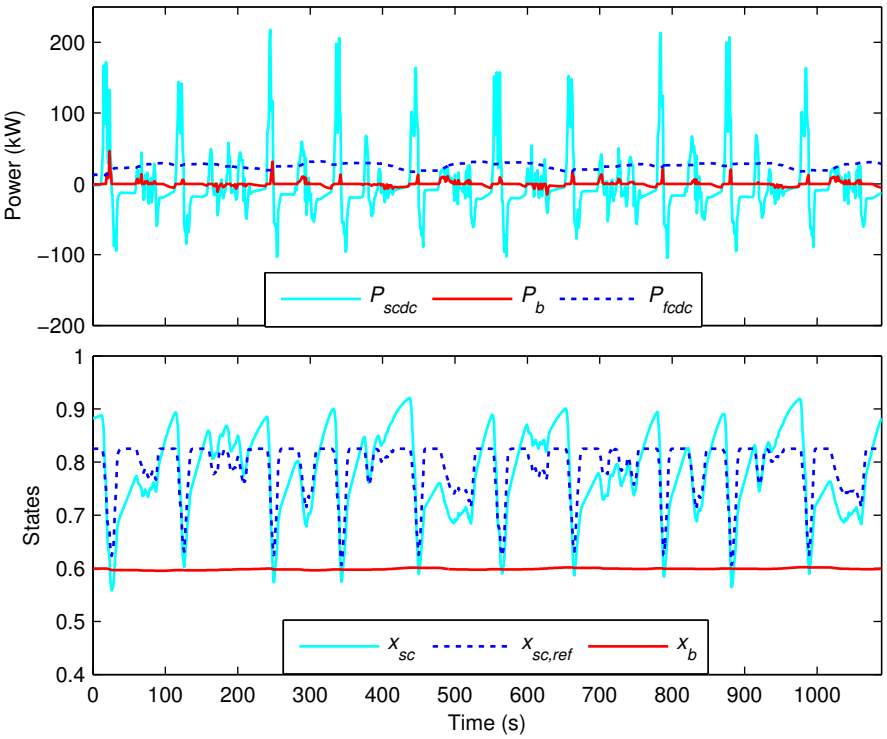

Figure 4.9: Evaluation results of the real-time power management strategy over Manhattan driving cycle.

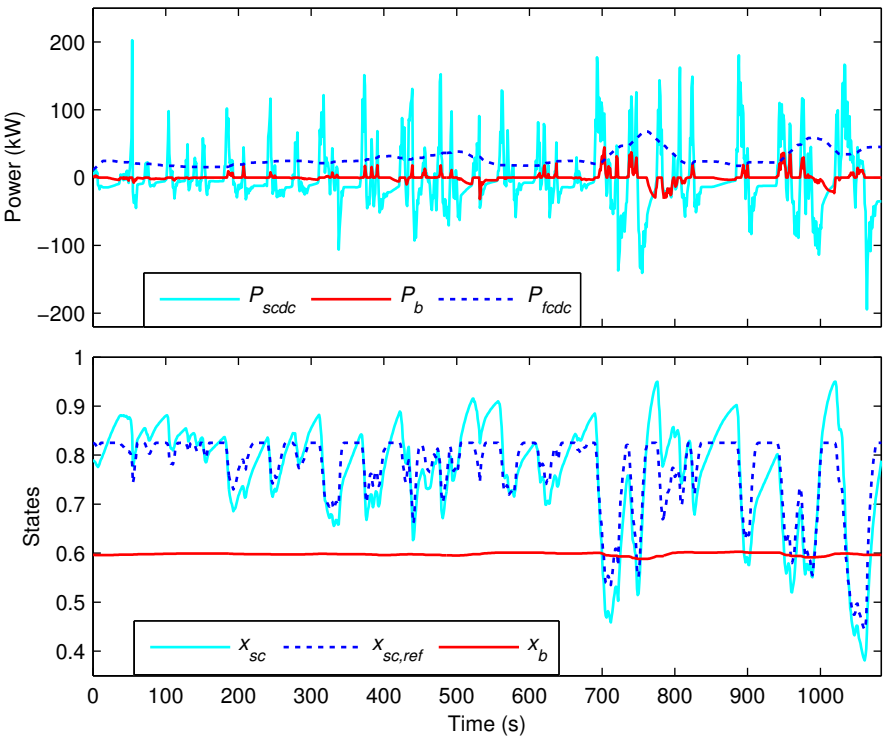

Figure 4.10: Evaluation results of the real-time power management strategy over Nurembergr36 driving cycle.

and the test bench, so that the vehicle power demand calculated by the vehicle model in Section 4.1 is multiplied by this scaling factor when it is applied to the test bench.

Using the same scaling factor to downscale the vehicle supercapacitor size of 0.97 kWh, the required test bench supercapacitor energy is then 5.8 Wh (=0.006 × 0.97 kWh). In comparison, the test bench supercapacitor used has an energy content of 54 Wh. Therefore, the test bench supercapacitor is actually oversized by a factor of about 10. As shown in Section 4.3, the size of the supercapacitor plays a crucial role in the design of the real-time strategy. Therefore, in order to mimic the conditions in the actual vehicle, only part of the available supercapacitor energy at the test bench is used. The nominal supercapacitor SOE will be 0.6, and the lower SOE limit is 0.53. A reduction of supercapacitor SOE of 0.07 in the test bench would correspond to a reduction of 0.7 in the vehicle representing a depletion of the vehicle supercapacitor.

Two strategies shown in Figure 4.11 are introduced and compared. The first strategy S1 shown in Figure 4.11(a) is used as a benchmark to illustrate the advantages of the second strategy S2 shown in Figure 4.11(b). Both strategies use the battery to regulate the supercapacitor state through a proportional controller (P), whereas the FCS is used to regulate the battery state with the help of a proportional-integral controller (PI).

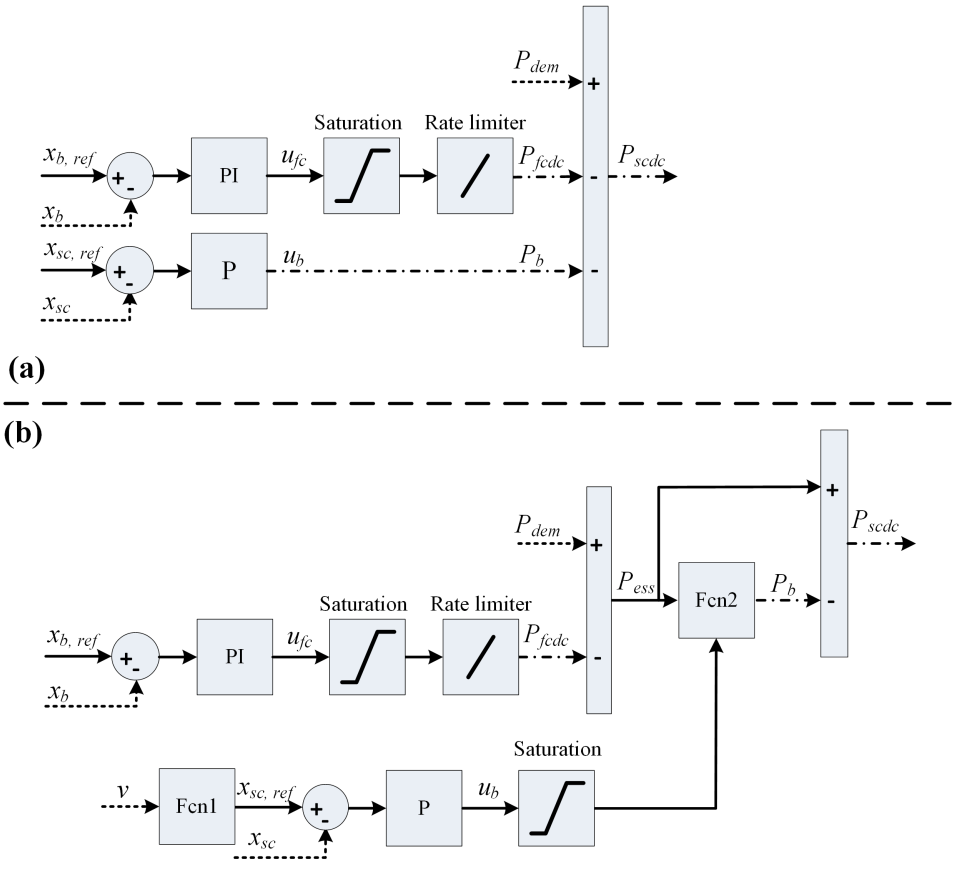

Figure 4.11: Schematic of the two power management strategies. (a) S1; (b) S2. The inputs represented by dotted arrows and the outputs by dash-dot arrows.

For S1, a PI controller is used to control the battery state around the constant reference $x_{b,ref}$ of 0.6; thus,

$$u_{fc}(t) = K_{p,b}\left(x_{b,ref} - x_b(t)\right) + K_{i,b}\int_0^t \left(x_{b,ref} - x_b(\tau)\right)\mathrm{d}\tau. \tag{4.17}$$

The output of the controller, u_{fc}, is then fed into a saturation block that limits the control variable between 0 and 700 W. The rate limiter limits the ramp rate of the control variable to ± 10 W/s. The output of the rate limiter is used as a reference power for the FCS DC/DC converter.

The proportional controller, shown below, controls the supercapacitor state around a constant reference $x_{sc,ref}$ of 0.6, where the battery power P_b equals the output of the controller, u_b, given by:

$$u_b(t) = K_{p,sc}\left(x_{sc,ref} - x_{sc}(t)\right). \tag{4.18}$$

Then the difference $P_{dem} - P_{fcdc} - P_b$ constitutes the reference power for the supercapacitor DC/DC converter.

The control loop of x_b in S2 is the same as S1, whereas the control loop of x_{sc} is different. The strategy S2 is the same used in Section 4.3; however, the maximum reference supercapacitor state $x_{sc,ref}^{\max}$ is made here constant of 0.6.

As discussed in Section 4.3, the charge exchange between the battery and supercapacitor is not possible in S2, whereas such exchange is possible in S1, for example, if $x_{sc} < x_{sc,ref}$ (i.e., $P_b > 0$) and $P_{dem} - P_{fcdc} < 0$.

In summary, S2 has three main features that distinguish it from S1. First, in S2, the supercapacitor reference state is made variable with the speed, whereas this reference is constant in S1. Second, the charge exchange between the battery and supercapacitor is excluded in S2, whereas such exchange is possible in S1. Third, P_b in S2 takes into account, in addition to the difference $x_{sc,ref} - x_{sc}$, P_{ess} (and hence P_{dem}), whereas in S1, P_b considers only the difference $x_{sc,ref} - x_{sc}$.

The design of the power management strategy is reduced to the selection of controllers parameters, $K_{p,sc}$, $K_{p,b}$ and $K_{i,b}$ for S1, and $K_{p,sc}$, $K_{p,b}$ and $K_{i,b}$ in addition to $K_{ref,sc}$ for S2. The selection criteria are as follows: 1) The hydrogen consumption is minimized, and 2) the supercapacitor is responsible for most of the transient power so that the battery contribution is minimized.

The first design objective function, J_1, is the total hydrogen consumption over the driving cycle, whereas the second objective, J_2, is the average absolute power of the battery; thus,

$$\begin{aligned} J_1 &= \int_0^{t_f} \dot{m}_h\left(P_{fcdc}(t)\right) \mathrm{d}t, \\ J_2 &= \frac{1}{t_f}\int_0^{t_f} \left|P_b(t)\right| \mathrm{d}t. \end{aligned} \tag{4.19}$$

The resulting Pareto fronts of the two strategies, S1 and S2, are shown in Figure 4.12(a). S2 achieves lower hydrogen consumption than S1 at the same battery contribution. This is a direct result of the fact that there is no charge exchange between the battery and the supercapacitor for S2, whereas such exchange exists for S1. Such charge exchange is accompanied by losses in the battery, the supercapacitor and mainly in the supercapacitor DC/DC converter. This becomes clearer if the average absolute supercapacitor contribution, J_3, defined as:

$$J_3 = \frac{1}{t_f}\int_0^{t_f} \left|P_{scdc}(t)\right| \mathrm{d}t,$$

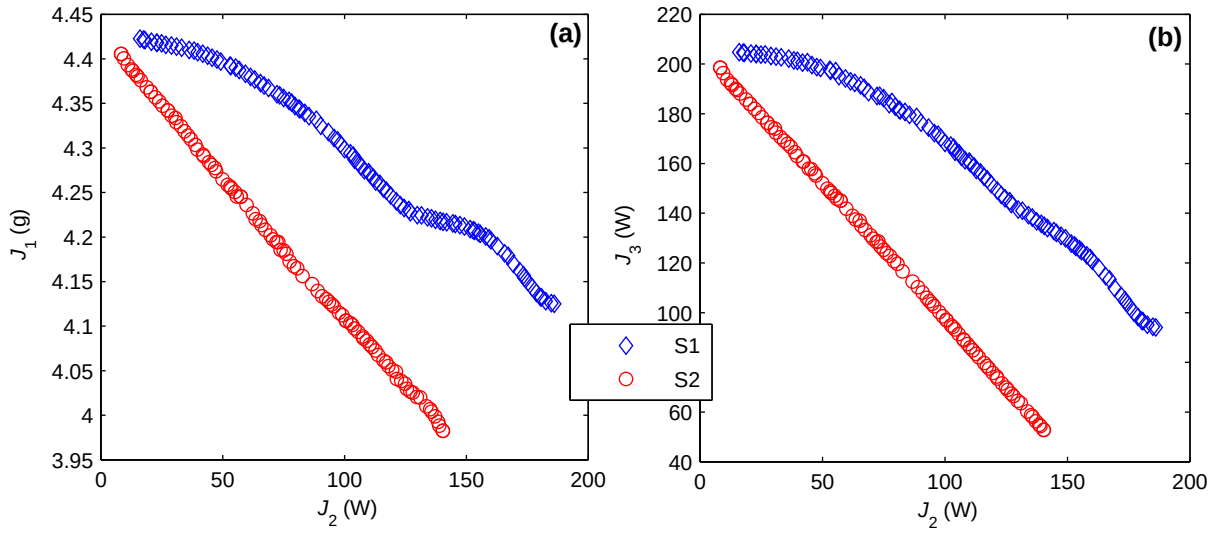

Figure 4.12: Optimization results of the power management strategies over Manhattan driving cycle. (a) Pareto front of J_1 and J_2; (b) J_3 versus J_2 for the Pareto solutions.

is considered. The relation between J_3 and J_2 for the two strategies is depicted in Figure 4.12(b) for the Pareto solutions of Figure 4.12(a). J_3 decreases linearly with J_2 for S2, whereas the relation is more complex for S1. In summary, for the same J_2, in comparison to S1, S2 achieves a smaller J_3, and this reduction in J_3 causes less energy loss in the supercapacitor DC/DC converter resulting in overall lower hydrogen consumption. The difference between the two strategies is smaller at smaller battery contribution, since at such low battery contribution, the charge exchange between the battery and the supercapacitor in S1 is also smaller. The difference between the two strategies increases with decreasing the efficiency of the supercapacitor DC/DC converter.

All the solutions of the Pareto front are mathematically equally optimal. The choice among them requires weighing the relative importance of J_1 and J_2, and testing whether a certain battery contribution (i.e., J_2) is enough to assist the supercapacitor. Here we put a major importance on J_2, so that advantage of using the supercapacitor is fully exploited. Hence, the Pareto solution that achieves the minimum enough battery contribution is considered. To test the sufficiency of a certain J_2, the Pareto solutions are evaluated on a strong acceleration 0-60 km/h shown in Figure 4.8. The Pareto solutions are tested in the direction of increasing J_2, and the minimum that achieves a final x_{sc} larger than 0.53 (starting from 0.6) is considered where 0.53 is considered as the lower limit for x_{sc}.

The above selection procedure is illustrated in Figure 4.13, which shows the evaluation of strategy S1 over the acceleration phase for three Pareto solutions (corresponding to J_2=20, 71 and 120 W). For J_2 of 20 W, the battery contribution is very small at the initial stages of the acceleration, whereas the supercapacitor is strongly loaded, so that the supercapacitor SOE reaches its lower limit of 0.53 before completing the acceleration. After about 8 seconds of acceleration, the battery needs to deliver the required power alone. If the battery is not capable of providing the required power, the acceleration time is prolonged. Therefore, a J_2 of 20 W is considered "insufficient." On the contrary, for J_2 of 120 W, the battery contribution is relatively high from the beginning of acceleration, so that the supercapacitor is less loaded and its final SOE is 0.55. This case is denoted

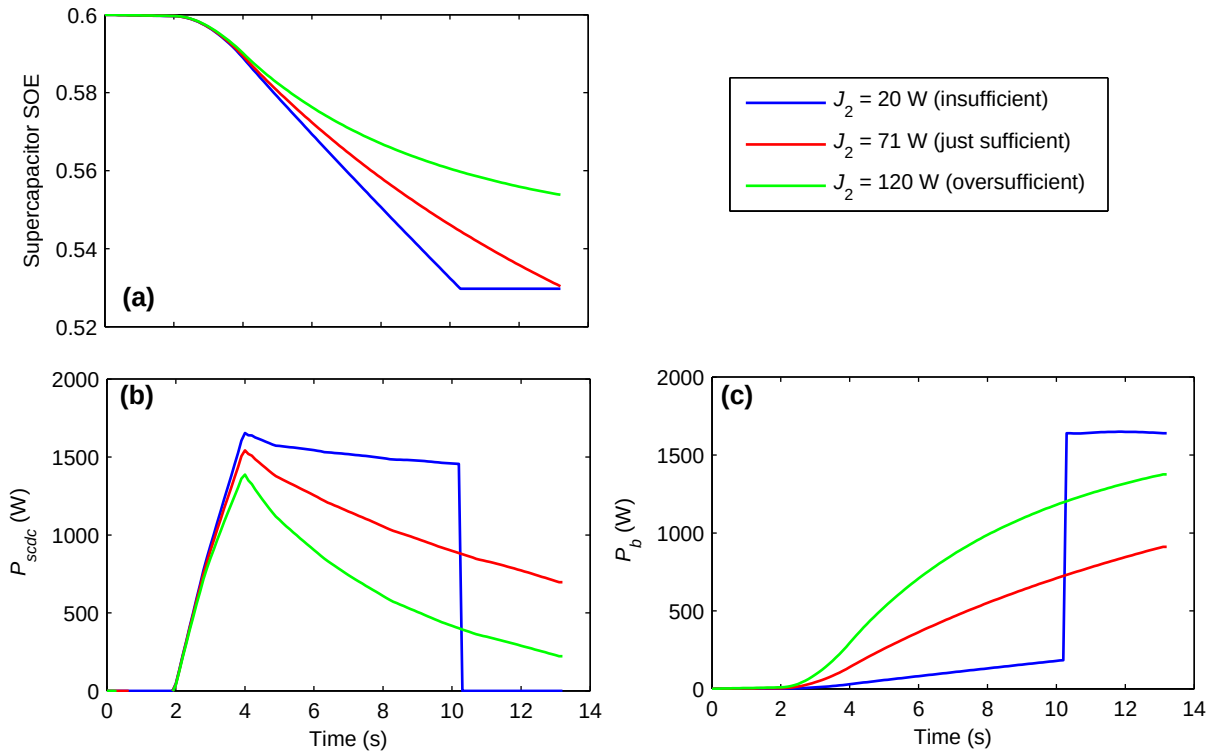

Figure 4.13: Evaluation of three Pareto solutions with three values of J_2 for the strategy S1. (a) Supercapacitor SOE; (b) Supercapacitor power; (c) Battery power.

in Figure 4.13 as "oversufficient." The value J_2 of 71 W represents the border between the last cases, where the supercapacitor survives the acceleration phase and ends up at its minimum SOE at the end of acceleration. This case is denoted in Figure 4.13 as "just sufficient," and it is considered as a design point for the strategy S1. In conclusion, the value of J_2 plays a role of a tuning parameter for the strategy, which can be tailored according to the design preferences and system specifications. For example, a small supercapacitor requires higher J_2 (i.e., higher battery contribution), whereas large supercapacitor requires less battery contribution.

As a result of the aforementioned parameters selection procedure, it has been found that the minimum J_2 required is 71 W for S1 and only 7 W for S2. This means that S2 achieves the same performance during the strong acceleration while having 90% lower battery loading during the normal driving cycles. The two strategies with the chosen parameters are subsequently experimentally evaluated.

Figure 4.14 shows the experimental evaluation of the strategies over the acceleration phase. The supercapacitor ends up at a final state of 0.53, which is the value used to select the strategies parameters. The total energy supplied by the battery during the acceleration is the same in both strategies (about 15 Wh). However, The battery power increases faster in S2 at the initial stages of the acceleration (e.g., at time 4 s, the battery power is 220 W for S2 and 130 W for S1), because the battery power in S2 is also dependent on the power demand, not only the current supercapacitor state. The demand increases fast at the beginning of acceleration, and so does the battery power in S2. In contrast, the battery power in S1 depends solely on the supercapacitor state and, therefore, it increases relatively slowly at the beginning. Since the consumed battery

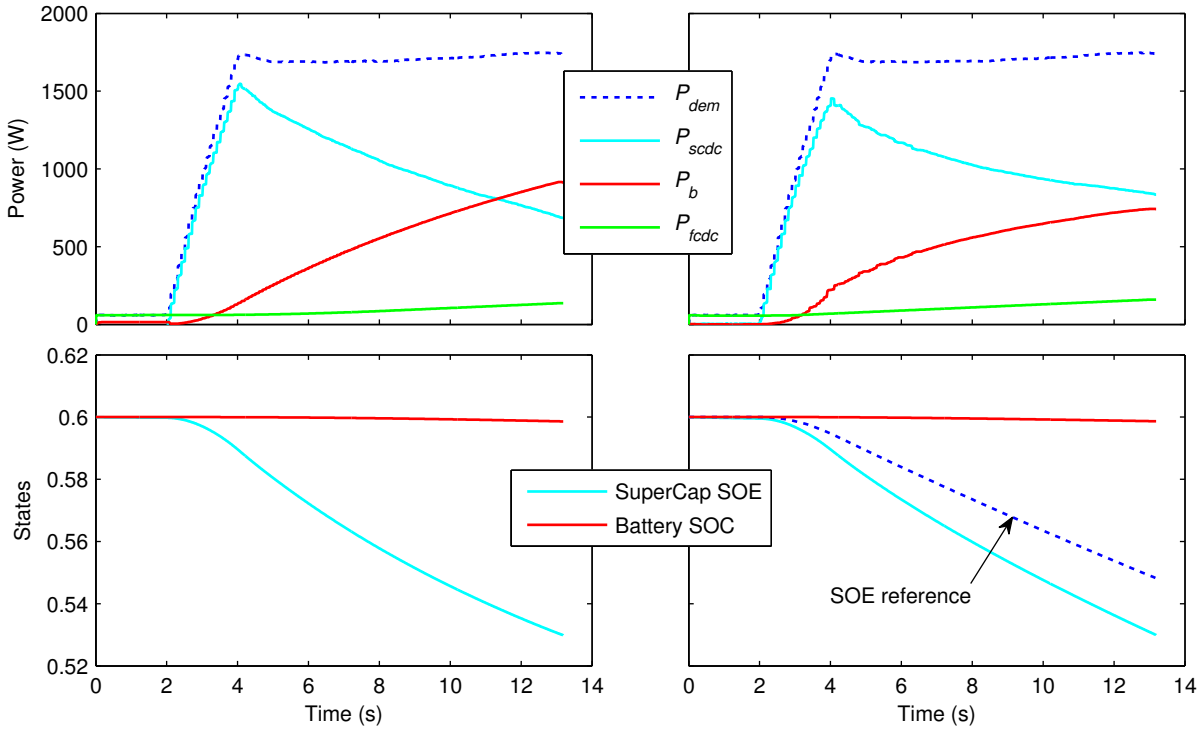

Figure 4.14: Experimental power distribution and states trajectories during the acceleration phase with S1 (left) and S2 (right).

energy is the same in both strategies, the maximum required battery power is smaller for S2 in comparison to S1 (e.g., 915 W for S1 and 743 W for S2 at the end of the acceleration).

In order to experimentally validate the objective functions, J_1 and J_2, the two strategies S1 and S2 are evaluated over Manhattan driving cycle as shown in Figures 4.15 and 4.16, respectively, for a charge sustaining performance. The test bench replicates the simulation results very well as illustrated in the comparison between simulation and experiment in terms of states trajectories. The second observation is that S2 requires negligible battery contribution in comparison to S1. Table 4.3 quantitatively compares the simulation and experiment in terms of the performance metrics J_1 and J_2.

As a result of the experimental evaluation, S2 excels S1 since it achieves a dramatic reduction of the battery loading (about 90% lower in comparison to S1) during normal driving cycles while performing equally well in terms of supercapacitor assistance during strong acceleration phases and in terms of hydrogen consumption (only about 1% higher than S1).

Table 4.3: Comparison between simulation and experiment in terms of the performance indices J_1 and J_2. sim.=simulation, exp.=experiment.

Strategy	J_2(W) (sim. / exp.)	J_1(g) (sim. / exp.)
S1	71 / 73	4.36 / 4.42
S2	7 / 8	4.41 / 4.45

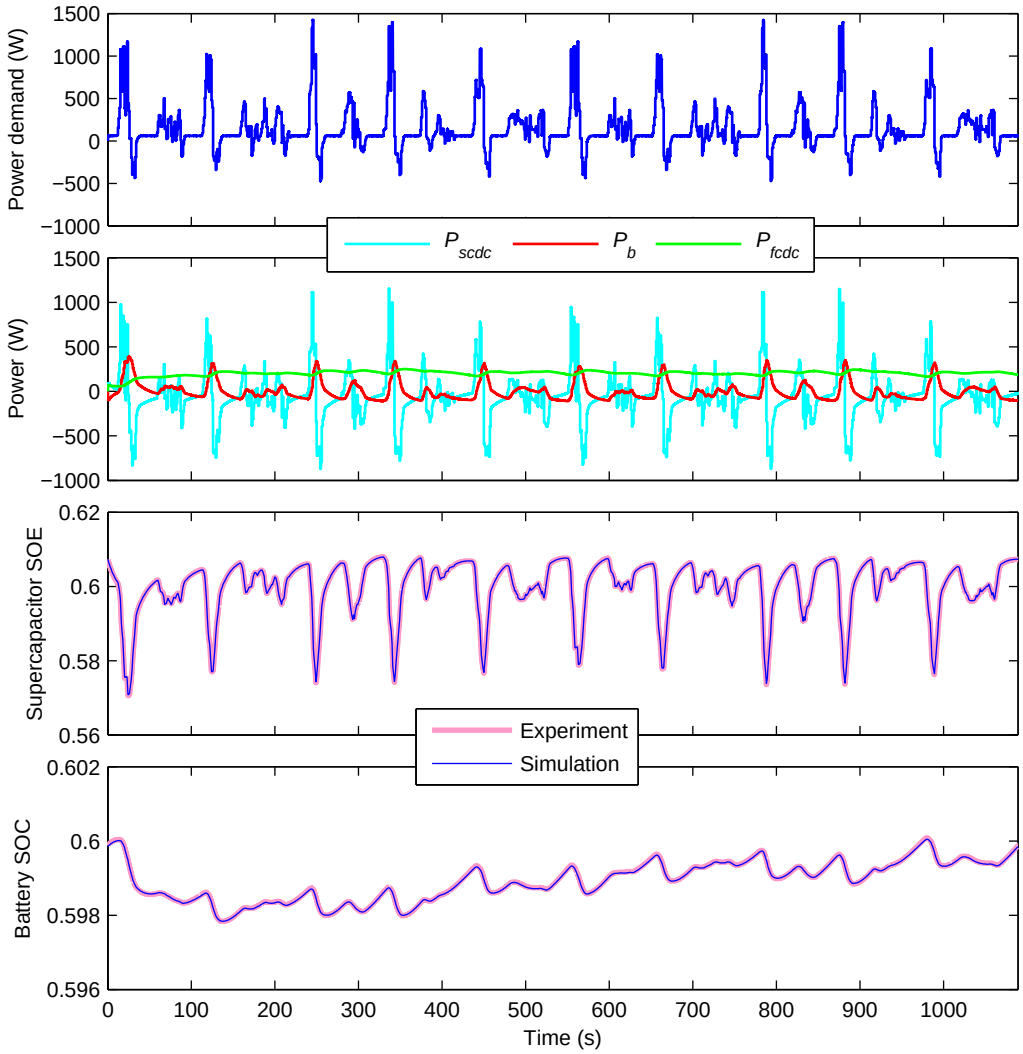

Figure 4.15: Experimental evaluation of the power management strategy S1 over Manhattan driving cycle.

The detailed analysis of the power flow in the triple hybrid system considered is quite complex, where every power source exchanges power with the other two sources and with the load. However, the main characteristics of the system behavior can be analyzed by grouping two sources and/or considering two sources at a time. Considering the battery/supercapacitor as a hybrid energy storage system, ESS, with a power $P_{ess} = P_{dem} - P_{fcdc}$, three main modes of operation can be recognized over Manhattan driving cycle for both strategies:

- $P_{dem}>0$ and $P_{fcdc}< P_{dem}$ ($P_{ess} >0$): both FCS and ESS provide the demand.
- $P_{dem}>0$ and $P_{fcdc}> P_{dem}$ ($P_{ess} <0$): FCS provides the whole demand and charges the ESS.
- $P_{dem}<0$ (i.e., regenerative braking) ($P_{ess} <0$): both FCS and load charge the ESS.

The power P_{ess} represents the net power of the hybrid ESS; therefore, the power exchanged between the battery and the supercapacitor does not appear in P_{ess}. Having

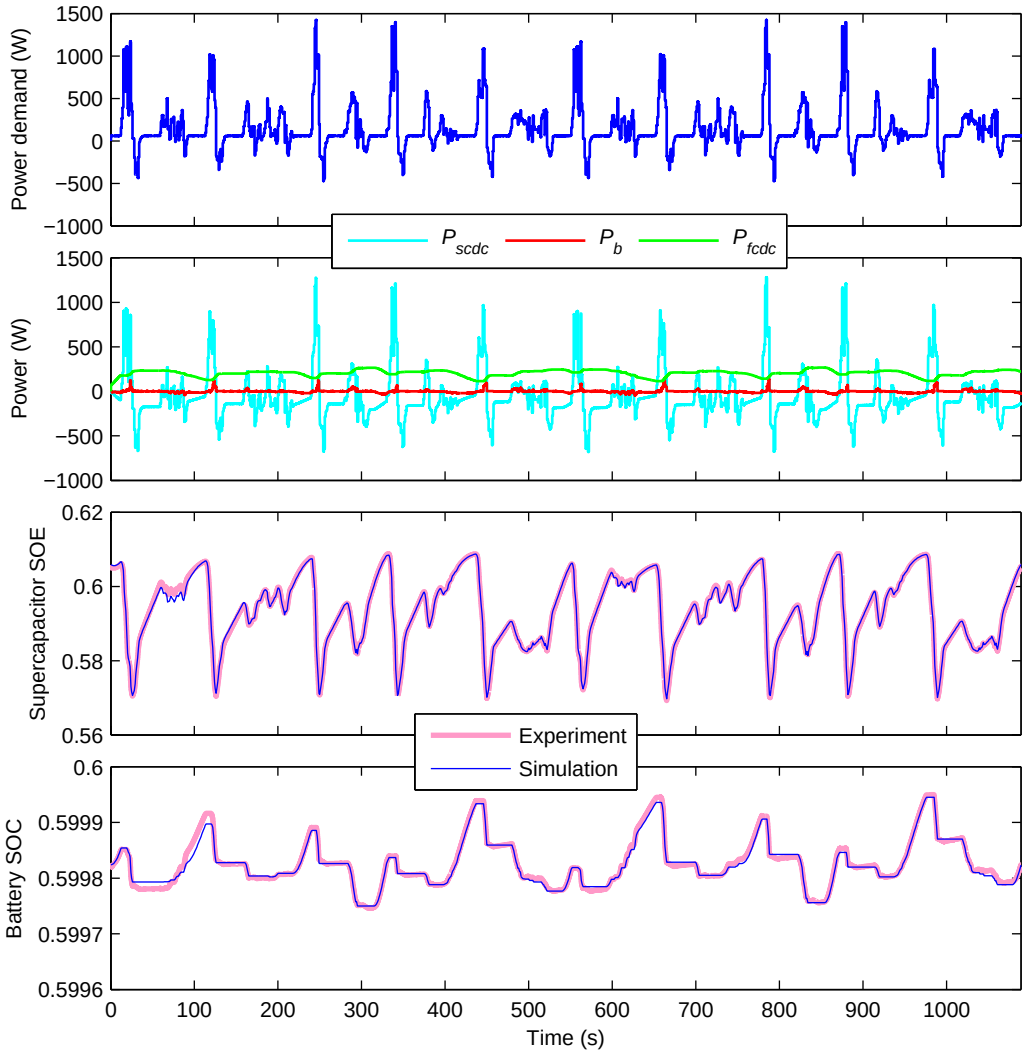

Figure 4.16: Experimental evaluation of the power management strategy S2 over Manhattan driving cycle.

such power exchange means that one of the two ESS components charges the other. Obtaining information about this power exchange requires looking at the power profile of one ESS component, battery or supercapacitor. The battery power P_b can be divided into two terms: one term represents the contribution of battery to P_{ess} and the other term represents the battery power fed to the supercapacitor. If the second term is positive, the battery is charging the supercapacitor; otherwise, the supercapacitor is charging the battery. Figure 4.17 illustrates the analysis of battery power over the time 400–600 s of Manhattan driving cycle for the two strategies. The figure shows the total battery power and its part directed to the supercapacitor. The difference between the two curves represents the battery contribution to P_{ess}. For S1, a significant part of the battery contribution is due to the power exchange with the supercapacitor, and the power exchange happens in the two directions; i.e., the battery can charge the supercapacitor and the supercapacitor can charge the battery. As stated earlier, S2 is designed so that the power exchange within the hybrid ESS is prevented, which is illustrated in Figure 4.17(b). There are some traces of power exchange (less than 5 W) in Figure 4.17(b) due to measurement errors. In summary, for S2, the battery never charges the supercapacitor and the supercapacitor never charges the battery.

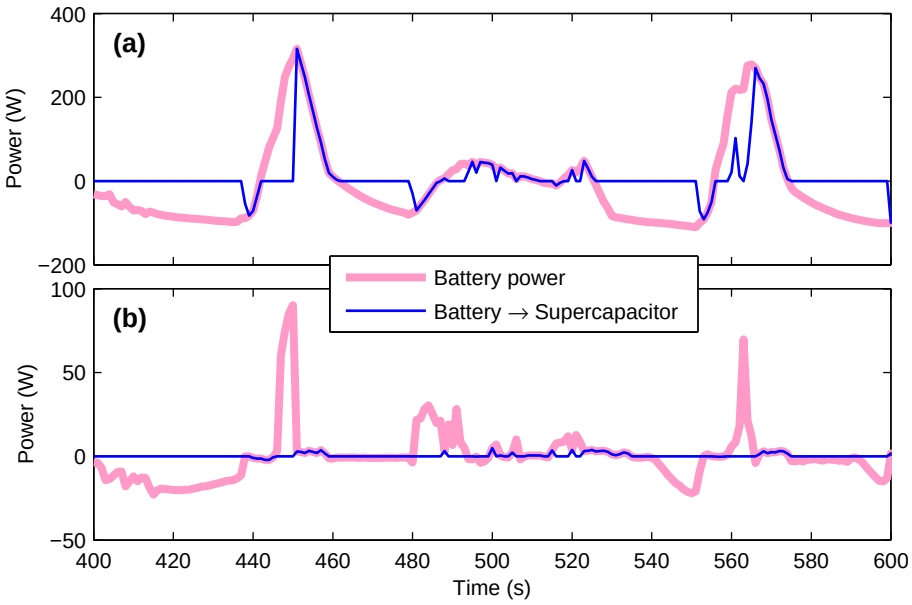

Figure 4.17: Experimental battery power and its part exchanged with the supercapacitor. (a) S1; (b) S2.

4.5 Conclusions

This chapter was intended to form a comprehensive framework for the optimization of the power management strategy of fuel cell/battery/supercapacitor hybrid systems for transit bus applications. DP and PMP were used and their results were compared. The algorithm used for a single ESS to account for state boundary constraints in PMP was extended to account for the case of hybrid ESS, composed of battery and supercapacitor.

Apart from not being real-time capable, the off-line optimum takes only the hydrogen consumption into account, which resulted in unacceptable performance in terms of battery power loading. This issue was taken into account in the design and optimization of the real-time PMS, which was optimized by a genetic algorithm and Pareto front analysis while considering hydrogen consumption, battery power and vehicle acceleration performance. The resulted real-time PMS consumed few percent more hydrogen than the off-line optimum (depending on the supercapacitor DC/DC converter efficiency), however, with a dramatic improvement in the system durability.

The real-time PMS optimization was repeated for a small-scale experimental fuel cell/ battery/ supercapacitor hybrid system. The experimental measurements replicated the simulation results very well, thanks to the good models of the test bench components. By comparing the proposed real-time PMS with comparable strategies in literature, two main advantageous features of the PMS were identified. First, the charge exchange between the battery and the supercapacitor should be avoided and, second, the battery power should take the power demand into account in addition to the supercapacitor state. These two features resulted in excellent performance in terms of battery loading, hydrogen consumption and acceleration.

Chapter 5

Summary and Perspectives

This thesis was intended to provide a comprehensive framework for the optimization of fuel cell-based hybrid vehicles for different ESS options, namely, battery, supercapacitor or battery/supercapacitor. The optimization of the PMS was investigated for the three topologies, and the optimization of the powertrain size was investigated for a single ESS, battery or supercapacitor.

PMS design and optimization

For a fuel cell/battery hybrid system, the PMS optimization was first performed assuming a complete knowledge of the driving cycle, resulting in an off-line optimal strategy that globally minimizes the hydrogen consumption. DP and PMP were compared as two possible off-line optimization techniques. Special consideration was given to the inclusion of battery SOC boundary constraints in the formulation of PMP. The off-line optimal strategy is not real-time capable; hence, real-time capable strategies were designed and optimized while using the off-line optimal PMS as a benchmark. The optimization of the real-time PMS was formulated as multi-objective optimization problem, solved by a multi-objective genetic algorithm, taking into account hydrogen consumption and charge sustenance as two optimization objectives. Special emphasize is put on the inclusion of multiple driving cycles, of different nature, in the optimization to increase the strategy robustness. The off-line and real-time PMS optimization was validated on a small-scale experimental fuel cell/battery hybrid system.

Fuel cell/supercapacitor hybrid powertrains were also investigated in terms of PMS design and optimization using the same methods used for fuel cell/battery hybrids. The optimization methods were validated on a small-scale experimental fuel cell/supercapacitor hybrid system. For the experimental system, several methods were discussed to include the FCS power gradient limitation in the off-line PMS optimization, and the effect of such limitation on hydrogen consumption was analyzed.

The most complex hybrid system fuel cell/battery/supercapacitor was also investigated in terms of PMS optimization, where DP and PMP were first applied and compared. The algorithm used for a single ESS to account for state boundary constraints in PMP was extended to account for this special case where two ESSs exist. Apart from not being real-time capable, the off-line optimum takes only the hydrogen consumption into account,

which resulted in unacceptable performance in terms of battery power loading. A real-time strategy was proposed and optimized taking into account hydrogen consumption, battery power and vehicle acceleration performance in a framework of multi-objective optimization. The proposed real-time PMS and its optimization were validated on a small-scale experimental fuel cell/battery/supercapacitor hybrid system.

As a result of PMS design and optimization techniques explored, the following conclusions can be drawn:

- The comparison between PMP and DP reveals that both algorithms achieve the global optimal PMS, whereas PMP has the advantage of negligible required computation resources (i.e., time and memory);
- In terms of programming effort, DP is simpler and more straightforward than PMP. PMP requires non-trivial manipulations to deal with constraints such as the battery SOC boundary constraints. This issue is further intensified for hybrid ESS composed of battery and supercapacitor. Additionally, PMP may encounter a difficulty in convergence when the FCS power gradient is constrained;
- Even though both algorithms, DP and PMP, require the whole driving cycle to be known a priori, making them not real-time capable, a real-time capable strategy can be easily deduced from PMP with proper adaptation of the co-state;
- The real-time PMS can be optimized simultaneously over many driving cycles increasing its robustness;
- The off-line optimization that takes only hydrogen consumption as an objective to minimize does not always result in an acceptable performance. For example, minimizing the hydrogen consumption may result in high FCS dynamics and, therefore, FCS dynamics should be considered in the optimization problem. Another example is the fuel cell/battery/supercapacitor hybrid, where the off-line optimization resulted in high battery power, not fully exploiting the advantage of using the supercapacitor besides the battery.

As for the PMS design and optimization, future research topics may address the following issues:

- Most recent off-line optimization algorithms, such as convex optimization, can be included in the list of possible off-line optimization algorithms. Recent literature on convex optimization shows promising results. However, this approach requires approximations of the FCS model and ESS model. It would be interesting to assess the effect of such approximations on the global optimality of the off-line PMS;
- In this study, the minimum number of system states is considered, namely, the ESS charge level and the FCS power if its gradient is constrained. More states can be added such as the temperature of battery and FCS. The temperature may have a significant effect on the battery resistance, and the FCS temperature may have an effect on its efficiency. This would require a thermal model of the FCS and battery;

- The inclusion of FCS lifetime and battery lifetime in the PMS optimization was briefly addressed; where the limitation of FCS power gradient was discussed, and the battery aging was quantified by an Ampere-hour throughput model. The inclusion of more sophisticated FCS aging model and battery aging model is of interest.
- The new technology of eco-driving systems has emerged over the last few years, and is currently a hot research topic with its significant potential to improve the vehicle fuel economy. The target of these systems is to adopt an energy-aware driving style, either by giving advices to the driver or even by directly controlling the vehicle. Eco-driving systems can make use of the navigation system and the vehicle communication to its surrounding; i.e., Vehicle-to-Vehicle (V2V) and Vehicle-to-Infrastructure (V2I) communication, in order to calculate the most efficient speed trajectory. The adoption of optimization-based eco-driving systems in hybrid vehicles would be the most challenging in comparison to conventional vehicles or electric vehicles due the increased dimension of the optimization problem, where the speed trajectory and the power management should be optimized in a reasonable time.

Powertrain sizing

The sizing of the power sources of fuel cell/battery and fuel cell/supercapacitor hybrids took into account hydrogen consumption and cost as two objectives. The sizing process was approached by two nested loops. The outer loop iterates over all the possible designs (FCS size and ESS size), and for each design the objective functions are evaluated within the inner loop that represents the optimization of the PMS by PMP. The interesting designs (i.e., Pareto front), which represent the most efficient trade-off between the objectives, were then extracted. The effect of battery lifetime on the sizing process was investigated by using an Ampere-hour throughput model to quantify the battery aging.

The main conclusions of the sizing process are:

- The cost of the powertrain needs to be considered as an objective besides hydrogen consumption; otherwise, the optimization may result in a too costly powertrain. A good compromise can be found that significantly reduces the cost with a marginal effect on the hydrogen consumption;
- Considering only the Pareto front, representing the best trade-off between cost and hydrogen consumption, simplifies the task of decision-making in choosing the right powertrain size;
- Considering the battery aging leads to less efficient powertrain designs. In comparison to battery replacement, it is more economical to sacrifice some hydrogen consumption in order to reduce the stress on the battery so that it survives the vehicle lifetime;
- The supercapacitor as an ESS is less economical than the battery. It can be more economical in comparison to batteries with short cycle life.

As for the optimization of powertrain size, future research topics may address the following issues:

- A simple Ah-throughout model is used here to express the battery aging, where the Ah-throughput is considered as the only stress factor. It would be interesting to use more sophisticated models that consider other stress factors such as the temperature, depth-of-discharge and discharge-charge rate;

- In this study, the aging of fuel cell systems is not included. It is of interest to study the effect of FCS aging, besides the battery aging, on the optimal powertrain size;

- In this study, the sizing process possesses two dimensions: the FCS size and the ESS size. More dimensions can be considered such as the size of the traction motor and the gear ratio of the transmission line. For 2-D sizing, an exhaustive search for the most efficient powertrain size can be the best option. However, increasing the problem dimensions would exponentially increase the number of powertrain designs to be evaluated, making the evolutionary algorithms a more time-wise feasible option;

- In this study, the powertrain sizing was addressed for a single ESS, either battery or supercapacitor. The next step is to investigate the sizing of the triple hybrid system fuel cell/battery/supercapacitor;

- In this study, fixed costs for the FCS, the Li-ion battery, the supercapacitor and hydrogen are considered. These technologies, for vehicular applications, are relatively new and produced in relatively small quantities; therefore, the characteristics of these technologies and their costs may change significantly in the near future. It would be of interest to investigate the influence of different future scenarios on the powertrain sizing.

Appendix A

Bases of the Off-line Optimization Techniques

In this appendix the basic principles and derivation of the off-line optimization techniques, Dynamic Programming (Section A.1) and Pontryagin's Minimum Principle (Section A.2), are given. The discussion here is based on the textbooks [25, 89].

A.1 Dynamic Programming (DP)

The dynamic programming algorithm is based on the Bellman's Principle of Optimality, which says:

> *An optimal policy has the property that whatever the initial state and initial decision are, the remaining decisions must constitute an optimal policy with regard to the state resulting from the first decision.*

The proof of this principle is illustrated in Figure A.1(a). Suppose that **a**–**b**–**c**–**e** is the optimal state trajectory between an initial state **a** and a final state **e**. Then the minimum cost to move from **a** to **e** is:

$$J^*_{ae} = J_{ab} + J_{bc} + J_{ce}.$$

ASSERTION: if **a-b-c-e** is the optimal trajectory between **a** and **e**, then **b**–**c**–**e** is the optimal trajectory between **b** and **e**.

Proof: This can be proven by contradiction. Suppose that **b**–**d**–**e** is the optimal path between **b** and **e**. This would imply that the cost of the path **b**–**d**–**e** is smaller than the cost of the path **b**–**c**–**e**; i.e.,

$$\begin{aligned} J_{bd} + J_{de} &< J_{bc} + J_{ce}, \\ \Rightarrow J_{ab} + J_{bd} + J_{de} &< J_{ab} + J_{bc} + J_{ce} = J^*_{ae}, \end{aligned}$$

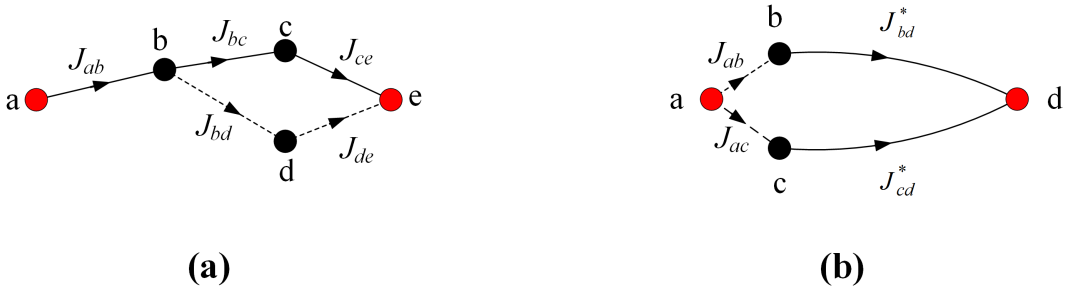

Figure A.1: Principle of the Dynamic Programming algorithm. (a) Illustration of the principle of optimality; (b) Application of the principle of optimality to find the optimal trajectory for a multi-stage process.

which violates the condition that **a**–**b**–**c**–**e** is the optimal trajectory. Thus, the assertion is proven.

Application: Let us have the multistage optimization problem illustrated in Figure A.1(b). The task is to find the optimal path from **a** to **d**. Assume as well that the problem has been partly solved and the optimal segments **b**–**d** and **c**–**a** have been calculated with the corresponding minimum costs J^*_{bd} and J^*_{ca}, respectively. The remaining task is to decide which decision to make at the initial stage, **a**–**b** or **a**–**c**, in order to get the optimal path between **a** and **d**. The principle of optimality implies that if **a**–**b** is the initial segment of the optimal path from **a** to **d**, then the optimal segment **b**–**d** is the terminal segment of this optimal path. Likewise, if **a**–**c** is the initial segment of the optimal path from **a** to **d**, then the optimal segment **c-d** is the terminal segment of this optimal path. Therefore, in order to evaluate the two possible initial decisions, we need to compare the two costs:

$$\begin{aligned} J_{abd} &= J_{ab} + J^*_{bd}, \\ J_{acd} &= J_{ac} + J^*_{cd}. \end{aligned}$$

The minimum cost determines the optimal decision at the initial stage. In other words, there may be other suboptimal segments from **b** to **d** and from **c** to **d**. The principle of optimality states that only the optimal segments and their optimal costs need to be known in order to find the optimal decision at stage **a**. To find the optimal decision at each stage, what we need to know, is only the optimal cost at the subsequent stages and the cost to move to those subsequent stages.

A.2 Pontryagin's Minimum Principle (PMP)

PMP uses the calculus of variations to determine the necessary optimality conditions of a dynamic system. Let the system be defined by the dynamic equation:

$$\dot{x} = f(x, u, t),$$

and the task is to find the optimal control $u^*(t)$ that minimizes the cost function:

$$J = \int_0^{t_f} L(x, u, t)\mathrm{d}t,$$

between 0 and t_f. There are many formulations of PMP depending on the boundary conditions of the optimization problem. Here only the relevant case is discussed where the initial state, $x(0)$, the terminal state, $x(t_f)$, and the terminal time, t_f, are all fixed. For simplicity, as well, a single state is assumed.

According to the Lagrange multiplier method, considering the system constraint is done by introducing the Lagrange multiplier, λ, to form the augmented cost function[1]

$$J_a = \int_0^{t_f} \left[L(x,u,t) - \lambda\left(f(x,u,t) - \dot{x}\right)\right] \mathrm{d}t.$$

The Hamiltonian is defined as:

$$H(x,u,\lambda,t) = L(x,u,t) - \lambda f(x,u,t).$$

So, in terms of the Hamiltonian, the augmented cost function is then given by:

$$J_a = \int_0^{t_f} \left[H(x,u,\lambda,t) + \lambda\dot{x}\right] \mathrm{d}t.$$

To determine the variation of J_a, δJ_a, the variations δx, δu, $\delta\lambda$ and $\delta\dot{x}$ are introduced. Thus, the cost variation is given by:

$$\delta J_a = \int_0^{t_f} \left[\frac{\partial H}{\partial x}\delta x + \frac{\partial H}{\partial u}\delta u + \frac{\partial H}{\partial \lambda}\delta\lambda + \dot{x}\delta\lambda + \lambda\delta\dot{x}\right] \mathrm{d}t.$$

The variation $\delta\dot{x}$ can be removed by using the integration by parts and taking into account that the initial and terminal states are fixed, we can write:

$$\begin{aligned}\int_0^{t_f} \lambda\delta\dot{x}\mathrm{d}t &= \left[\lambda(t_f)\delta x(t_f) - \lambda(0)\delta x(0)\right] - \int_0^{t_f} \dot{\lambda}\delta x\mathrm{d}t \\ &= -\int_0^{t_f} \dot{\lambda}\delta x\mathrm{d}t.\end{aligned}$$

As a result, by grouping the coefficients of each variation term, the variation of the augmented cost becomes:

$$\delta J_a = \int_0^{t_f} \left[\left(\frac{\partial H}{\partial x} - \dot{\lambda}\right)\delta x + \frac{\partial H}{\partial u}\delta u + \left(\frac{\partial H}{\partial \lambda} + \dot{x}\right)\delta\lambda\right] \mathrm{d}t.$$

By definition, this cost variation must be positive at the optimal control trajectory, u^*, for any combination of the independent variations δx, δu and $\delta\lambda$ around the optimal trajectories. In other words, the cost function accepts its minimum at the optimum and, therefore, any variation around this optimum must be accompanied by an increase in the cost. This implies that the coefficients of each independent variation must vanish at the

[1] Formally the constraint of the initial state and that of the final state should be included in the augmented cost function J_a with associated Lagrange multipliers. These additional terms are dropped out here for the sake of simplicity.

optimum. This gives the following three necessary conditions of optimality of the solution $\left(x^*, u^*, \lambda^*\right)$:

$$\begin{aligned}
\dot{x}^* &= -\frac{\partial H}{\partial \lambda}\left(x^*, u^*, \lambda^*, t\right) = f\left(x^*, u^*, t\right), \\
\dot{\lambda}^* &= \frac{\partial H}{\partial x}\left(x^*, u^*, \lambda^*, t\right), \\
\frac{\partial H}{\partial u}&\left(x^*, u^*, \lambda^*, t\right) = 0.
\end{aligned}$$

The first necessary condition is nothing else than the system dynamics. The second condition determines the optimal trajectory of the Lagrange multiplier, which is called co-state in the frame of PMP. The third condition states that the optimal control minimizes the Hamiltonian. If the control space is not constrained, then the derivative of the Hamiltonian must vanish at the optimum. However, to account for the cases where the optimal control may lie at the boundary of its constraints, where the derivative does not need to vanish, the following general condition is used instated:

$$H\left(x^*, u^*, \lambda^*, t\right) \leq H\left(x^*, u, \lambda^*, t\right), \ \forall u \in \mathbf{U}(t),$$

where $\mathbf{U}(t)$ defines the admissible control space at time t.

Appendix B

Multi-objective Optimization Using NSGA-II

In this appendix, the multi-objective optimization algorithm NSGA-II (Non-dominated Sorting Genetic Algorithm) is explained. A genetic algorithm occupies a main part of NSGA-II; therefore, it is discussed first in Section B.1. Then NSGA-II will be discussed in Section B.2.

B.1 Genetic Algorithm

A genetic algorithm (GA) [90, 91, 92] is a method for solving optimization problems based on a natural selection process that mimics the biological evolution. The algorithm repeatedly modifies a population of individual solutions. At each step, the genetic algorithm randomly selects individuals from the current population and uses them as parents to produce children for the next generation. Over successive generations, the population "evolves" toward an optimal solution. The genetic algorithm can be used to solve problems that are not well suited for standard gradient-based optimization algorithms, including problems in which the objective function is discontinuous, nondifferentiable or highly nonlinear.

As an example of an optimization problem, the function f is defined as follows:

$$f(x_1, x_2) = (x_1 - 1)^2 + (x_2 + 1)^2, \tag{B.1}$$

where f is a function of two variables, x_1 and x_2, and we want to minimize f and find the optimal solution of variables (i.e., the values of x_1 and x_2 that minimize f). In this example, the solution is trivial, which is x_1=1, x_2=-1 and the minimum f is zero.

The *fitness function* is the function that needs to be minimized. For standard optimization algorithms, this is known as the objective function. For example, the function f is a fitness function.

An *individual* is any point to which we can apply the fitness function. The value of the fitness function for an individual is its score. For example, the vector (0,0) is an

individual, whose score is $f(0,0)=2$. An individual is sometimes referred to as a *genome* and the entries of an individual as *genes*.

A *population* is an array of individuals. The algorithm uses the population in each iteration to produce the population of the next iteration, with the population in each iteration called a *generation*.

Figure B.1 illustrates the main steps of the genetic algorithm. The algorithm works as follows:

(1) The algorithm begins by creating a random initial population, which constitutes the first generation;

(2) In the evaluation step, all the individuals in the current population are scored by computing their fitness value;

(3) In the reproduction step, the algorithm generates the population of the next generation based on the scores of the individuals of the current population;

(4) The algorithm stops when one of the stopping conditions is met. The algorithm may be terminated, for example, after a specific number of generations, after a specific time or when the relative change in the fitness function is below a certain threshold.

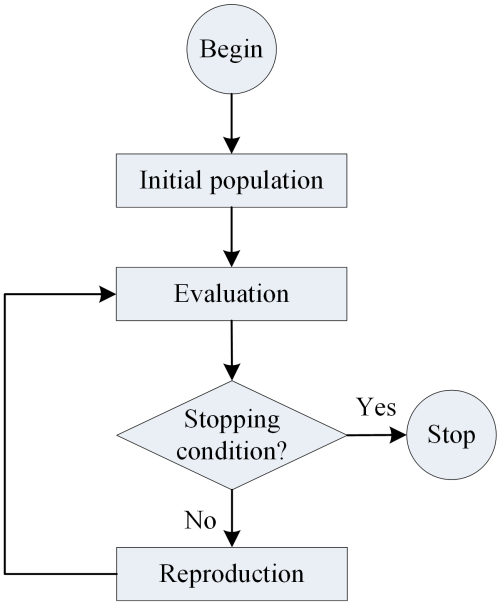

Figure B.1: Flowchart of genetic algorithm.

The reproduction step constitutes the core of the genetic algorithm, because it determines how the population evolves toward the optimal solution from one generation to another. The algorithm selects, first, a group of individuals in the current population, called *parents*, which contribute their *genes* to their children. The algorithm usually selects individuals that have better fitness values as parents. Those parents are used to create the children that make up the next generation. The genetic algorithm creates three types of children for the next generation:

- *Elite* children are the individuals in the current generation with the best fitness values. These individuals automatically survive to the next generation.
- *Crossover* children are created by combining pairs of parents. Crossover enables the algorithm to extract the best genes from different individuals and recombine them into potentially superior children.
- *Mutation* children are created by introducing random changes, or mutations, to a single parent. Mutation adds to the diversity of a population and thereby increases the likelihood that the algorithm will generate individuals with better fitness values.

The algorithm has many parameters that can be varied depending on the optimization problem under study. Among others, the stopping conditions, the population size, the elite count (the number of elite children) and the crossover fraction (the fraction of children created by crossover) are examples of the algorithm parameters.

Figure B.2 shows the results of a GA run in Matlab, for the fitness function given in equation (B.1). The figure shows the best fitness value (i.e., minimum) at each generation and the corresponding individual (i.e., x_1 and x_2). Here the default algorithm settings are used. They are, population size: 20; algorithm terminated after 100 generations; elite count: 2; crossover fraction: 0.8; parent selection: stochastic uniform; crossover function: scattered. The individuals of the initial population are chosen here to be (10,-10). At the end of the GA run, the obtained solution is (1.000,-0.998) corresponding to a fitness value of 3.4×10^{-6}. With increasing the number of generations, the GA solution becomes closer to the optimum of (1,-1).

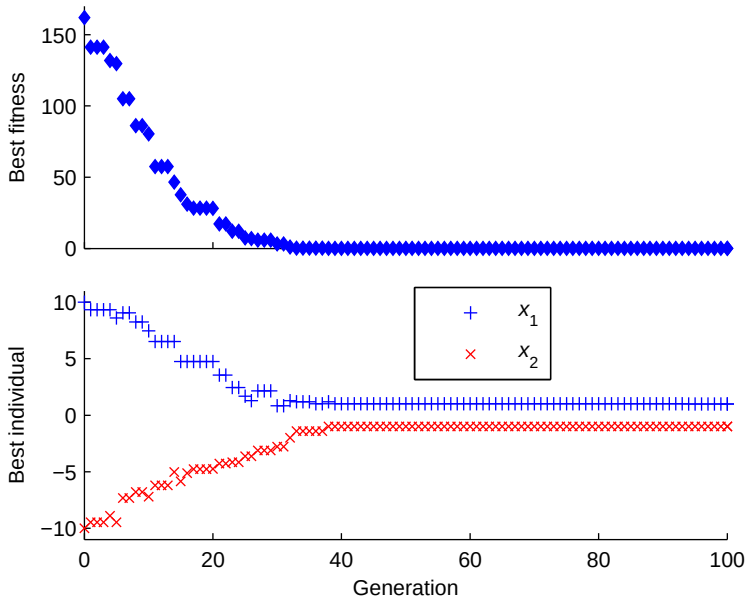

Figure B.2: Example of a GA evolution toward the optimum from generation to generation.

B.2 Multi-objective Optimization

In case of a single objective, one attempts to obtain the best solution, which is absolutely superior to all other alternatives. In the case of multiple objectives, there does not necessarily exist a solution that is best with respect to all objectives. A solution may be best in one objective but worst in other objectives. Therefore, there usually exists a set of solutions for the multi-objective case which cannot simply be compared with each other. For such solutions, called nondominated solutions or Pareto optimal solutions, no improvement in any objective function is possible without sacrificing at least one of the other objective functions.

The multi-objective optimization algorithms use the concept of domination, so that two solutions are compared based on whether one dominates the other or not. A solution X_1 is said to dominate the other solution X_2, if both conditions are true [76]:

- The solution X_1 is no worse than X_2 in all the objectives;
- The solution X_1 is strictly better than X_2 in at least one objective.

If any of the above conditions is violated, the solution X_1 does not dominate the solution X_2. The solution is called nondominated, and hence belongs to the optimal Pareto front, if and only if there does not exist another solution that dominates it.

Figure B.3 illustrates the concept of domination. Here the minimization of the two objectives f_1 and f_2 is considered. The feasible objective space, which represents all the possible values of f_1 and f_2, and the optimal Pareto front are shown. The point p_1 from the Pareto front and three possible solutions, x_1, x_2 and x_3 off the Pareto front are chosen. According to the two conditions above, we can say that x_1 does not dominate p_1 because it is worse than p_1 in the two objectives. x_2 does not as well dominate p_1, even though x_2 has a better f_1, however, with a worse f_2. The same applies to x_3, which also does not dominate p_1. p_1 belongs to the Pareto front because there is no other solution that dominates it. x_2 does not belong to the Pareto front because there are other solutions that dominate x_2 (for example p_2 from the Pareto front). Likewise, x_3 is not nondominated because there is, for example, p_3 that dominates it. The solutions p_1, p_2 and p_3 from the Pareto front do not dominate each other, and they are all nondominated. As shown in the figure, the Pareto front determines the optimal trade-off between the two objectives.

In the case of a single objective, the genetic algorithm ranks the individuals based on their corresponding fitness value. In comparison, for the multiple objectives, the individuals are ranked according to their dominance relation, while taking the diversity of the solutions into account. The most common algorithm for multi-objective optimization is NSGA-II (Non-dominated Sorting Genetic Algorithm II) [76], which is also used in Matlab [92]. A schematic of the algorithm is shown in Figure B.4.

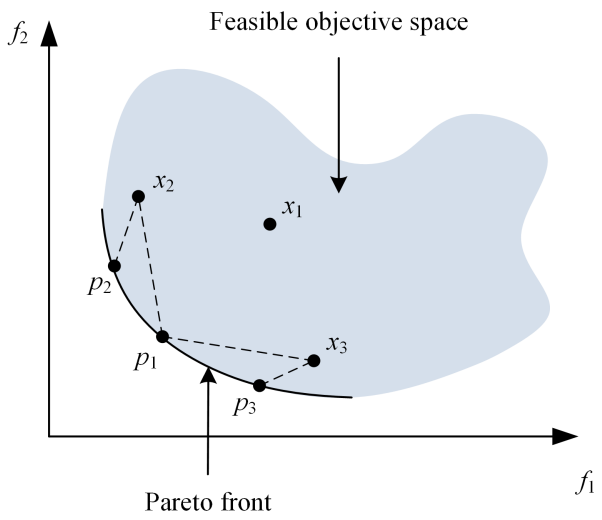

Figure B.3: Example of a Pareto front for two-objective minimization problems.

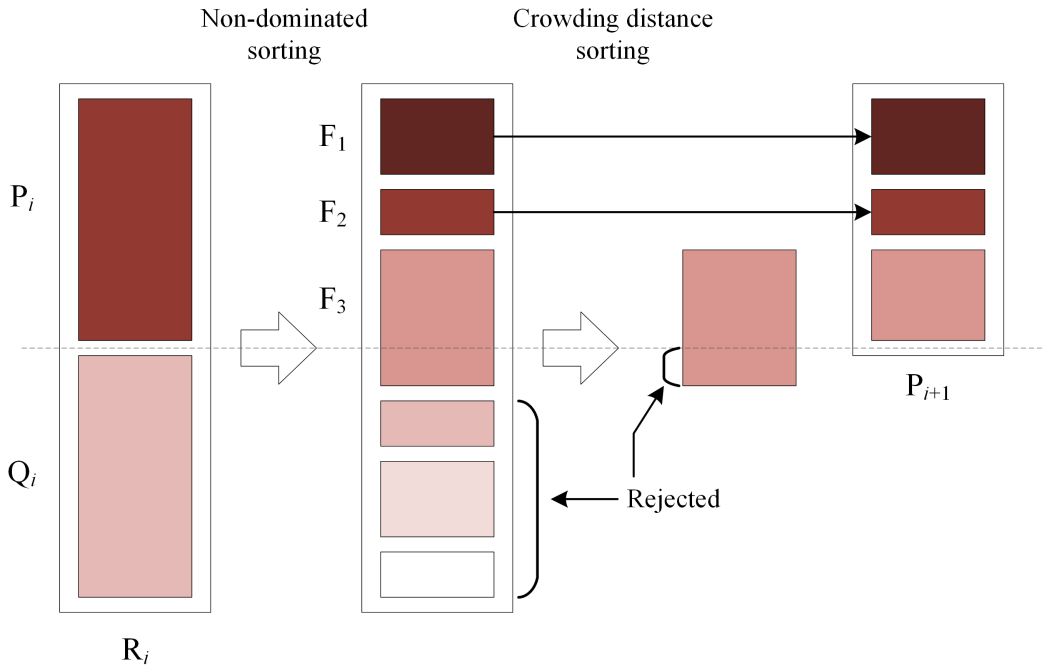

Figure B.4: Schematic of NSGA-II algorithm. Redrawn from [76].

At generation i, the population P_i of size N is sorted into different non-domination levels, so that each solution attains a rank according to its non-domination level. The offspring population Q_i of size N is generated from P_i using binary tournament selection (to select parents of Q_i) and genetic operators (crossover and mutation). The two populations P_i and Q_i are then combined to form R_i of size 2N. The binary tournament selection operator selects a parent from two individuals based on their rank for a single objective optimization. In case of multiple objectives, the crowding distance of the individual is taken into account if the two individuals have the same rank (i.e., they belong to the same front), so that the individual that has less density of individuals surrounding it gets selected (i.e., wins the tournament). This way, the diversity of solutions is improved.

The resulting population R_i undergoes a non-dominated sorting, where the solutions of the best front F_1 are first selected, then the second front F_2 and so on. The population P_{i+1} at generation $i+1$ is then filled gradually with the best fronts. In Figure B.4, for example, the solutions of F_1 are bypassed to P_{i+1}, then F_2. The size of P_{i+1} is also N, so in this example, not all the solutions of F_3 can be accommodated in P_{i+1}. In this case, the solutions of F_3 are sorted according to the crowding distance, then the solutions with the best crowding distance (i.e., ensure more diversity) are bypassed to P_{i+1}. All the other solutions (the rest of F_3, which has worse crowding distance, and the other fronts with the lowest rank) are deleted. The algorithm continues from generation to another until the stopping criterion is fulfilled. In the optimal case, after sufficient generations, P_{i+1} will be filled by only one front F_1 (representing the Pareto-optimal front) so that all the solutions of P_{i+1} will have the same rank and the number of solutions in the resulting front is N.

As an example of multi-objective optimization problem, let us consider the minimization of the two objective functions, f_1 and f_2, give by:

$$
\begin{aligned}
f_1(x) &= (x-1)^2, \\
f_2(x) &= (x+1)^2, \\
x &\in [-2, 2],
\end{aligned}
$$

where x is the single decision variable of the problem. In this simple example, the objective space is a line as shown in Figure B.5. The analytical optimal Pareto front is also shown together with the results of a multi-objective GA in Matlab. Here the default algorithm settings are used. They are, population size: 20; algorithm terminated after 100 generations; elite count: 2; crossover fraction: 0.8; parent selection: tournament; crossover function: intermediate.

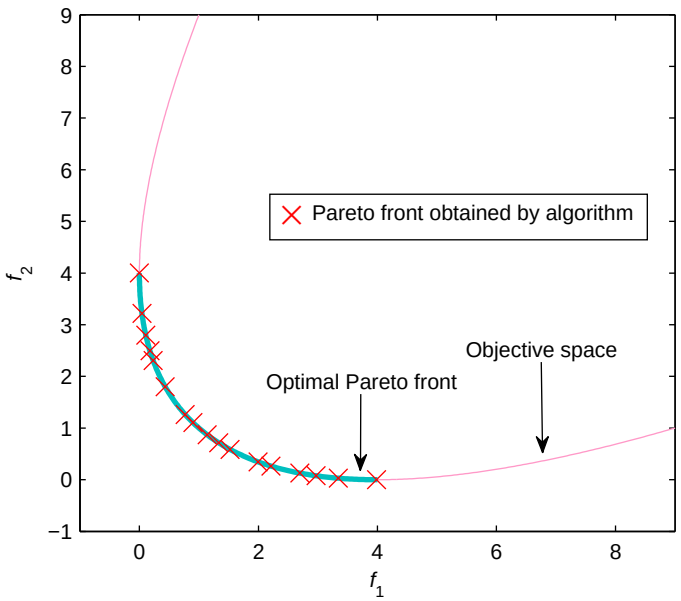

Figure B.5: Example of a multi-objective optimization.

Appendix C

Test Bench

In this appendix the layout, specifications and control of the test bench used in the experimental validations are introduced. Section C.1 reports the layout and specifications. Sections C.2, C.3 and C.4 present the models of FCS, battery and supercapacitor, respectively. The control of the DC/DC converters is discussed in Section C.5. Section C.6 presents the developed graphical user interface that enables the user to control, run and monitor the whole test bench in real time.

C.1 Specifications and Layout

The experimental test bench (Figure C.1) is composed of an FCS, a lithium-polymer battery, a supercapacitor, a unidirectional DC/DC converter for the FCS, and a bidirectional one for the supercapacitor. The two-quadrant load is composed of a source and a sink. The sink draws power from the hybrid system simulating the traction phases of the vehicle, whereas the source provides the system with power simulating the regenerative braking phases. Table C.1 lists the specifications of the test bench components. The ratings of the DC/DC converter in Table C.1 correspond to the unidirectional FCS converter. Four units of this converter are used for the supercapacitor.

The layout of the test bench is depicted in Figure C.2. The power part includes the power sources and DC/DC converters, in addition to voltage and Hall-effect current sensors at the output of each component. The digital part of the test bench is composed of a target computer and a host computer. The target computer represents the real-time control unit of the system. It takes the signals of the sensors as inputs, applies the power management strategy and, then, generates the appropriate control signals as outputs. The target computer is equipped with external high-resolution cards from Speedgoat (IO106 for the input and IO111 for the output). The host computer communicates with the target computer via Ethernet. The target application is, first, built as a Simulink model on the host computer and a compiled version (C code) of it is downloaded to the target computer. The host computer accepts the measurement data from the target computer while the test is running and after it is finished. The target application (Figure C.3) consists of the power management strategy in addition to two conditioning steps for the inputs (i.e., sensors signals) and for the outputs (i.e., control signals).

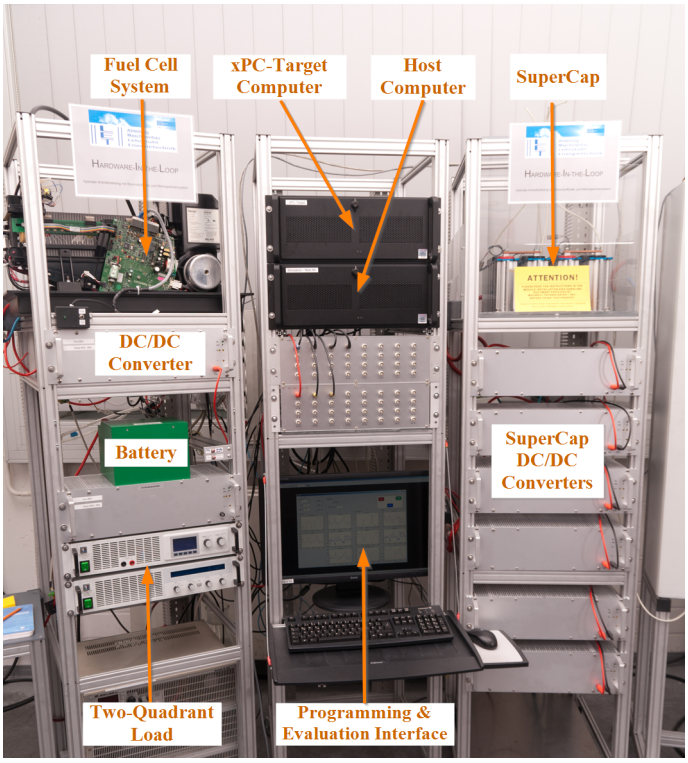

Figure C.1: Photograph of the Hardware-in-the-Loop test bench.

Table C.1: Specifications of the test bench.

Parameter	Value
Fuel cell system	
PEM stack	47 cells
Rated power	1.2 kW
Output voltage	22–43 V (26 V rated)
Battery	
No. cells	10
Capacity	30 Ah
Rated voltage	37 V
Current (max./ min./ rated)	(110/ -45/ 30) A
Supercapacitor	
No. modules	3 (each with 6 cells)
Module capacitance	500 F
Rated voltage	48 V
Current (max./ min./ rated)	(1900/ -1900/ 100) A
DC/DC converter	
Input voltage	25–47 V (36 V rated)
Output voltage	25–50 V (50 V rated)
Maximum output current	25 A
Load	
Sink ratings	80 V/ 200 A/ 2400 W
Source ratings	80 V/ 50 A/ 1500 W

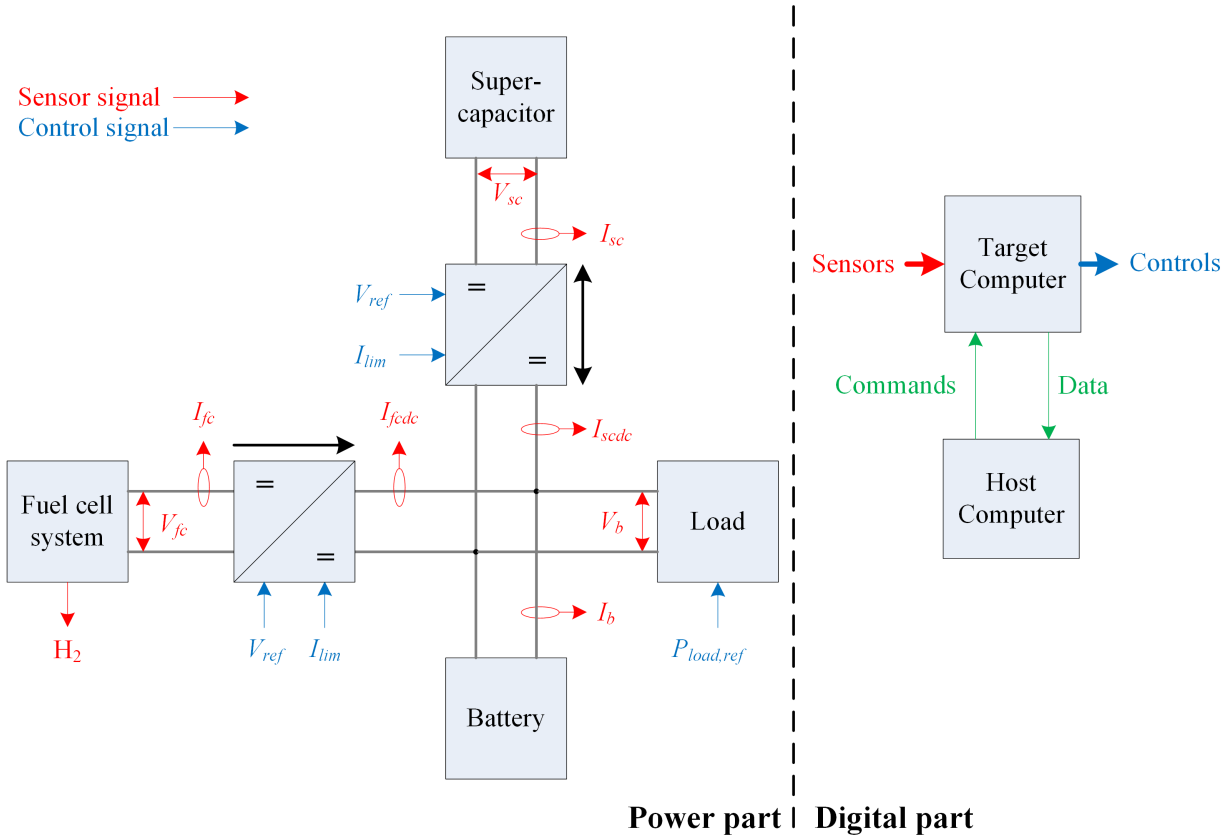

Figure C.2: Schematic of the test bench layout.

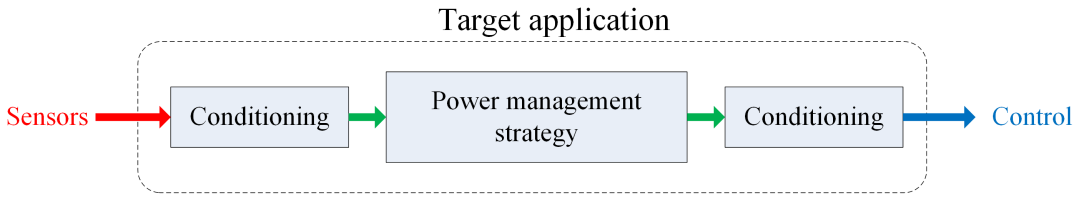

Figure C.3: Basic structure of the target application.

C.2 Fuel Cell System

A 1.2 kW, 26 V FCS from Ballard is used in the test bench. The FCS and its unidirectional DC/DC converter are modeled by their steady state efficiencies shown in Figure C.4(b), which shows the overall efficiency of the two components, as well. The overall efficiency of the FCS and its DC/DC converter is defined as the ratio of the converter output power, P_{fcdc}, to the hydrogen power, where the hydrogen power is the product of hydrogen mass flow rate and hydrogen lower heating value, LHV (=120 kJ/g). The hydrogen flow rate is modeled by a second-order polynomial function of P_{fcdc} (Figure C.4(a)) fitted to experimental data. A comparison between the measured overall efficiency and the model efficiency is illustrated in Figure C.4(b). Due to aging, the FCS had lost its high power capability and, therefore, P_{fcdc} was limited to 700 W. The voltage and power characteristics of the FCS are shown in Figure C.5.

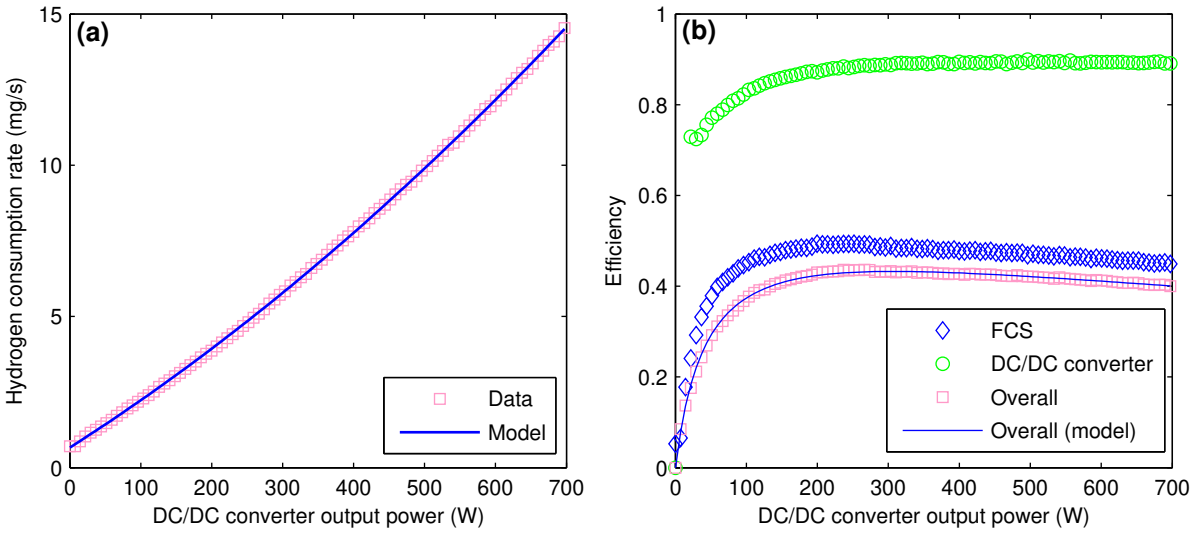

Figure C.4: Modeling of the FCS and its DC/DC converter. (a) Hydrogen consumption rate; (b) Efficiency of FCS and its DC/DC converter.

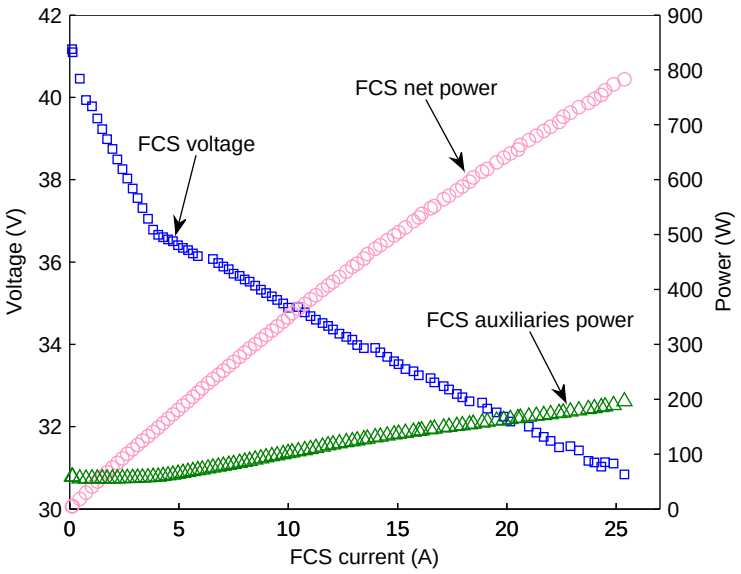

Figure C.5: Voltage and power characteristics of the FCS.

C.3 Battery

A 30 Ah lithium-polymer battery from Hoppecke is used. It is composed of 10 cells connected in series. The parameters of the internal-resistance model of the battery shown in Figure C.6 were identified by an HPPC test (Hybrid Pulse Power Characterization) [69].

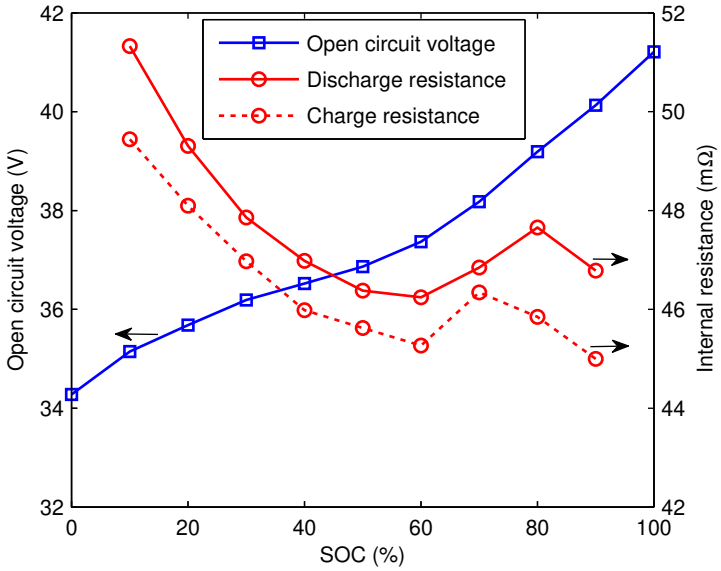

Figure C.6: Parameters of the battery internal-resistance model as a function of SOC.

C.4 Supercapacitor

The supercapacitor bank is composed of three BMOD0500P016B02 6-cell modules from Maxwell Technologies. Each module has a rated capacitance of 500 F, an internal resistance of 2.1 mΩ and a rated voltage of 16 V [93]. These characteristics have been experimentally verified in Table C.2 using the profiles given in the product datasheet.

Table C.2: Measurements of capacitance and internal resistance of the three modules constituting the supercapacitor bank.

	Capacitance (F)	**Resistance (mΩ)**
Module 1	498	2.02
Module 2	499	2.06
Module 3	497	1.99

The bidirectional DC/DC converter of the supercapacitor is formed by four unidirectional converters of the type given in Table C.1; two serve to discharge the supercapacitor and the other two to charge it. Figure C.7 shows the relation between the power at the supercapacitor side, P_{sc}, and that at the electric bus side, P_{scdc}, for a voltage of 37 V at both sides. The difference between them constitutes the power loss in the DC/DC converters.

C.5 DC/DC Converters

The DC/DC converters are responsible for the realization of the power management strategy. They are of buck-boost type, so that the output voltage can be smaller or higher than the input voltage. They are equipped with two control inputs: one to set

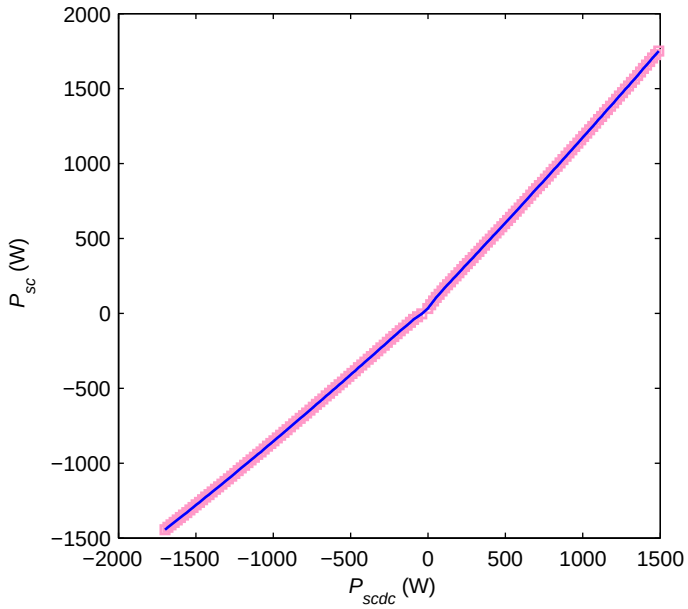

Figure C.7: Input-output power relation of the supercapacitor bidirectional DC/DC converter.

the reference output voltage, and one to limit the output current. The reference output voltage can be varied between 25 and 50 V, and the output current can be limited to any value between 0 and 25 A. Depending on the powertrain topology, the converters are operated either in the voltage-controlled mode (i.e., output voltage is controlled) or in a current-limited mode (output current is controlled).

For a fuel cell/battery topology shown in Figure 2.6, the converter in front of the FCS controls the FCS contribution in meeting the demand at each time instance. The output voltage is the DC bus voltage that is set by the battery, with about 37 V as a nominal value. In order to set the FCS converter output power to P_{fcdc}, the bus voltage, V_{bus}, is measured and the required output current, $I_{fcdc} = P_{fcdc}/V_{bus}$, is then calculated. The reference voltage of the converter is set always to the maximum value of 50 V. Since the actual output voltage is smaller than the reference, the converter operates in the current-limited mode, so that the output current will be the maximum possible value permitted by the current limitation. So, I_{fcdc} is implemented by the converter if I_{fcdc} is used as a current limitation. The battery contribution is then determined by the power balance.

For a fuel cell/supercapacitor topology shown in Figure 3.1, the FCS converter is operated in the voltage-controlled mode where 37 V is used as a reference voltage (which is also the DC bus voltage) and the current limitation is set to its maximum value. On the other hand, the supercapacitor converters are operated in the current-limited mode so that the power contribution of the supercapacitor is controlled by the power management strategy, and the FCS contribution is determined by the power balance.

For a fuel cell/battery/supercapacitor topology shown in Figure 4.1, both the FCS converter and supercapacitor converter are operated in the current-limited mode so that their power contributions are controlled by the power management strategy. The battery contribution is then determined by the power balance.

C.6 Graphical User Interface (GUI)

The host computer is equipped with a friendly GUI to help the user to control the test and to process the measurement data. The GUI displays the measurements online (i.e., while running the test) with a sample time of 100 ms. However, after finishing the test, the measured data are collected from the target machine with a sample time of 10 ms, which is the sample time used in the target application. Figure C.8 shows, as example, the GUI of the fuel cell/battery hybrid. Similar GUIs are used for the fuel cell/supercapacitor and fuel cell/battery/supercapacitor topologies. The GUI is divided into the following panels:

- Test Control: This panel serves to configure the test. This includes selecting driving cycle (most standard driving cycles are preprogrammed), scaling and cropping of the selected driving cycle, initializing the test (processing the chosen driving cycle and then compiling and downloading the target application to the target machine), starting and stopping the test (the test can be interrupted at any time; otherwise, it stops after finishing the test).
- Data control: At the end of the test the complete data collected by the target machine can be transferred to the host machine to be processed and saved. The loaded measurements can be filtered by a median filter to remove the noise.
- Driving Cycle: This panel shows the speed and power profile of the chosen driving cycle. The vehicle model is used to calculate the vehicle power demand, which is then, after scaling, used as a reference for the test bench load.
- Load: This panel shows the measured current, voltage and power of the load.
- Fuel Cell System: This panel shows the current, voltage and accumulated hydrogen consumption of the fuel cell system. The last value of the accumulated hydrogen consumption represents the fuel consumption over the driving cycle.
- Battery: This panel shows the battery current, voltage and SOC trajectory.
- System status: This panel shows online the direction of system currents, and hence the system operation mode. Eight system operation modes can be distinguished as shown in the following table.

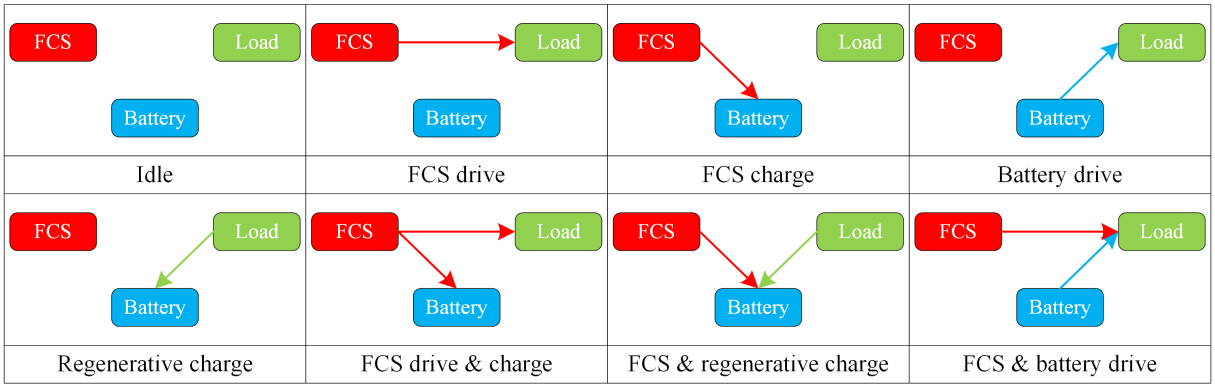

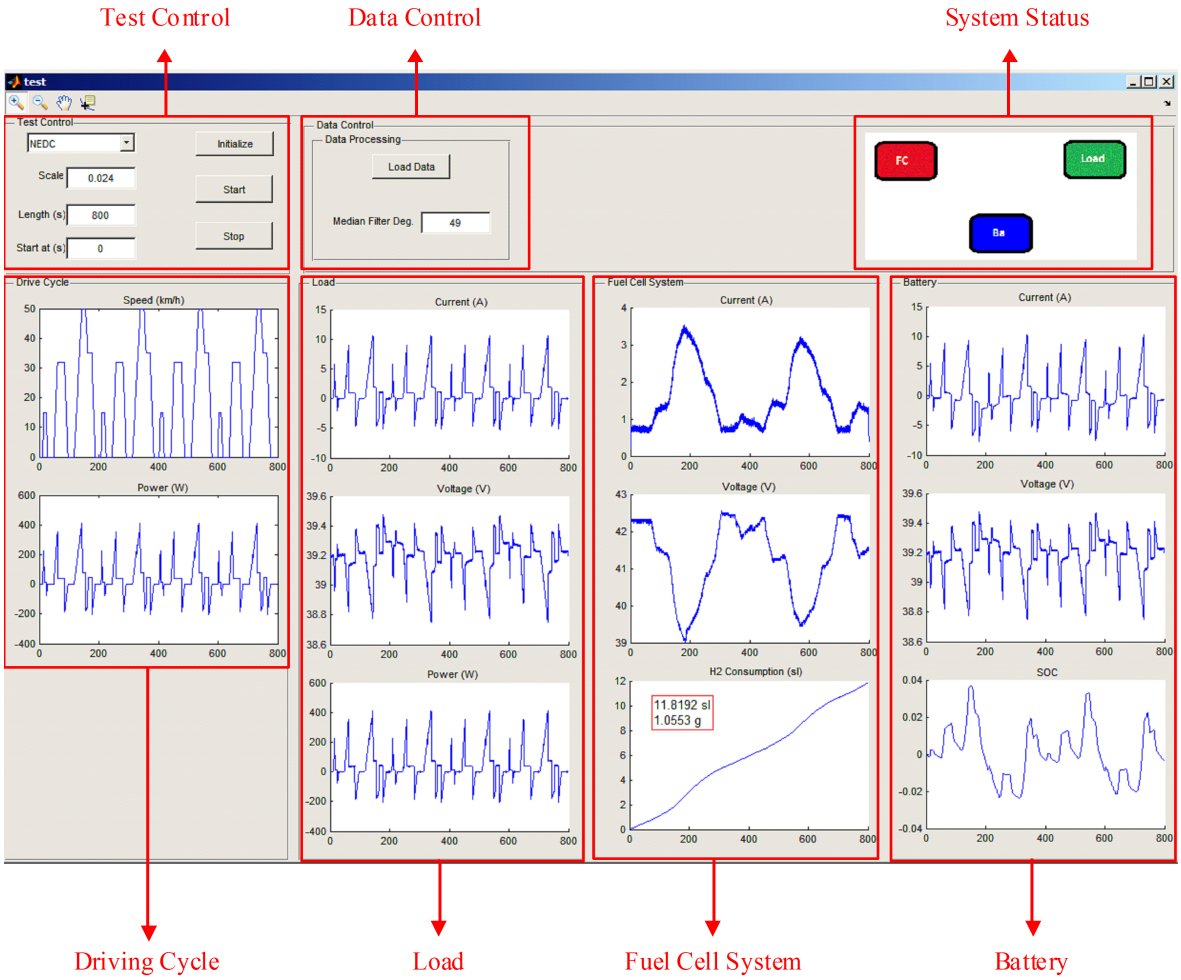

Figure C.8: Graphical user interface of the fuel cell/battery topology.

Bibliography

[1] Statista Inc., "Worldwide production of passenger cars 1998-2014 | Statistic." Available online: http://www.statista.com/statistics/268739/production-of-passenger-cars-worldwide/. (accessed on Sept. 22, 2015).

[2] EUR-Lex, "EUR-Lex - 02009R0443-20140408 - EN - EUR-Lex." Regulation (EC) No 443/2009 of the European Parliament and of the Council of 23 April 2009 amended by Commission Regulation (EU) No 397/2013 of 30 April 2013 and Regulation (EU) No 333/2014 of the European Parliament and of the Council of 11 March 2014. Available online: http://eur-lex.europa.eu/legal-content/EN/TXT/?uri=CELEX:02009R0443-20140408. (accessed on Sept. 22, 2015).

[3] European Environment Agency (EEA), "Average carbon dioxide emissions from new passenger cars-European Environment Agency (EEA)." Available online: http://www.eea.europa.eu/data-and-maps/daviz/average-emissions-for-new-cars. (accessed on Sept. 22, 2015).

[4] U.S. Energy Information Administration (EIA), "Annual Energy Review - Energy Information Administration." Available online: http://www.eia.gov/totalenergy/data/annual/index.cfm. (accessed on Sept. 22, 2015).

[5] B. C. Chan, "The state of the art of electric, hybrid, and fuel cell vehicles," *Proceedings of the IEEE*, vol. 95, no. 4, pp. 704–718, 2007.

[6] J. Erjavec, *Hybrid, electric & fuel cell vehicles*. Delmar, US: Cengage Learning, Inc., 2 ed., 2013.

[7] T. Pels and C. Kaup, "Micro, mild, and full hybrids," *Encyclopedia of Automotive Engineering*.

[8] J. Laramine and A. Dicks, *Fuel cell systems explained*. Chichster, England: John Wiley & Sons Ltd, 2 ed., 2003.

[9] A. Veziroglu and R. Macario, "Fuel cell vehicles: State of the art with economic and environmental concerns," *International Journal of Hydrogen Energy*, vol. 36, no. 1, pp. 25–43, 2011.

[10] Office of Energy Efficiency and Renewable Energy (EERE)-U.S. Department of Energy (DOE), "Fuel Cell Technologies Office Multi-Year Research, Development and Demonstration Plan–3.4 Fuel Cells." Available online: http://energy.gov/sites/prod/files/2014/12/f19/fcto_myrdd_fuel_cells.pdf. (accessed on Sept. 22, 2015).

[11] P. Pei, Q. Chang, and T. Tang, "A quick evaluating method for automotive fuel cell lifetime," *International Journal of Hydrogen Energy*, vol. 33, no. 14, pp. 3829–3836, 2008.

[12] P. Pei and H. Chen, "Main factors affecting the lifetime of proton exchange membrane fuel cells in vehicle applications: A review," *Applied Energy*, vol. 125, pp. 60–75, 2014.

[13] M. Broussely, "Battery requirements for HEVs, PHEVs, and EVs: An overview," *Electric and Hybrid Vehicles: Power Sources, Models, Sustainability, Infrastructure and the Market*, pp. 305–347, 2010.

[14] M. Broussely, P. Biensan, F. Bonhomme, P. Blanchard, S. Herreyre, K. Nechev, and R. Staniewicz, "Main aging mechanisms in Li ion batteries," *Journal of Power Sources*, vol. 146, no. 1, pp. 90–96, 2005.

[15] M. Ecker, N. Nieto, S. Käbitz, J. Schmalstieg, H. Blanke, A. Warnecke, and D. U. Sauer, "Calendar and cycle life study of Li(NiMnCo)O2-based 18650 lithium-ion batteries," *Journal of Power Sources*, vol. 248, pp. 839–851, 2014.

[16] A. F. Burke, "Batteries and ultracapacitors for electric, hybrid, and fuel cell vehicles," *Proceedings of the IEEE*, vol. 95, no. 4, pp. 806–820, 2007.

[17] Honda Motor Co., Ltd., "Honda Worldwide | Fuel Cell | FCX." Available online: `http://world.honda.com/FuelCell/FCX/`. (accessed on Sept. 22, 2015).

[18] F. R. Salmasi, "Control strategies for hybrid electric vehicles: Evolution, classification, comparison, and future trends," *Vehicular Technology, IEEE Transactions on*, vol. 56, no. 5, pp. 2393–2404, 2007.

[19] A. Sciarretta and L. Guzzella, "Control of hybrid electric vehicles," *Control systems, IEEE*, vol. 27, no. 2, pp. 60–70, 2007.

[20] G. Rizzoni and S. Onori, "Energy management of hybrid electric vehicles: 15 years of development at the Ohio State University," *Oil & Gas Science and Technology–Revue d'IFP Energies nouvelles*, vol. 70, no. 1, pp. 41–54, 2015.

[21] L. Serrao, S. Onori, and G. Rizzoni, "A comparative analysis of energy management strategies for hybrid electric vehicles," *Journal of Dynamic Systems, Measurement, and Control*, vol. 133, no. 3, p. 031012, 2011.

[22] D. P. Bertsekas, *Dynamic Programming and Optimal Control*, vol. 1. Belmont, Massachusetts: Athena Scientific, 3 ed., 2005.

[23] C.-C. Lin, H. Peng, J. W. Grizzle, and J.-M. Kang, "Power management strategy for a parallel hybrid electric truck," *Control Systems Technology, IEEE Transactions on*, vol. 11, no. 6, pp. 839–849, 2003.

[24] O. Sundström and L. Guzzella, "A generic dynamic programming Matlab function," in *Control Applications,(CCA) & Intelligent Control,(ISIC), 2009 IEEE*, pp. 1625–1630, IEEE, 2009.

[25] D. E. Kirk, *Optimal Control Theory: An Introduction*. New York: Dover Publications Inc., 14 ed., 2004.

[26] G. Rousseau, D. Sinoquet, and P. Rouchon, "Constrained optimization of energy

management for a mild-hybrid vehicle," *Oil & Gas Science and Technology-Revue de l'IFP*, vol. 62, no. 4, pp. 623–634, 2007.

[27] N. Kim, S. Cha, and H. Peng, "Optimal control of hybrid electric vehicles based on Pontryagin's minimum principle," *Control Systems Technology, IEEE Transactions on*, vol. 19, no. 5, pp. 1279–1287, 2011.

[28] X. Hu, N. Murgovski, L. M. Johannesson, and B. Egardt, "Optimal dimensioning and power management of a fuel cell/battery hybrid bus via convex programming," *Mechatronics, IEEE/ASME Transactions on*, vol. 20, no. 1, pp. 457–468, 2015.

[29] X. Hu, L. Johannesson, N. Murgovski, and B. Egardt, "Longevity-conscious dimensioning and power management of the hybrid energy storage system in a fuel cell hybrid electric bus," *Applied Energy*, vol. 137, pp. 913–924, 2015.

[30] E. D. Tate and S. P. Boyd, "Finding ultimate limits of performance for hybrid electric vehicles," Tech. Rep. No. 2000-01-3099, SAE Technical Paper, 2000.

[31] J. Liu and H. Peng, "Modeling and control of a power-split hybrid vehicle," *Control Systems Technology, IEEE Transactions on*, vol. 16, no. 6, pp. 1242–1251, 2008.

[32] T. Leroy, J. Malaize, and G. Corde, "Towards real-time optimal energy management of HEV powertrains using stochastic dynamic programming," in *Vehicle Power and Propulsion Conference (VPPC), 2012 IEEE*, pp. 383–388, IEEE, 2012.

[33] G. Paganelli, T. Guerra, S. Delprat, J. Santin, M. Delhom, and E. Combes, "Simulation and assessment of power control strategies for a parallel hybrid car," *Proceedings of the Institution of Mechanical Engineers, Part D: Journal of Automobile Engineering*, vol. 214, no. 7, pp. 705–717, 2000.

[34] A. Sciarretta, M. Back, and L. Guzzella, "Optimal control of parallel hybrid electric vehicles," *Control Systems Technology, IEEE Transactions on*, vol. 12, no. 3, pp. 352–363, 2004.

[35] C. Musardo, G. Rizzoni, Y. Guezennec, and B. Staccia, "A-ECMS: An adaptive algorithm for hybrid electric vehicle energy management," *European Journal of Control*, vol. 11, no. 4, pp. 509–524, 2005.

[36] B. Gu and G. Rizzoni, "An adaptive algorithm for hybrid electric vehicle energy management based on driving pattern recognition," in *ASME 2006 International Mechanical Engineering Congress and Exposition*, pp. 249–258, American Society of Mechanical Engineers, 2006.

[37] L. Serrao, S. Onori, and G. Rizzoni, "ECMS as a realization of Pontryagin's minimum principle for HEV control," in *Proceedings of the American control conference*, pp. 3964–3969, 2009.

[38] H. Borhan, A. Vahidi, A. M. Phillips, M. L. Kuang, I. V. Kolmanovsky, and S. D. Cairano, "MPC-based energy management of a power-split hybrid electric vehicle," *Control Systems Technology, IEEE Transactions on*, vol. 20, no. 3, pp. 593–603, 2012.

[39] S. Di Cairano, D. Bernardini, A. Bemporad, and I. V. Kolmanovsky, "Stochastic MPC with learning for driver-predictive vehicle control and its application to HEV

energy management," *Control Systems Technology, IEEE Transactions on*, vol. 22, no. 3, pp. 1018–1031, 2014.

[40] K. B. Wipke, M. R. Cuddy, and S. D. Burch, "ADVISOR 2.1: A user-friendly advanced powertrain simulation using a combined backward/forward approach," *Vehicular Technology, IEEE Transactions on*, vol. 48, no. 6, pp. 1751–1761, 1999.

[41] M. Cipek, D. Pavković, and J. Petrić, "A control-oriented simulation model of a power-split hybrid electric vehicle," *Applied Energy*, vol. 101, pp. 121–133, 2013.

[42] N. J. Schouten, M. A. Salman, and N. A. Kheir, "Energy management strategies for parallel hybrid vehicles using fuzzy logic," *Control Engineering Practice*, vol. 11, no. 2, pp. 171–177, 2003.

[43] M. Kisacikoglu, M. Uzunoglu, and M. Alam, "Load sharing using fuzzy logic control in a fuel cell/ultracapacitor hybrid vehicle," *International Journal of Hydrogen Energy*, vol. 34, no. 3, pp. 1497–1507, 2009.

[44] X. Li, L. Xu, J. Hua, X. Lin, J. Li, and M. Ouyang, "Power management strategy for vehicular-applied hybrid fuel cell/battery power system," *Journal of Power Sources*, vol. 191, no. 2, pp. 542–549, 2009.

[45] C.-Y. Li and G.-P. Liu, "Optimal fuzzy power control and management of fuel cell/battery hybrid vehicles," *Journal of Power Sources*, vol. 192, no. 2, pp. 525–533, 2009.

[46] S. Caux, W. Hankache, M. Fadel, and D. Hissel, "On-line fuzzy energy management for hybrid fuel cell systems," *International Journal of Hydrogen Energy*, vol. 35, no. 5, pp. 2134–2143, 2010.

[47] Z. Chen, R. Xiong, K. Wang, and B. Jiao, "Optimal energy management strategy of a plug-in hybrid electric vehicle based on a particle swarm optimization algorithm," *Energies*, vol. 8, no. 5, pp. 3661–3678, 2015.

[48] M. Ansarey, M. S. Panahi, H. Ziarati, and M. Mahjoob, "Optimal energy management in a dual-storage fuel-cell hybrid vehicle using multi-dimensional dynamic programming," *Journal of Power Sources*, vol. 250, pp. 359–371, 2014.

[49] P. Bubna, S. G. Advani, and A. K. Prasad, "Integration of batteries with ultracapacitors for a fuel cell hybrid transit bus," *Journal of Power Sources*, vol. 199, pp. 360–366, 2012.

[50] P. Thounthong, S. Rael, and B. Davat, "Energy management of fuel cell/battery/supercapacitor hybrid power source for vehicle applications," *Journal of Power Sources*, vol. 193, no. 1, pp. 376–385, 2009.

[51] D. Gao, Z. Jin, and Q. Lu, "Energy management strategy based on fuzzy logic for a fuel cell hybrid bus," *Journal of Power Sources*, vol. 185, no. 1, pp. 311–317, 2008.

[52] Q. Li, W. Chen, Y. Li, S. Liu, and J. Huang, "Energy management strategy for fuel cell/battery/ultracapacitor hybrid vehicle based on fuzzy logic," *International Journal of Electrical Power & Energy Systems*, vol. 43, no. 1, pp. 514–525, 2012.

[53] V. Paladini, T. Donateo, A. De Risi, and D. Laforgia, "Super-capacitors fuel-cell

hybrid electric vehicle optimization and control strategy development," *Energy Conversion and Management*, vol. 48, no. 11, pp. 3001–3008, 2007.

[54] R. T. Bambang, A. S. Rohman, C. J. Dronkers, R. Ortega, A. Sasongko, *et al.*, "Energy management of fuel cell/battery/supercapacitor hybrid power sources using model predictive control," *Industrial Informatics, IEEE Transactions on*, vol. 10, no. 4, pp. 1992–2002, 2014.

[55] E. Silvas, T. Hofman, N. Murgovski, P. Etman, and M. Steinbuch, "Review of optimization strategies for system-level design in hybrid electric vehicles," *Vehicular Technology, IEEE Transactions on*, DOI:10.1109/TVT.2016.2547897, 2016.

[56] R. T. Doucette and M. D. McCulloch, "A comparison of high-speed flywheels, batteries, and ultracapacitors on the bases of cost and fuel economy as the energy storage system in a fuel cell based hybrid electric vehicle," *Journal of Power Sources*, vol. 196, no. 3, pp. 1163–1170, 2011.

[57] X. Wu, B. Cao, J. Wen, and Z. Wang, "Application of particle swarm optimization for component sizes in parallel hybrid electric vehicles," in *Evolutionary Computation, 2008. CEC 2008.(IEEE World Congress on Computational Intelligence). IEEE Congress on*, pp. 2874–2878, IEEE, 2008.

[58] O. Hegazy and J. Van Mierlo, "Particle swarm optimization for optimal powertrain component sizing and design of fuel cell hybrid electric vehicle," in *Optimization of Electrical and Electronic Equipment (OPTIM), 2010 12th International Conference on*, pp. 601–609, IEEE, 2010.

[59] W. Gao and C. Mi, "Hybrid vehicle design using global optimisation algorithms," *International Journal of Electric and Hybrid Vehicles*, vol. 1, no. 1, pp. 57–70, 2007.

[60] O. Hegazy and J. Van Mierlo, "Optimal power management and powertrain components sizing of fuel cell/battery hybrid electric vehicles based on particle swarm optimisation," *International Journal of Vehicle Design*, vol. 58, no. 2-4, pp. 200–222, 2012.

[61] S. Ebbesen, P. Elbert, and L. Guzzella, "Engine downsizing and electric hybridization under consideration of cost and drivability," *Oil & Gas Science and Technology–Revue d'IFP Energies nouvelles*, vol. 68, no. 1, pp. 109–116, 2013.

[62] M.-J. Kim and H. Peng, "Power management and design optimization of fuel cell/battery hybrid vehicles," *Journal of Power Sources*, vol. 165, no. 2, pp. 819–832, 2007.

[63] J. Bernard, S. Delprat, F. N. Büchi, and T. M. Guerra, "Fuel-cell hybrid powertrain: Toward minimization of hydrogen consumption," *Vehicular Technology, IEEE Transactions on*, vol. 58, no. 7, pp. 3168–3176, 2009.

[64] T. Nuesch, T. Ott, S. Ebbesen, and L. Guzzella, "Cost and fuel-optimal selection of HEV topologies using particle swarm optimization and dynamic programming," in *American Control Conference (ACC), 2012*, pp. 1302–1307, IEEE, 2012.

[65] L. Guzzella and A. Sciarretta, *Vehicle Propulsion Systems, Introduction to Modeling and Optimization*. Berlin, Germany: Springer-Verlag, 2005.

[66] M. Zolot, T. Markel, and A. Pesaran, "Analysis of fuel cell hybridization and implications for energy storage devices," in *4 th International Advanced Automotive Battery Conference*, (San Francisco, California), June 2004.

[67] K. Wipke, S. Sprik, J. Kurtz, T. Ramsden, and J. Garbak, "DOE's national fuel cell vehicle learning demonstration project–NREL's data analysis results," *Electric and Hybrid Vehicles: Power Sources, Models, Sustainability, Infrastructure and the Market*, p. 287, 2010.

[68] V. Johnson, "Battery performance models in ADVISOR," *Journal of power sources*, vol. 110, no. 2, pp. 321–329, 2002.

[69] Idaho National Engineering and Environmental Laboratory (INEEL), *FreedomCAR Battery Test Manual for Power-Assist Hybrid Electric Vehicles*, October 2003.

[70] J. Han, Y. Park, and D. Kum, "Optimal adaptation of equivalent factor of equivalent consumption minimization strategy for fuel cell hybrid electric vehicles under active state inequality constraints," *Journal of Power Sources*, vol. 267, pp. 491–502, 2014.

[71] T. van Keulen, *Fuel Optimal Control of Hybrid Vehicles*. PhD thesis, Technische Universiteit Eindhoven, 2011.

[72] F. Odeim, J. Roes, L. Wülbeck, and A. Heinzel, "Power management optimization of fuel cell/battery hybrid vehicles with experimental validation," *Journal of Power Sources*, vol. 252, pp. 333–343, 2014.

[73] N. Kim and A. Rousseau, "Sufficient conditions of optimal control based on Pontryagin's minimum principle for use in hybrid electric vehicles," *Proceedings of the Institution of Mechanical Engineers, Part D: Journal of Automobile Engineering*, vol. 226, no. 9, pp. 1160–1170, 2012.

[74] U. S. Department of Energy, "Fuel cell system cost–2012." DOE Fuel Cell Technologies Program Record (Record No. 12020), August 2012. Available online: `www.hydrogen.energy.gov/pdfs/12020_fuel_cell_system_cost_2012.pdf`. (accessed on Sept. 22, 2015).

[75] K.-H. Hauer, *Analysis Tool for Fuel Cell Vehicle Hardware and Software (Controls) with an Application to Fuel Economy Comparisons of Alternative System Designs*. PhD thesis, University of California Davis, 2001. p. 180.

[76] K. Deb, *Multi-objective optimization using evolutionary algorithms*. Chichester, UK: John Wiley & Sons Ltd, 2001.

[77] S. B. Ebbesen, *OPTIMAL SIZING AND CONTROL OF HYBRID ELECTRIC VEHICLES*. PhD thesis, ETH Zurich, 2012. Chapter 5.

[78] V. Marano, S. Onori, Y. Guezennec, G. Rizzoni, and N. Madella, "Lithium-ion batteries life estimation for plug-in hybrid electric vehicles," in *Vehicle Power and Propulsion Conference, 2009. VPPC'09. IEEE*, pp. 536–543, IEEE, 2009.

[79] L. Serrao, S. Onori, A. Sciarretta, Y. Guezennec, and G. Rizzoni, "Optimal energy management of hybrid electric vehicles including battery aging," in *American Control Conference (ACC), 2011*, pp. 2125–2130, IEEE, 2011.

[80] J. Schmalstieg, S. Käbitz, M. Ecker, and D. U. Sauer, "A holistic aging model for Li(NiMnCo)O2 based 18650 lithium-ion batteries," *Journal of Power Sources*, vol. 257, pp. 325–334, 2014.

[81] Maxwell Technologies, "Datasheet K2 ultracapacitors–2.7V series." Available online: `www.maxwell.com`. (accessed on Sept. 22, 2015).

[82] P. Rodatz, O. Garcia, L. Guzzella, F. Büchi, M. Bärtschi, A. Tsukada, P. Dietrich, R. Kötz, G. Scherer, and A. Wokaun, "Performance and operational characteristics of a hybrid vehicle powered by fuel cells and supercapacitors," Tech. Rep. No. 2003-01-0418, SAE Technical Paper, 2003.

[83] J. Schiffer, O. Bohlen, R. W. De Doncker, D. U. Sauer, and K. Y. Ahn, "Optimized energy management for fuelcell-supercap hybrid electric vehicles," in *Vehicle Power and Propulsion, 2005 IEEE Conference*, pp. 341–348, IEEE, 2005.

[84] C. Zheng, G. Xu, Y. Park, W. Lim, and S. Cha, "Prolonging fuel cell stack lifetime based on Pontryagin's minimum principle in fuel cell hybrid vehicles and its economic influence evaluation," *Journal of Power Sources*, vol. 248, pp. 533–544, 2014.

[85] F. Odeim, J. Roes, and A. Heinzel, "Power management optimization of a fuel cell/battery/supercapacitor hybrid system for transit bus applications," *Vehicular Technology, IEEE Transactions on*, vol. 65, pp. 5783–5788, 2016.

[86] F. Odeim, J. Roes, and A. Heinzel, "Power management optimization of an experimental fuel cell/battery/supercapacitor hybrid system," *Energies*, vol. 8, no. 7, pp. 6302–6327, 2015.

[87] Mercedes-Benz, "The Citaro FuelCELL Hybrid." Available online: `www.mercedes-benz.de`. (accessed on Sept. 22, 2015).

[88] A123 Systems, "Nanophosphate lithium ion prismatic pouch cell AMP20M1HD-A." Available online: `www.a123systems.com`. (accessed on Sept. 22, 2015).

[89] H. P. Geering, *Optimal control with engineering applications*. Berlin, Germany: Springer-Verlag, 2007.

[90] M. Gen and R. Cheng, *Genetic algorithms and engineering optimization*. New York, USA: John Wiley & Sons, 2000.

[91] R. L. Haupt and S. E. Haupt, *Practical genetic algorithms*. Hoboken, New Jersey, USA: John Wiley & Sons, Inc., 2 ed., 2004.

[92] MathWorks, "Global Optimization Toolbox, User's Guide." Available online: `www.mathworks.com`. (accessed on Sept. 22, 2015).

[93] Maxwell Technologies, "BMOD0500P016B02 Datasheet." Available online: `www.maxwell.com`. (accessed on Sept. 22, 2015).